A low-cost ultrasonic 3D measurement device for calibration of Cartesian and non-Cartesian machines

by

Fouad Juma Aldawi

A thesis submitted to the University of Huddersfield
In partial fulfilmentof the requirements for
the degree of Doctor of Philosophy

The University of Huddersfield
(December, 2009)

Abstract

The major obstacles to the widespread adoption of 3D measurement systems are accuracy, speed of process and the cost. At present, high accuracy for measuring 3D position has been achieved, and there have been real advances in reducing measurement time, but the cost of such systems remains high.

A high-accuracy and high-resolution ultrasonic distance measurement system has been achieved in this project by creating multi-frequency continuous wave frequency modulation (MFCWFM) system. The low-cost system measures dynamic distance (displacements of an ultrasound transmitter) and fixed distance (distances between receivers). The instantaneous distance between the transmitter and each receiver can be precisely determined.

New geometric algorithms for transmitter 3D position and receiver positing have also been developed in the current research to improve the measurement system's practicability. These algorithms allow the ultrasound receivers to be arbitrarily placed and located by self-calibration following a simple procedure.

After the development and testing of the new 3D measurement system, further studies have also been carried out on the system, considering the two major external disturbances: air temperature drifting and ultrasound echo interference. Novel methods have been successfully developed and tested to minimize measurement errors and evaluation of speed of sound.

All the enabling research described in the thesis means that it is now possible to build and implement a measurement system at reasonable cost for industrial exploitation. This will have the necessary performance to provide ultrasonic 3D position measurements in real time for monitoring position.

Acknowledgements

During the three years of research on this project. I have received help and supports from several people, to whom I would like to express my sincere gratitude.

First and foremost, I would like to thank my supervisor, Dr. Andrew P Longstaff for not only giving me this greatest opportunity, but also his continued interest, guidance and support during this project. Without this, the work will not have been completed and reach its conclusion on time.

Also, I would like to express my sincerest thanks to my wife, Mrs. Fathiy Tamzini and my parents, Mr. Jouma Aldawi and Mrs. Zina Daoo, who were always behind me and offered me the care and support that a child can ever have. Without them, I would have never accomplished this course.

At last, I would like to acknowledge Dr. Simon Fletcher and Mr. Alan Myers, for their help and advice on development of the new 3D measurement system.

Table of Contents

List of Figures

List of Tables

Equations

Glossary of Terms

3D: 3 Dimensions

BCF: Base coordinate frame

BFSK: Binary frequency shift keyed

CB: Camera coordinate

CCD: Charge coupled device

CH: Channel

CP: Calibration plate

DAQ: Data acquisition

DFD: Data flow diagram

DTI: Dial test indicators

FM: Frequency modulation

GUI: Graphic user interface

MFCW: A multiple-frequency continuous wave

MFCWFM: A multiple-frequency continuous wave frequency modulation

PGIA: Programmable gain instrumentation amplifier

PSD: Position sensitive diode

RH: Relative humidity

STFT: Short time fourier transform

TCF: Tool coordinate frame

TOF: Time of flight

Nomenclature

Ψ, θ, α, β: Angles

α_{refl}: Reflection coefficient

α_{refr}: Reflection coefficient

I: Ultrasound intensity

f: Frequency

M: Mass

T: Time (Chapter 4)

u, v, w: 3D coordinates of the transmitter (Chapter 4)

d: Distance

c: Speed of sound

t: Time of flight

φ: Phase shift

λ: Wavelength

ρ: Density

P: Pressure

μ: Ratio of major specific heats gas

R: Universal gas

t: Temperature (Chapter 5)

ω: Angular velocity $\omega=2\pi f$

v: Speed of moving object (Chapter 7)

X, Y, Z, X, x, y, z, x', y', z': 3D coordinates of the position

Chapter 1 Introduction

1.1 Preamble

The accuracy of machined components is one of the most critical considerations for many manufacturers. Great importance is laid on the consistency of the machine tool and its ability to accurately position the tool. Factors like cutting tools and machining conditions, resolution of the machine tool, the type of work-piece etc. all play an important role within the machine. Some errors occur when building machines or over time due to changes in environmental conditions (e.g. temperature within the workspace) or variations in cutting forces. Error due to the latter depends on the type of tool, work piece and the cutting conditions adopted.

Improving machine accuracy is a long-standing problem in the manufacturing industry and 3D measurement techniques for machine tool calibration have received considerable attention due to the unavailability of low cost and high accuracy measurement systems.

Measurement accuracy and environmental parameters are fundamental to the successful application of 3D measurement systems. In an integrated 3D system (Figure 1.1), the specifier provides the specific space location of the job. The trajectory planner is then activated, providing the time-history of the motion required to accomplish the specified task. The parameters of motion produced by the planner, namely the transmitter position, velocities and accelerations required, are then fed to the motion controller, producing the actuating values of torque (or forces) for each of the position spindles that will provide the planned movement of the 3D position. However, due to possible change in the surrounding environment and or uncertainties in the dynamic model of the spindle position used by the controller, some deviations in the position motion are expected.

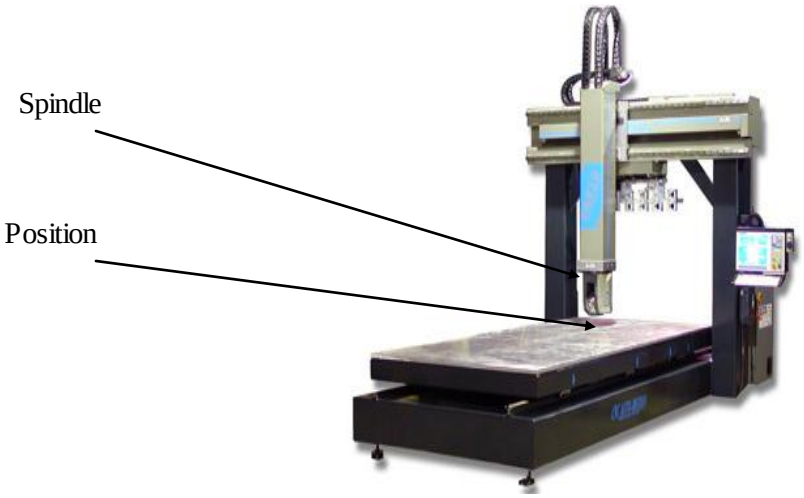

Figure 1-1 CNC for 3D Milling

Due to manufacturing tolerance, the position parameters of the dynamic model, including the reference position, distance between actual position and reference etc, of each 3D measurement device is slightly different from one to another. Also, changes to the surrounding environment, such as the external forces applied to the device, the parameter change of the dynamic model and, therefore, introduce error into the controller. Thus, to improve the accuracy of device control, a proper model for the system should be able to measure all the characteristics (position, velocity, and distance) accurately, and so determine the parameters of the kinematics and dynamic models of the system. With these measurements, it is possible to either calibrate the parameters off-line or configure the on-line closed-loop 3D system control, improving device accuracy.

Research into 3D measurement systems has been active since the beginning of 1900s. Hitherto, a number of 3D measurement systems have been successfully developed, among them laser tracking systems have already reached an accuracy of ±0.05mm [1, 2], or even better. Such systems can fulfil requirements for 3D measurement system parameter calibrations, but their price is normally high, and some may be even more expensive than the machine itself. In the case of off-line calibration, costs might not be an important issue, as the manufacturer can always use one standard 3D measurement system to calibrate a number of 3D machines. However, in the case where the 3D

measurement system is required as a part of the machine to form part of the on-line closed loop control system, or for condition monitoring the price of the measurement system becomes very important.

Ultrasonics, as a very economical technique, has been extensively developed for 3D measurement systems [3, 4, 5, 6, 7]. Previous ultrasonic 3D measurement systems have limitations on resolution, accuracy, flexibility and adaptability so the current project seeks to develop a new ultrasonic 3D measurement system for Cartesian and non-Cartesian machine calibration, which will demonstrate great improvements in the following aspects:

- High accuracy: Using TOF (time-of-flight) measurement, the accuracy of the previous ultrasonic 3D measurement systems was only between ±2.54mm [4] and 1mm [6], which is usually insufficient for machine calibration. In the proposed ultrasonic 3D measurement system for Cartesian and non-Cartesian machine calibration, the use of a multiple-frequency continuous wave frequency modulation (MFCWFM) technique, has achieved significant improvement in accuracy in the laboratory environment.

- High resolution: High measurement resolution is essential for capturing detailed position coordinates, which provide users with more information on accuracy, repeatability and other dynamic behaviour, thus validating calibrations of the dynamic model.

- Calibration of Cartesian-based and non-Cartesian machines: Procedures will be devised to calculate the geometric elements from 3D measurement data. This will solve calibration problems for many machine configurations.

- Good flexibility: Triangulation used in previous 3D measurement systems for positioning coordinates requires the receivers to be positioned orthogonally. This reduces the flexibility of the system and becomes impractical when more

receivers are used. Thus, in this project algorithms have been developed that allow three receivers to be arbitrarily located.

- Easier set-up procedures: This project allows receivers to be easily positioned, without using external equipment. This method will significantly simplify the set-up procedure of the tracking system, and hence will improve the system‘s flexibility, adaptability and speed of process, and minimise time required to collect data.

- Robustness against environmental disturbances: Ultrasonic speed drifting and echo interference are the major environmental disturbances to the ultrasonic tracking system. In this project, the problem of ultrasonic speed drifts has been solved by a novel method, which employs optimisation algorithms to estimate the best value of the ultrasonic speed, by multi frequency continuous wave frequency modulation techniques.

The system can then be used for online feedback in a condition monitoring system with automatic measurement of a machine tool and integration into a modern CNC controller.

1.2 Aim and objectives of the research

1.2.1 Aim

The aim of the research to design and produces an efficient, accurate, low-cost 3D measurement device based upon ultrasonic principles, which is suitable for calibration and monitoring of Cartesian and non-Cartesian machine tools.

1.2.2 Objectives

The distinct objectives in details:

1- To design a low cost technique for accurately measuring distances using an ultrasonic signal.

2- To investigate techniques for allowing for changing environmental effects (in particular temperature and humidity) in the workspace on the propagation of ultrasonic waves with reference to distance measurement.

3- To investigate techniques for compensating for ultrasound echoes in the workspace on ultrasonic distance measurement.

4- To design and produce a prototype ultrasonic multi-sensor 3D positional measurement significantly more accurate than current systems.

5- To produce measurement strategies for the efficient calibration of a 3-axis machine tool utilising the proposal 3D measurement device.

1.3 The Structure of the thesis

This thesis contains nine chapters that describe the research work performed in this project, leading to the improvements outlined above. It starts with a review of the previous research in the field of 3D measurement systems. In chapter 2, most of the past 3D measurement systems, based on different techniques are described. This includes the three cable tracking system, laser tracking system, and so on. Amongst them, laser tracking has the highest accuracy, but also the highest price. Therefore, in order to find an alternative solution for 3D measurement system with a lower price, a number of different 3D measurement systems have been developed, and each of them has its own relative advantages. The characteristics of these systems (cost, accuracy, portability, workspace volume and resolution, etc) are compared with each other at the end of the chapter, and summarised.

Chapter 3 provides a brief introduction on the relevant ultrasonic fundamentals. The contents of this chapter cover ultrasonic characteristics, ultrasonic transducers, transmitted ultrasonic signals and modern applications of ultrasound.

Previous work on ultrasonic 3D measurement system is then introduced and analysed in Chapter 4. First, the working principles of previous ultrasonic 3D measurement systems are introduced in terms of their coordinate positioning algorithm and the techniques used for distance measurement. The drawbacks of previous techniques for ultrasonic distance measurement systems are then considered, including the limitations of its measurement accuracy and resolution, and also its serious lack of flexibility and unsuitability for industrial implementation due to the complex set-up procedure that it requires.

The limitations of the previous ultrasonic 3D ultrasound system provided the motivation for the research described in this thesis, with the aim of improving the accuracy, resolution, flexibility and adaptability of the system. One prominent innovation has been the adoption of MFCWFM system measurement principles. The development of a MFCWFM 3D measurement system is described in detail in Chapter 5. A number of difficulties had to be overcome in this development, including evaluated temperature and humidity and receiver positioning. Data Flow Diagrams (DFD) are introduced in the chapter, as efficient means for modelling the measurement system functionality, regardless of the implementation issues.

With the new techniques and algorithms introduced in Chapter 5, a prototype of the new 3D measurement system has been developed. The hardware implementations of this prototype involved the design and development of the transmitter and dual functional receivers. The principal circuit diagrams of these hardware items are given in Chapter 6 accompanied by detailed descriptions. Following the hardware implementations, issues concerned with software developments of the prototype are also presented. The software (LABVIEW) provides a simple GUI (graphic user interface) with the functions of data collecting, processing, displaying and storage.

In a complex industrial environment factors such as the air temperature, humidity and ultrasound echoes can seriously affect the accuracy of the system. Therefore, in Chapter 7 the new frequency measurement technique was shown to have good resistance to echo interference. Also in Chapter 7 the experiments show that the evaluation of temperature and humidity in the workspace area was successful by reducing variation and increasing the accuracy of the measured distance.

The testing of the new 3D measurement system in a series of experiments is described in Chapter 8. First the MFCWFM system was tested on Zeiss CMM and then on Geiss machine. Then, a number of measurements were made at varying distance at difference times on three axis (x, y, z) and compare the results with XL-80, eTALON and DTIs systems. Finally, the new 3D measurement system was tested experimentally, when the position of the moving transmitter was measured in different position at workspace area, and high accuracy obtained. During the experiments, the procedure for receiver positioning was demonstrated in detail.

Finally, Chapter 9 describes contributions to knowledge made by this research, particularly the innovations which have achieved significant improvements in the overall performance of ultrasound 3D measurement systems. Suggestions for future research are then made for further improvements in ultrasound distance measurements.

Chapter 2 Review of 3D measurement

2.1 Introduction

The purpose of this chapter is to introduce the past research work on 3D measurement systems and provide a critical overviews of this research area. The general function of 3D measurement systems is to monitor the actual position of a specified coordinate, and feed the information back to a system controller to achieve a more accurate and higher performance.

The coordinates of a position can be determined as either the absolute position or orientation in a certain coordinate system [1, 8, 9, 10, 11, 6, 12, 13, 14, 15, 16] or the relative position according to the movement of an object [3, 4 , 5 , 7, 17, 18, 19]. This information can be fed back to the system controller either in real-time to perform closed loop control, which provides a higher reliability and accuracy, or it can be used to realise the off-line calibration of the system.

The accuracy of most industrial robots and machine tools (the ability to attain a specified position in space) is usually much worse than their repeatability (the ability to return repeatedly to a given position). In theory, it is possible to improve the accuracy so that it is as good as the repeatability. The inaccuracy comes from manufacturing tolerances in the production of each part of the system. Accordingly, a production machine must be calibrated by the manufacturer and periodically re-calibrated by the user to maintain its accuracy.

The methods for 3D position measurement are divided into two basic categories. The first uses non-contact systems, including all optical and ultrasonic systems. The second includes all cable-driven systems. Due to the varied practical requirements, different equipment, tools and methods are employed to solve 3D measurement system problems. These techniques are classified as:

Contact 3D measurement systems:

- Fohanno's method
- Three-cable techniques

Non-contact 3D measurement systems:

- Optical measurement systems
- Ultrasonic measurement systems

In the following sections, each of these techniques will be introduced and discussed with their applications.

2.2 Contact 3D measurement systems

In this case, the coordinate of the position is measured by the instrument in a contact manner, i.e. during the measurement there must be some physical contact between the position and the instrument. This leads to the limitation that these techniques can only be applied for off-line calibration of the machine. The main drawback of this kind of system is that the force exerted on the position through the physical contact can bring significant error to the measurement. However, due to their portability and low cost, they are still attractive in some applications.

In this section, two contact measurement systems (methods) are introduced; three-cable tracking system and Fohannos method.

2.2.1 Fohanno's method

Fohanno's method for coordinate position determination is described only briefly [20]. As shown in Figure 2.1(a), six sensors are located on three orthogonal plates mounted to the machine, and the readings from sensors are taken and used to calculate position and orientation with respect to an arbitrarily placed cube. The array of sensors is then

positioned to have all three plates parallel to faces of the cube. The sensors provide an output proportional to the distance between the sensor itself and the cube face. Figure 2.1(b), shows one aspect of this measurement.

The orthonormal reference of the sensor array is represented as (o, i, j, k) and that of the cube as (o', i', j', k'). The measurements taken by the sensors are X1, X2, Y1, Y2, Z1, and Z2

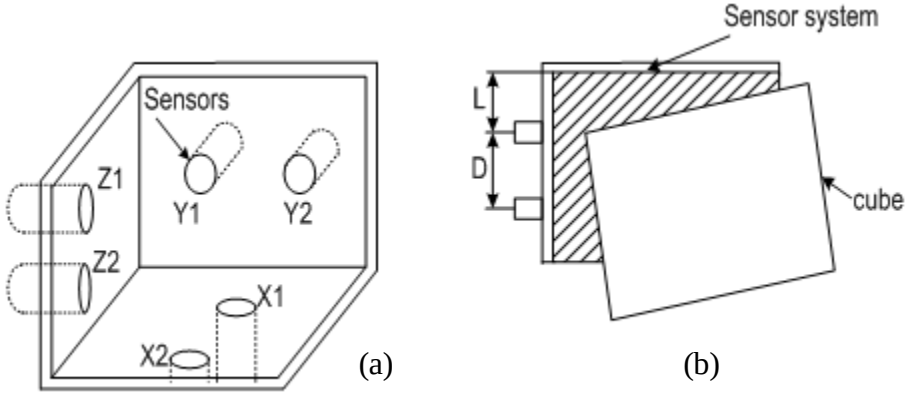

Figure 2-1 Fohanno's sensor system

For small angles, the orientation of the sensor array with respect to the cube is given as:

$$\psi = \frac{X_2 - X_1}{D} \qquad 2\text{-}1$$

$$\theta = \frac{Y_2 - Y_1}{D} \qquad 2\text{-}2$$

$$\phi = \frac{Z_2 - Z_1}{D} \qquad 2\text{-}3$$

Where D is the distance between sensors in the same plane as shown in Figure 2.1(b), and the angles, ψ, θ and φ are given in radians.

These equations hold only for very small angles, so that $\alpha \approx \tan\alpha \approx \sin\alpha$.

Fohanno also expressed the displacement from o to o'.

$$X' = X_1 - \psi(L - Y_1) + \phi(L - Z_1) \qquad 2\text{-}4$$

$$Y' = Y_1 - \theta(L - Z_1) + \psi(L - X_1) \qquad 2\text{-}5$$

$$Z' = Z_1 - \phi(L - X_1) + \theta(L - Y_1) \qquad 2\text{-}6$$

2.2.2 Three-cable tracking system

Fohanno also introduced a 3-cable triangulation technique for solving the assessment problem of the system manipulator [20]. The three-cable triangulation technique relies upon measurement of three distances from the position to three datum points, followed by simple triangulation calculation yielding *x*, *y* and *z*.

The measurement is achieved by using a spring-return drum, around which the wire is wound, the rotation of which is measured by a potentiometer or an encoder. There are three drums, one for each of the *x*, *y* and *z* coordinates. By measurement of the angle through which a drum has rotated, the length of cable paid out may be determined and, hence, the distance is measured. The wires are maintained under constant tensile force of the drum spring to about 1Kg, the main drawback of this technique is that variable forces are applied to the position, producing artificial dynamic results.

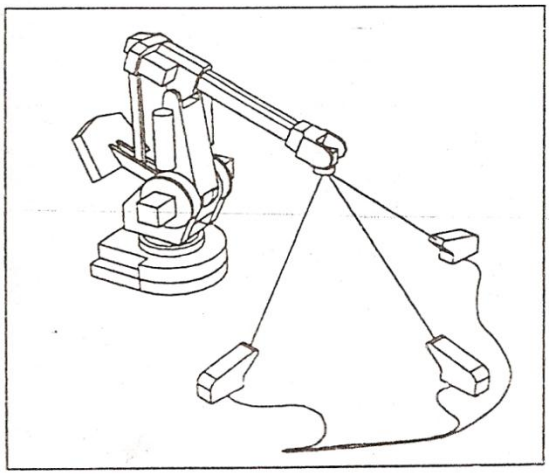

Figure 2-2 Three-cable tracking system

Figure 2.2, shows how the system manipulator may be tested by this method. The three drums are located around the manipulator work area at know relative spacings.

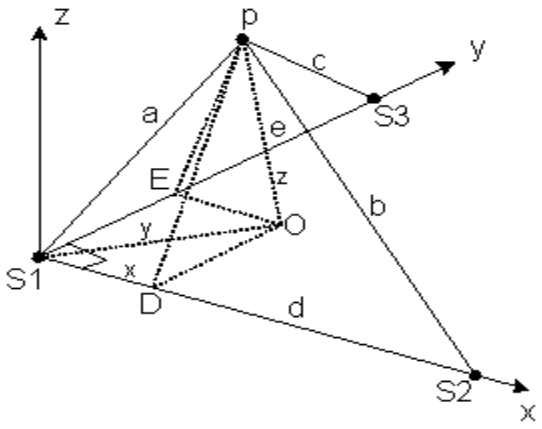

Figure 2-3 Three-cable technique coordinates

It is common to arrange the three sensors orthogonally, so that the 'corner' sensor can be considered the origin of measurement's frame of reference. The situation is then as shown in Figure 2.3, where *a, b* and *c* represent measured distances, and d and e represent the fixed distances between the sensors and *x, y* and *z* are the coordinate values of the

position. The sensors are denoted by S_1, S_2 and S_3, with point P, representing the position to be determined. The three coordinates are given by the following equations:

$$x = (a^2 + d^2 - b^2)/2d$$
$$y = (a^2 + e^2 - c^2)/2e$$
$$z = \sqrt{a^2 - x^2 - y^2}$$

Knowing, *a, b c*, d and e, the 3D coordinates position of *P(x, y, z)* can be determined.

The disadvantage of a three-cable measurement system is that variable forces applied on the position result in errors in the measurement. Importantly, it is not capable of dynamic measurement. To achieve high performance dynamic measurements, a non-contact measurement system is necessary.

The system described by Legnani [21] uses cheaper equipment but a rather complicated procedure for orientation and position measurement. Because of its configuration, the system is only capable of off-line use, in this case measuring the orientation calibration.

2.3 Non-contact 3D measurement systems

With a non-contact measurement system, the 3D position is measured without any physical contact, using electromagnetic or acoustic waves, such as laser, light, or ultrasound. These offer advantages of higher flexibility and adaptability to many different applications. Also, high performance dynamic measurement is possible without direct contact with the position and, importantly, they can perform online measurement without disturbing the normal operation of the 3D position. They can be integrated into the 3D measurement control system as a part of the control loop.

According to the different measurement intermediates used, non-contact 3D measurement systems can be divided into two categories: optical and ultrasonic measurement systems.

2.3.1 Optical measurement system

Laser tracking

The extremely high accuracy of laser measurement offers the opportunity for the most successful tracking system yet developed. In the past decade, a number of researchers have focused on laser tracking and its applications [22, 23, 24, 25] and significant improvements have been achieved. The specification of the Optotrac dual-beam laser measurement system is shown in Table 2.1 [9].

Table 2-1 Optotrac specifications

Measurement volume	Up to 3×3×3m
Repeatability	0.0005% of measurement field
Accuracy	0.025% of measurement field
Sampling rate	Selectable up to 1KHz
Control	User interface on PC Digital I/O lines

Certainly, this system provides a very high performance in 3D measurement. But the price of this tracking system is extremely high, up to £100,000.

Vince developed a similar laser tracking system that used one laser beam instead of two for 3D position measurement [24]. In this way, with less equipment, the system cost is reduced, but remains high. The working principle of this system is based on a polar configuration, as shown in Figure 2.4.

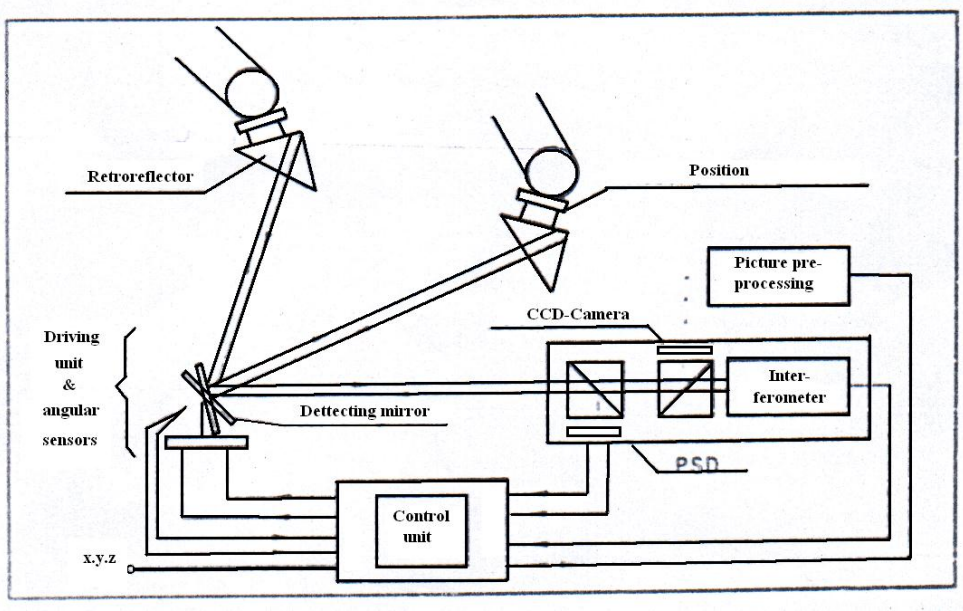

Figure 2-4 Functional principle of the laser tracking system

The beam of a high-speed HeNe laser-interferometer is deflected by a plane mirror fixed to a high-precision universal joint and hits the retro-reflector that is mounted on the system's position. The retro-reflector or comer cube consists of three mutually perpendicular plane mirrors that reflect the beam back on a path parallel to that of the incident beam. The reflected beam is again deflected by the plane mirror and directed via beam splitters to a position sensitive Diode (PSD) and a CCD (Charge Coupled Device) camera.

Ideally, the laser beam hits the centre point of the retro-reflector, causing no parallel displacement between the emitted and the reflected beams. When the system starts moving, the laser beam no longer hits the centre point of the retro-reflector, which results in a displacement of the reflected beam. This displacement is measured by the PSD and constitutes the tracking error. The tracking controller minimises the tracking error by turning the axes of the Universal joint, which allows the laser beam to follow arbitrary movements of the retro-reflector.

The position of the system is defined to be the focal point of the retro-reflector. The orientation of the plane mirror can be calculated from the beam length, and the beam displacement ascertained. The interferometer is used to measure the beam length between the plane mirror and the retro-reflector, based on the heterodyne principle. Two laser rotary encoders, one at each of the Universal joints, determine the angles of rotation of the plane mirror in the x, y and z planes. The PSD provides a measure of the displacement of the reflected laser beam from the middle position. These two signals provide both position measurements and also feedback to the measurement controller, where the position can be determined.

To measure the orientation of the position (see Figure 2.5), a plane mirror is attached to it and it is driven along a straight path parallel to the laser beam and the mirror. The beam is directed toward the mirror by means of a beam splitter and the reflected beam passes through the beam splitter and shines onto a screen. Any error in the orientation of the position (and hence the mirror) will deflect the beam away from a "zero" spot on the screen by a certain distance, which will be an indication of the amount of the orientation error.

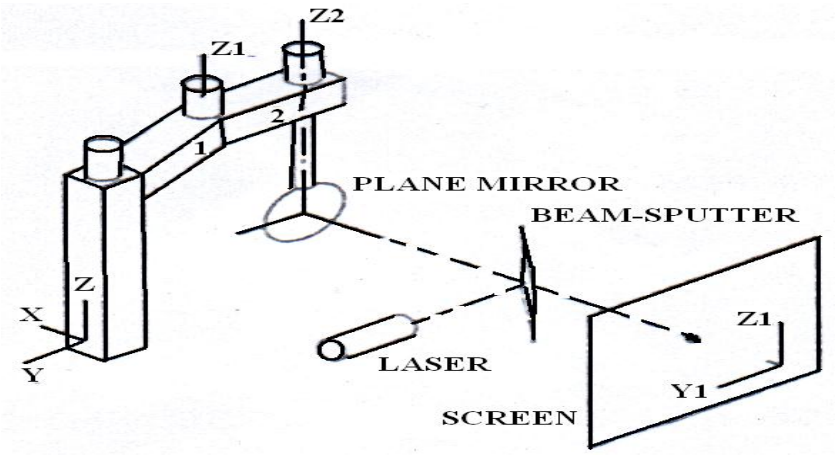

Figure 2-5 Scheme for the measuring system of the angular error of position

On the other hand, for displacement error measurement, the system is reconfigured as shown in Figure 2.6, where a lens is used as the target instead of the plane mirror. In this

way, the laser beam passes through the lens and reaches the screen as a more or less diffused spot, which is deflected if there are positional errors. A CCD (charge-coupled device) video camera can accurately measure the shift of the laser spot on the screen using suitable image analysis software and hence determine the displacement error of the position.

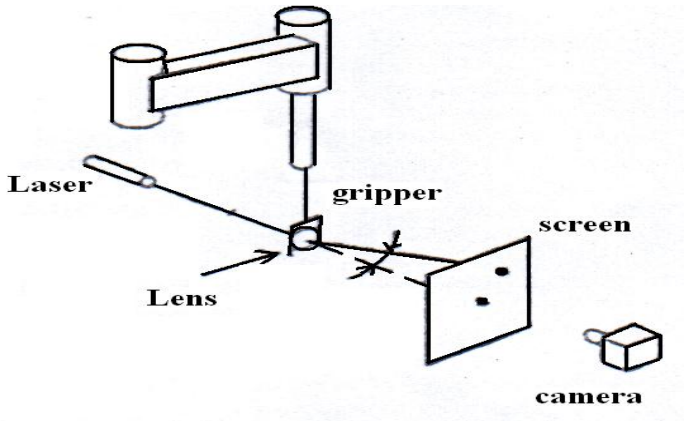

Figure 2-6 Scheme for the system of the position displacement measurement

Unlike other laser 3D measurement systems introduced so far, the laser tracking system introduced by Yuan and Fu [26] uses an optical sensor attached to the position instead of a reflector, while the laser scanners cast light planes to trace the sensor's movement.

As shown in Figure 2.7, the optical sensor (an exaggerated rectangular plate) is attached to the position of a planar system and shares the same coordinates as the TCF (Tool Coordinate Frame). Two laser scanners cast light stripes toward the system workspace to form a pair of cross hairs. Each scanner aims at one of N possible angles and results in N2 possible nodes in the Base Coordinate Frame (BCF). During measuring, while the pair of crossing hairs project onto the sensor, by knowing the stripes' coordinates in both TCF and BCF, the transform relating the two coordinate frames can be derived and, thus, the orientation and position can be determined.

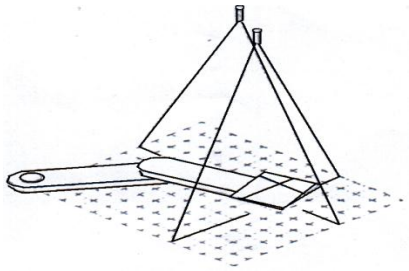

Figure 2-7 Two-DOF measurement setup

In this section, several different methods for 3D measurement using lasers have been presented. All of these systems provide very high accuracy in measuring the position. Due to the distinct advantages of dynamic measuring and on-line calibration, people have more interest in the first two laser measuring systems [24, 9]. With similar techniques, similar measuring systems with one, two, three or four laser beams have been developed, and some research has been carried out to enhance the performance of such systems.

The work on the last laser measuring system introduced above was found in a publication by Yuan and Fu [26]. It was an innovative configuration, where, instead of a reflector (as in the other laser measurement systems introduced) an optical sensor is attached to the position. This results in a simpler and hence cheaper method for dynamic laser measurement system. However, the prototype of such a system was only tested for two-DOF measurement and no 3D dynamic measurement has been demonstrated.

eTALON - NPL Laser tracer system

The UK National Physical Laboratory in partnership with eTALON has launched a new high accuracy measurement system for calibration of CNC machine tools, as shown in Figure 2.8. The NPL claims that the system will bring laboratory accuracy to the shop floor [27] .

Figure 2-8 National Physical Laboratory laser tracer

This system uses a laser to track a reflector mounted on a CMM or machine tool, and an associated software package, to provide an innovative system which claims to have reduced horizontal and vertical guidance errors to less than 0.2µm, and achieved a centre of rotation stability to less than 0.3µm. Mounted inside the laser to form a tracer system is a high precision reflecting sphere with a claimed radial deviation of less than 50nm. This reflector is decoupled from the tracking mechanism, resulting in sub-micron stability during movement of the interferometer and gives a maximum range of 6m. However, the system requires highly trained personnel to set up and is expensive.

Renishaw XL-80 laser measurement system

The Renishaw XL-80 laser measurement system, as shown in Figure 2.9, offers high performance calibration for motion systems, including CMMs and machine tools. The XC-80 contains a device which accurately measures local air temperature, air pressure and relative humidity, and changes in these conditions are automatically compensated for in any measurement readings taken. The resulting linear measurement accuracy is claimed to be better than ±0.5µm with a maximum linear measurement speed of 4m/s.

Figure 2-9 Renishaw XL-80 laser measurement system

The compensator readings can be taken at up to 50kHz, and a linear resolution of 1nm is claimed. The disadvantage of this system is its high cost and that it is limited to measurement along a single line [28], therefore 3D measurement requires synthesis of several measured error.

Due to the high expense of the laser measurement systems, they are not usually integrated into the 3D measurement system in practice to perform close-loop control or no-machine monitoring. (The tracking system itself may be even more expensive than the machine being measured). Additionally, measurement in such systems can suffer from obstacles involved in the workspace. These problems can be solved by using the visual or ultrasonic measurement systems, which are introduced next. The paper by Zhuang and Roth [22] addresses error modelling issue for laser measuring coordinate systems, which is crucial in the accuracy enhancement of such systems.

Visual measurement system

Vision-Guided 3D systems have been a topic of continued interest for the past three decades. Distinct enhancements have been achieved during this time, and vision techniques have been applied in 3D measurement systems more and more widely. In

Vision-Guided 3D measurement systems, the vision systems are normally used to recognise or track the work pieces, landmarks or the environment, and feed back useful information to the controller to perform efficient and reliable control after proper image processing. Visual measurement is one of the applications of Vision-Guided 3D measurement systems.

This section introduces two alternative vision systems calibration, both of which demonstrate good performance with relatively low cost. However, they are both designed for off-line system calibration and are thus incapable of online dynamic measurement.

Compared to laser measurement systems, the visual measurement system offers advantages of higher adaptability and flexibility and lower price. In this section, some applications of 3D measurement, using a vision technique are introduced. Figure 2.10, shows a vision system presented by Preising and HSIA [10] for 3D calibration, involving a single camera and a calibration plate which is used as a target.

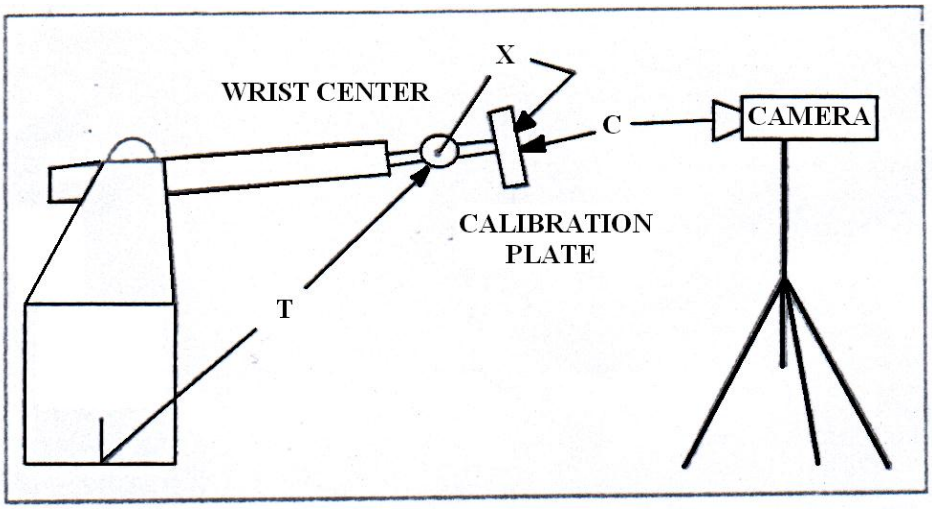

Figure 2-10 3D computer vision and system set-up

Camera calibration for 3D-computer vision requires the internal camera geometric and optical characteristics (intrinsic parameters) to be determined, as well as the position of the camera frame relative to a certain world coordinate system (extrinsic parameters). Once calibrated, position information of the calibration plate (CP) coordinates or world coordinate system with respect to the camera's coordinate (CB) system can be obtained from the camera image.

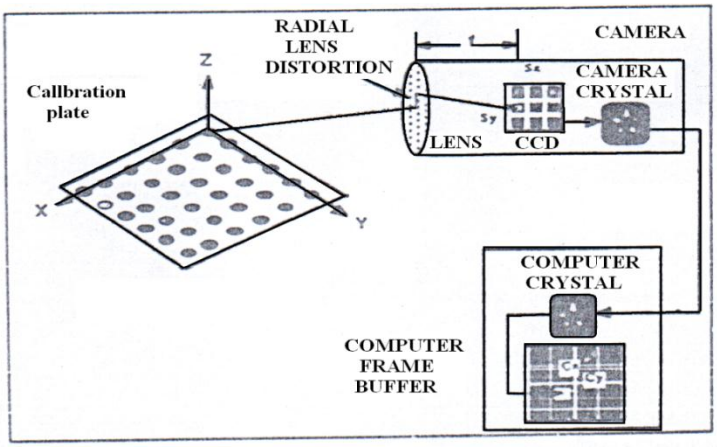

Figure 2-11 Schematic diagram of the Two-Stage Camera calibration process

The camera's intrinsic parameters are determined, using a least squares fit algorithm with a reference plate representing a known world coordinate system, as shown in Figure 2.11. After camera calibration, this same plate is used for convenience as a target for the camera system to measure. Uning a commercially available computer controlled Deadal XYZ positioning table [Deadal Incorporated] and a Zeiss (Nr 134240) rotary table, measurement of the position of the calibration plate is achieved. This method provided very high performance measurement, and was employed to calibrate the repeatability and accuracy of the 3D measurement system. In both cases, the manipulator was pre-programmed to reach one or more specific positions. As presented in Preising and HSIA paper [11] , 500 repetitions of one position were measured for repeatability assessment and 100 different positions were tested to estimate the system accuracy.

The ‘Eye in Head’ system is a very popular application of vision guided 3D systems. In such a system, instead of fixing the camera stationary at some specific place independent of the system, the camera is mounted on the position to build a hand-eye coordinate for the system. Albada and etal [29] presented a novel method to calibrate the system using its onboard “eye” and an external reference plate. The prototype performed the measurement of the system position in a volume of 1m. The system had high accuracy of 0.20mm. The measurement procedure began with the selection of the model parameters of the system that needs to be pre-determined. Using this set of model parameters, the position generation program could generate a set of measurable positions that allow computation of the desired parameters.

Using these positions, a system program is generated which directs the system along a path containing these positions. At each measuring position, the system stops, and one or more images of the reference plate are obtained. The actual parameters at the measuring position must be recorded. Next, the images obtained are processed off-line, to obtain the position of the camera relative to the reference plate, plus the parameter of the camera. This “photogrammetric procedure” can be made self-calibrating when a collection of sufficiently different images is available. The positions are obtained by iterating two tasks: the image-processing procedure and the image-reconstruction procedure. The former tries to recognise and identify the markers on the reference plate and to determine their positions in the image, the latter fits a model that can predict the position of the markers in every image by the computation of the camera position for each image and the camera parameters. The predictions are fed back to the identification part of the image-processing procedure. Using the calibration procedure developed at IPK Berlin, the unknown system parameters, plus the position of the reference plate relative to the system base, can be derived from these measurements.

2.3.2 Ultrasonic measurement system

In 3D measurement systems ultrasonic signals may be applied for range finding in a mobile measurement system [30, 4, 5, 6, 7]. Because the acoustic properties of air vary

with temperature, humidity, presence of dust, etc., airborne ultrasonics has rarely been used in applications where high accuracy is required. However, in view of the simplicity and low cost of ultrasonic systems, research on an ultrasonic 3D measurement system was started in the middle of the 1980s [31]. This aimed to develop a cheap 3D measurement system that could be integrated into the robot system as a part of its servo-control loop. The details of previous and current research on particular ultrasonic 3D measurement systems will be presented throughout the rest of this thesis. First, in the next section, another ultrasonic system that is capable of 3D positioning is introduced.

Ultrasonic spatial locating system

This system presents a measurement technique which can locate points within a 500mm cube to an accuracy of approximately 1mm, it has the advantage of being practically unrestrained and can provide spatial position information in real time [32]. The technique involves measuring transit times of high-frequency sound between the point of interest and a coordinate system. The system includes a microcomputer-based processor and controller, which performs the necessary calculations and is capable of self-calibration and error checking.

The basic measurement principle uses the fact that an electrical spark discharge radiates a high frequency ultrasonic wave, which travels spherically outward at the speed of sound. If the transmission time of that wave can be measured, then the distance travelled can be computed by knowing the local speed of sound. Figure 2.12, shows a functional diagram of the measurement system.

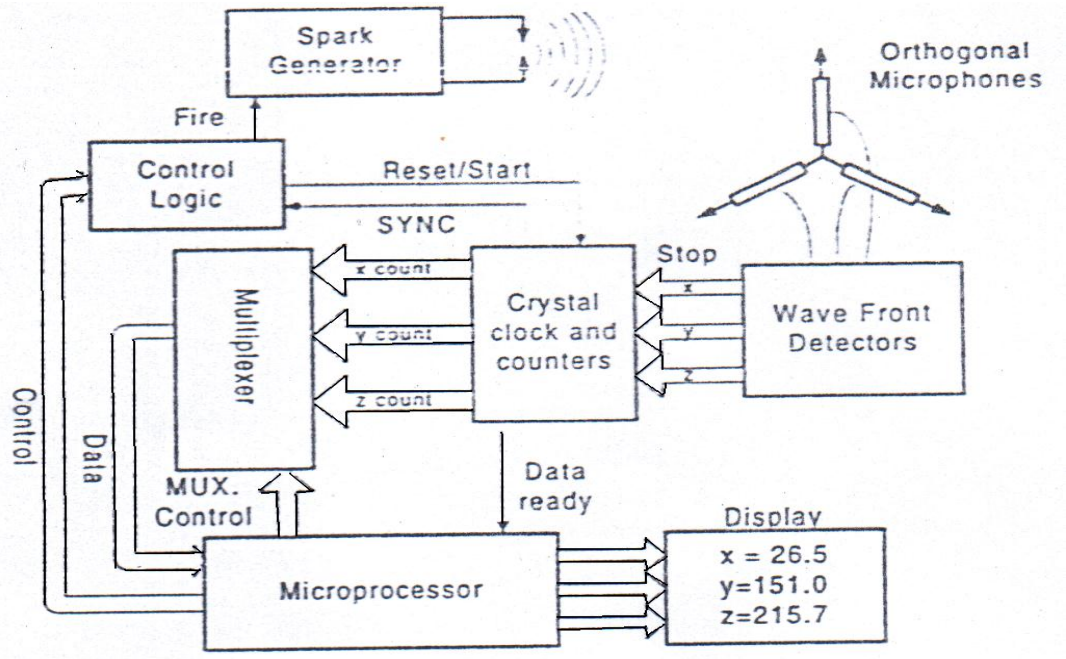

Figure 2-12 Functional block diagram of the ultrasonic spatial locating system

In order to calculate the coordinates of the spark, the equations shown in Figure 2.13 are used.

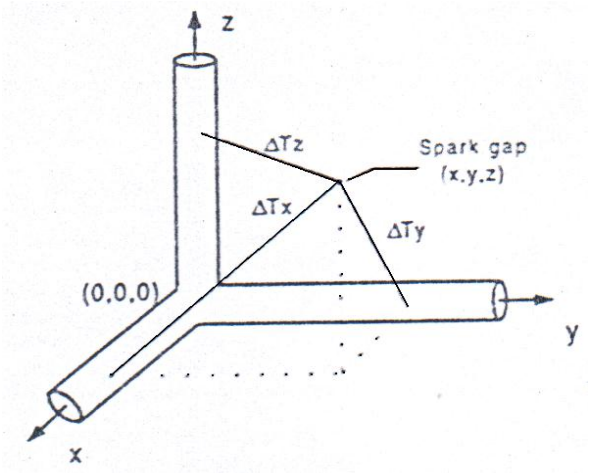

$$x = v\sqrt{\frac{(\Delta T_y)^2 - (\Delta T_x)^2 + (\Delta T_z)^2}{2}}$$

$$y = v\sqrt{\frac{(\Delta T_x)^2 - (\Delta T_y)^2 + (\Delta T_z)^2}{2}}$$

$$z = v\sqrt{\frac{(\Delta T_x)^2 - (\Delta T_z)^2 + (\Delta T_y)^2}{2}}$$

Figure 2-13 Coordinate system formed by the linear microphones and the equations used to compute coordinates from the transit time intervals

In the usual mode of operation, a series of 8 sparks are fired sequentially and the transit time for each stored in the computer memory. Following the eighth spark, the 8 transit

times are averaged and a standard deviation calculated. The standard deviation is checked to verify that no spurious signals have been received. The calculation of the spatial location of the spark is then completed by applying the equations shown in Figure 2.13 to the computed average transit-time intervals. The calculation time for determining the coordinates of the spark is approximately 150ms.

Since the position locating system is intended to be used in ordinary room environments, no special precautions were taken initially to control the environmental conditions so the results include errors due to small atmospheric changes, as well as system errors.

3D measurement systems with economical ultrasonic transducers

This ultrasonic 3D measurement systems were developed to estimate the location of a wave source in real-time, using a simple triangulation technique that has also been used for the three-cable tracking system [3, 4, 5, 7]. But in this case, the three distances to the surrounding receivers were measured using the ultrasonic TOF technique with the ultrasonic transmitter mounted on the position. While accuracy of between ±2.54mm [4] (and 1mm [6]) has been achieved, and there is good potential for further development, such a measuring system has limits on its accuracy, resolution and practicability, which seriously restricted its implementation in real industrial applications. As these ultrasonic 3D measuring systems were used as the starting point for current work developing an enhanced system, the full details of these systems will be presented later in Chapter 4.

2.4 Summary

In order to perform both static and dynamic calibration, close-loop feedback control and off-line programming of the 3D measurement system, a reliable 3D measuring system for position determination is required. In the past three decades, a number of researchers have been in this area, and different 3D measuring systems employing different technologies for different applications have been developed. In this chapter, an overview of these 3D measuring systems was provided by classifying them into contact and non-contact 3D measuring systems. For both groups, a few representative 3D measuring systems are introduced. Here, the advantages and disadvantages of these systems are summarized:

Contact 3D measurement systems

Two contact techniques were introduced in this Chapter, they are Fohanno's and a three-cable method. 3D measurement systems employing these techniques are cheap, portable and easy to set-up. However, the drawback is that variable forces applied on the position cause errors in the measurement, and such systems are not suitable for dynamic measurement, especially when the position is moving fast or performing complicated movements. Perhaps more importantly, the system cannot be left 'in situ' for condition monitoring.

Non-contact 3D measurement systems

With non-contact 3D measurement systems, there is no physical contact between the measurement instruments and the position. Therefore, it is possible to validate high performance of dynamic 3D measurement. Normally, such systems perform a very accurate and reliable measurement of the position. The non-contact 3D measurement systems were divided in two categories, optical and ultrasonic measurement systems, and the optical measurement systems were subdivided into laser and visual measurement systems.

The laser measurement system is the most accurate measurement system that has been developed. It provides a very high performance, but such systems are relatively expensive, which limits the application of such systems in industry.

Compared to laser measurement systems, visual measurement systems are cheaper and give acceptable accuracy in static calibration of the position. However, due to today's limited image processing techniques, the measurement requires the presence of specially designed marks, which restrict its application for on-line calibration, and normally the calibration volume is very limited.

The ultrasonic 3D measurement systems allow a simpler and cheaper measurement of the position. Since the measurement is based on "time-of-flight", the method can be easily affected by temperature, humidity and air etc. The accuracy of ultrasonic 3D measurement systems is relatively low compared to the others.

Table 2.2 compares the characteristics of different 3D measurement systems. It is hoped that the table will be helpful for the reader when reviewing past researches in the particular area of 3D measurement system.

Table 2-2 Characteristics comparison of the different 3D measurement systems

	Contact measurement systems		**Non-contact measurement systems**			
				Vision		
	Fohanno's method[3]	**Three-Cable[1]**	**Laser**	**Camera**	**Eye-in-Hand**	**Ultrasound[4]**
Accuracy	N/A	<1mm	±0.2μm	0.5mm 0.2degree	0.2mm 0.2minute of arc	between ±2.25 to 1 mm
Repeatability	N/A	<0.5mm	1μm	0.2mm 0.03 degree	N/A	N/A
Measuring Volume	N/A	2×2×2m (local)	6m	N/A	1×1×1m (local)	2×2×2m (global)
Expense	N/A	Low	£130000	Medium	Low	Low
Portability	Good	Good	medium	Medium	Very good-[2]	Poor

(1) This item is also called as dynamic resolution, it is only available with the 3D measurement systems able to perform dynamic measurement.

(2) Calibration with the eye-in-hand system, the portability is very good only for the 3D measurement system on which the eye-in-hand system has already been assembled.

(3) Fohanno's method is only a suggestion for 3D system calibration, no experimental work was performed on this particular method.

(4) The parameters are according to the ultrasonic 3D measurement systems developed by Mahajan, Ray, Jimenez and Martin [4, 5, 6, 7]. These particular systems aren't mentioned in this chapter, but it will be described in detail in later chapters.

Chapter 3 Overview of ultrasonics

3.1 Introduction

Sound waves which have frequencies higher than those to which the human ear can respond (about 20 kHz/s) are known as ultrasonic. Unlike light waves which are electromagnetic, ultrasonic waves are mechanical, often generated by the vibration of a body (though other sources such as electrical discharges and whistles can be used) and propagate as the vibration of the elementary particles in a compressible medium through which the longitudinal waves are passing. In the ultrasonic 3D measurement systems that will be described in the following chapters, airborne ultrasound is used as the medium for distance measurements. However, due to the relatively unstable characteristics of the air through which the wave is passing, high accuracy distance measurement is hard to achieve, when compared with e.g. the optical techniques introduced in the last chapter. This chapter briefly introduces the fundamentals of airborne ultrasound, and some modern applications of ultrasonics.

Firstly, the essential characteristics (i.e. velocity, reflection, refraction and attenuation) of airborne ultrasound are introduced, and how they are related to environmental factors. Next, airborne ultrasound transducers are introduced and the mathematical models of the generated ultrasound are also given. At the end of the chapter, some modern applications of ultrasonics are briefly summarised.

3.2 Characteristics of airborne ultrasound

As airborne ultrasound is used for distance measurement in the ultrasonic 3D measurement system, a good understanding of its characteristics is essential for accurate 3D measurement. Thus, before starting on the details of the measurement systems, relevant aspects of airborne ultrasound are reviewed.

3.2.1 Velocity

The propagation velocity of airborne ultrasound is an important parameter used in ultrasonic distance measurements as either a constant or a predetermined known value. Thus, a good determination of the ultrasound velocity is essential for high accuracy distance measurements, shown in the following equation

$$c = \sqrt{\frac{E}{\rho}} \qquad 3\text{-}1$$

Where, E refers to elasticity or pressure and ρ is the local density of the air. Strictly the equation refers to adiabatic transmission, but ultrasound is a good approximation. In the case of air, the ambient pressure remains almost constant, but when the temperature increases, the expansion of the air causes its density to decrease. From equation (3-1) we see that the ultrasound velocity will also increase. The relationship between the ultrasound velocity and air temperature, T, can be approximated linearly with a rate of 0.61m/s/°C, as shown in the following equations:

$$c = 331.4 + 0.61.T \qquad 3\text{-}2$$

Where T is the air temperature in degrees centigrade and the constant 331.4 is the ultrasound velocity at 0°C, in meter per second.

With equation (3-2) the ultrasound velocity can be accurately estimated from the air temperature. However, in many engineering tasks, including ultrasonic 3D measurement system, a more accurate value of the ultrasound velocity is required, thus some specific instrument or techniques are needed. Yang and Yuan [33, 34] applied techniques for high accuracy ultrasound velocity measurement. In Chapter 5 of this thesis, MFCWFM developed specifically for this project [35] to improve the accuracy of ultrasonic velocity measurement is presented.

3.2.2 Reflection and refraction

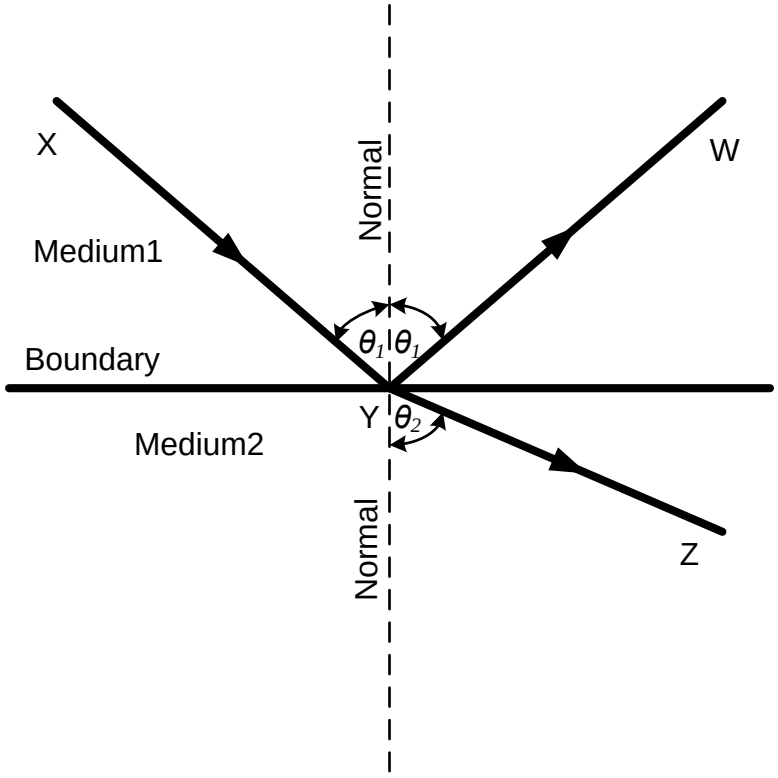

Figure 3-1 Reflection and refraction of an ultrasound beam incident to a plane boundary separating two mediums

Figure 3.1 shows a beam of ultrasound, *XY*, incident on a plane boundary separating medium 1 and 2, *Y* being the point of incidence on the boundary. *YW* and *YZ* are the respective reflected and refracted sound waves. θ_1 and θ_2 represent incidence angle and refraction angle respectively. The reflection angle is the same as the incidence angle θ_1, and the refraction angle θ_2 can be evaluated with the following equation:

$$\frac{C_1}{\sin\theta_1} = \frac{C_2}{\sin\theta_2} \qquad 3\text{-}3$$

Where, C_1 and C_2 represent the ultrasound velocities in medium 1 and 2, respectively. Equation (3-3) is only applicable, when the incident angle θ_1 is smaller than the critical angle θ_c, which totally depends on the two mediums, as in the following equation:

$$\theta_c = \frac{C_1 \sin\theta_c}{C_2} \qquad C_2 > C_1 \qquad 3\text{-}4$$

If the incident angle is bigger than the critical angle, then there will be no refraction wave at all. For example, if medium 1 and medium 2 are air and steel respectively, the critical angle is calculated as 3.15^0. This analysis pre-supposes that the solid has an ideally smooth and flat surface.

At the boundary, the ratio of the acoustic intensity of the reflected wave to that of the incident wave defines the reflection coefficient, α_{refl}, and the ratio of the intensity of the refracted wave to that of the incident wave is called the refraction coefficient, α_{refr}. These coefficients can be evaluated with the following equations:

$$\alpha_{refl} = \left(\frac{R_2 \cos\theta_1 - R_1 \cos\theta_2}{R_2 \cos\theta_1 + R_1 \cos\theta_2} \right)^2 \qquad 3\text{-}5$$

$$\alpha_{refr} = \frac{4R_1 R_2 \cos\theta_1 \cos\theta_2}{(R_2 \cos\theta_1 + R_1 \cos\theta_2)^2} \qquad 3\text{-}6$$

Where, R_1 and R_2 are the characteristic acoustic impedances of medium 1 and 2 respectively. The characteristic impedance of some commonly used materials are shown in Table 3.1 and, by applying equation (3-5) and equation (3-6), the reflection and refraction coefficients can be easily calculated. For example, assuming that medium1 and medium 2 in figure 3.1 are air and steel respectively, and the incident angle θ_1 equals θ^0, which indicates that the incident ultrasound beam is orthogonal to the boundary, then by applying equation (3-5) the reflection coefficient α_{refl} can be determined as 0.99998.

Table 3-1 Characteristic impedance for some commonly used materials.

Material	**Velocity of ultrasound wave in material (m/sec)**	**Density $(g/cm)^3$**	**Characteristic impedance $(kg/m^2.\ sec)$**
Aluminium	6,400	2.7	1.7×10^7
Steel	6,000	7.8	4.7×10^7
Water	1,500	1.0	1.5×10^6
Air	331	0.0013	430
Hydrogen	1,300	0.00090	110
Oxygen	320	0.0014	450

3.2.3 Angle of the ultrasound beam

The flat surface of an ultrasonic crystal driven by a continuous sinusoidal electrical signal will vibrate this vibration propogates through the air, generating longitudinal waves. The sound pressure in front of the crystal surface in fraunhofer region for a circular piston is obtained from:

$$p = \left(\frac{p'\pi a^2}{r} e^{j(\omega t - kr)}\right)\left(\frac{2J_1(ka\sin\theta)}{ka\sin\theta}\right)$$

Where:

P = pressure at distance r

P' = pressure at face of the piston

ω = angular frequency

k = wave number

a = crystal radius

θ = angle

J_1 = Bessel function of the first kind

Figure 3.2 shows the polar diagram of a crystal with radius a = 7.5mm at various frequencies obtained from the Equation above. This figure shows that as frequency increases the angular divergence of the beam decreases and become more directional, but small side lobes appear.

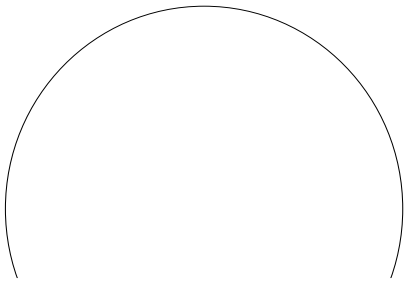

f=10kHz

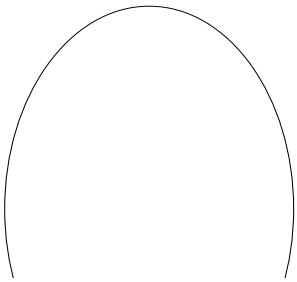

f=20kHz

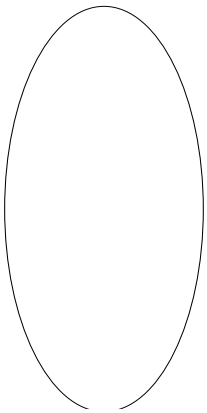

f=40kHz

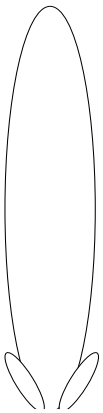

f=60kHz

Figure 3-2 Polar diagrams for the radiation from a circular disk at various frequencies

3.2.4 Attenuation of airborne ultrasound

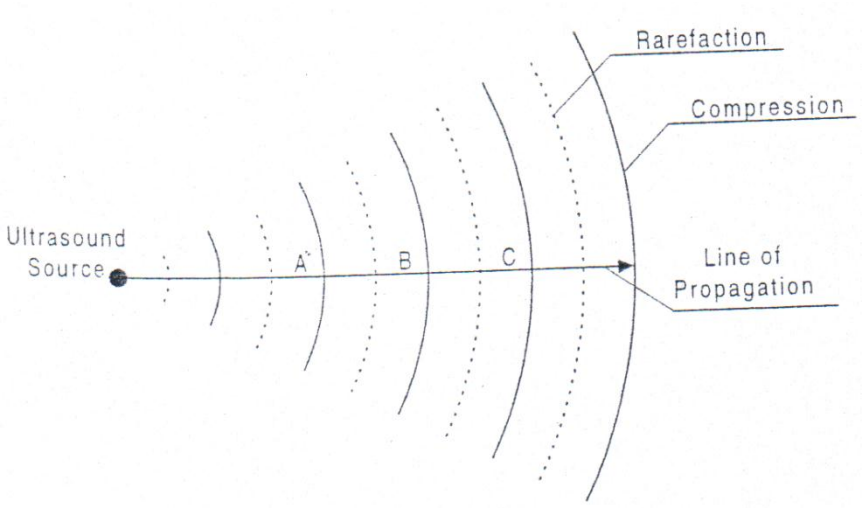

Figure 3-3 Propagation of airborne ultrasound

When an ultrasound wave propagates through air, its intensity reduces as the distance from the source increases. As shown in figure 3.3, as the wave front moves radially outwards from the source, the sound energy spreads over a larger and larger area, which may be considered the surface area of a sphere. As the surface area of the sphere becomes progressively larger the intensity per square metre, *I*, of the wave reduces according to the inverse square law, which can be expressed as:

$$I_i = I_r(\frac{d_r}{d_i})^2 \qquad 3\text{-}7$$

Where I_i is the intensity at the distance of interest, d_i, from the source, and I_r is the intensity at a reference distance d_r from the source (usually 1 m). Note that for every doubling of distance from the source the intensity falls by a factor of 4, the intensity decreases by 6dB.

In addition to the distance factor, attenuation of the airborne ultrasound will also be caused by a number of other factors of which the following are the most important:

- reflection, refraction and diffraction caused by the water vapour and dust, and
- absorption, in which acoustic energy is converted into heat by internal friction of the air.

Assuming that there are no reflecting surfaces present a semi-empiric equation is often used to combine the above two factors into an attenuation coefficient, α, which is defined by the following equation:

$$I_{r2} = I_{r1} \exp(-2\alpha(r_2 - r_1)) \qquad r_2 > r_1 \tag{3-8}$$

Where, I_{r2} the ultrasonic intensity at a distance r_2 from the source, and I_{r1} the ultrasonic intensity at a distance r_1 from the source. To express the attenuation coefficient in Nepers (Np), the following equation is given as:

$$\alpha r = \log(\frac{p_o}{p_r}) Np \tag{3-9}$$

From the table of attenuation coefficients given in [36], the attenuation coefficient of air, α, is $(1.85\times10^{-11})v^2$ $Np.m^{-1}.s^2$, where v denotes the ultrasound frequency. For instance, assuming v = 40 kHz, the corresponding attenuation coefficient α is $2.96\times10^{-2} Np.m^{-1}$, equivalent to 0.257 dB m^{-1}.

Thus, in the above conditions, a wave travelling from 1m to 2m away from a source will experience a 6dB drop in intensity but only a 0.257dB due to attenuation in the air. A wave travelling from 100m to 101m will experience a drop of 0.086dB due to spherical spread and 0.257dB due to air attenuation.

This section has described the two major reasons why the intensity of an acoustic wave decreases with distance from the source; spherical spread of the wave front and energy dissipation due to viscous and other losses during propagation. Equations (3-7) and (3-9) allow evaluation of the attenuation.

3.3 Ultrasound transducers

Many different ultrasound transducers exist, including piezoelectric, magnetostrictive, mechanical, thermal and optical. Today, piezoelectric transducers are the most widely transducers for the generation of airborne ultrasound generation and detection [37,38, 39,40,41]. The active element at the heart of the transducer is a slice of polarized material that can convert electrical energy to acoustic energy. Electrodes are attached to two of its opposite faces and, when an alternating voltage is applied across the material, polarized molecules within the material align themselves with the electric field causing the material to change dimensions. The surface thus acts as an acoustic piston generating an ultrasonic acoustic wave at the same frequency as the applied electric voltage. The transducer can also act as an ultrasound receiver. A permanently polarized material such as quartz will produce an electric field when the material changes dimensions as a result of an incident acoustic wave, which can be picked up by the attached electrodes.

In the ultrasonic applications, using pulse-echo techniques, piezoelectric ultrasound transducers transmit short ultrasound bursts that have the waveform shown in Figure 3.4.

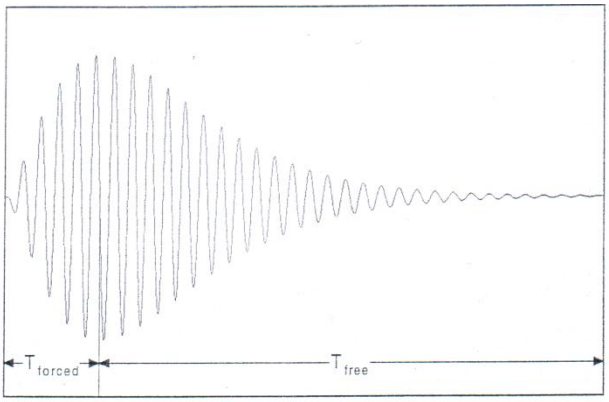

Figure 3-4 Waveform of ultrasound burst

The waveform of the ultrasound burst can be divided into two periods. In the first, T_{forced}, the ultrasound wave is generated by forced vibrations of the piezoelectric plate, and it has the same frequency as the driving signal. The amplitude of the wave in this period is due

to the inertia of the piezoelectric plate. In the second period denoted as T_{free}. The waveform is due to the free vibrations of the piezoelectric plate after the driving signal has disappeared. Here the frequency (f_{free}) of the vibration is determined by the mass (M) of the vibrating object and its compliance, (C_m), the displacement per unit restoring force of the vibrating system, according to the following expression:

$$f_{free} = \frac{1}{2\pi}(MC_m)^{-\frac{1}{2}} \qquad 3\text{-}10$$

f_{free} is the resonant frequency of the vibrating system. In practice, frictional effects cause the motion to be damped, and provided that this damping is below critical, oscillation still occurs but the amplitude decreases with time (see Figure 3.4). The mathematical expression for this free vibration is:

$$x = x_0 \exp(-\alpha' t)\cos 2\pi f_{free} t \qquad 3\text{-}11$$

Where $\alpha' = R_m / 2M$, and R_m is the mechanical resistance. Here, x is the amplitude of the vibration and x_0 is the initial amplitude.

The free and forced vibrations of the transducer do not necessarily have the same frequency. However, to drive the transducer more efficiently, the driving signal is normally at the resonant frequency of the transducer. Thus, the following expression can be used to model the ultrasound burst shown in Figure 3.4 [42]:

$$x(t) = x_0 t^{lIL} \exp(-\alpha' t)\cos(2\pi f_{free} t + \varphi) \qquad 3\text{-}12$$

Where, the coefficient m ranges from 1 to 3 for a good approximation and φ is a phase shift.

3.4 Transmitted ultrasonic signals

Generally used ultrasonic signals are categorized as pulse or continuous type wave. A pulse is a short-duration signal and emitted discontinuously. It is often called a gated-

wave. A gated-wave can be very beneficial for a transceiver which acts as both a transmitter and receiver. In contrast, a continuous wave is transmitted without any interruption. Thus, the receiver can only be used to acquire the signal. This characteristic is very useful in phase detection which compares the phase difference between outgoing and incoming signals.

3.4.1 Pulses

Pulse-echo ranging systems are widely used because only one sensor is required to transmit and receive the signal. The pulse is a frequency broadband signal. The shorter the duration, the broader the bandwidth. Although a shorter duration can produce a wider bandwidth, it often suffers from a reduced energy, which impedes TOF estimation. A compromise is to emit several periods of a sinusoidal wave to provide enough signal strength. Figure 3.5, shows one-cycle and four-cycle pulses and the corresponding spectra. The four-cycle pulse yields narrower frequency band but a higher level of power. In contrast, the one-cycle pulse results in broader frequency band but a lower level of power [43].

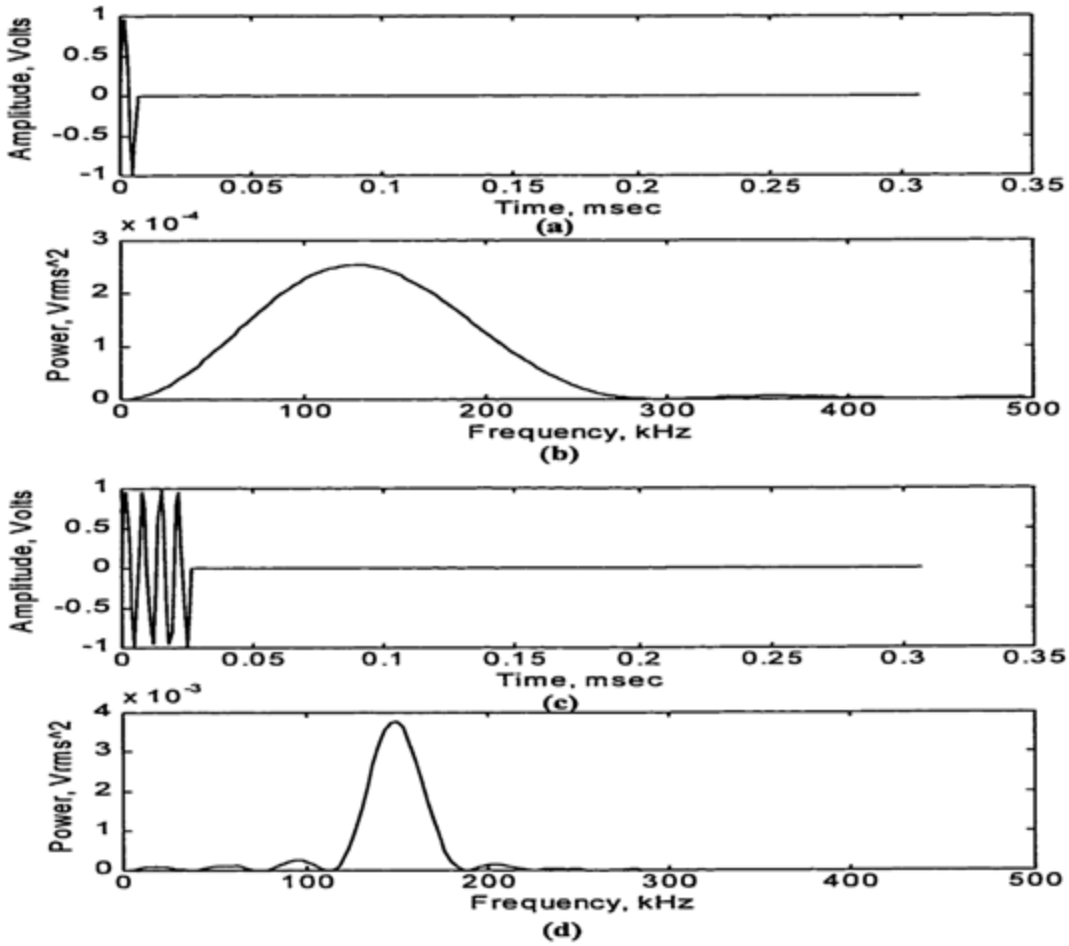

Figure 3-5 The gated sine waves and the associated spectra

(a) A one-cycle sinusoidal pulse in the time domain

(b) The spectrum of the one-cycle pulse

(c) A multiple-cycle sinusoidal pulse in the time domain

(d) The spectrum of the multiple-cycle pulse

3.4.2 Modulated signals

Many modulation methods are available for ultrasonic ranging such a frequency modulation, amplitude modulation, and phase shift keying [33]. The major advantage of the modulated signal is to reduce the noise effect during the propagation. Thus, these methods are often applied in the communication systems for recovery of noisy signals. In

addition to improving the signal to noise ratio, the modulation process usually broadens the signal bandwidth and shifts the major signal spectrum to close to the carrier frequency. The broader bandwidth can be advantageous for certain detection algorithms that require wide-band signals; whereas, the frequency shift is often used to match the signal with the sensor's effective bandwidth. This yields the most efficient transmission sensitivity and minimizes the distortion. A special category of the modulated signal that contains a linearly varied frequency is known as a chirp, or FM sweep (Figure 3.6). A typical linear chirp signal can be written as

$$f(t) = \sin\left[2\pi\left(f_0 + \frac{f_1 - f_0}{2t_s}t\right)t\right] \qquad 3\text{-}13$$

Where f_0 and f_1 are the start and stop frequencies, respectively, and t_s is the sweep duration. Equation (3-13) describes a sinusoidal signal with frequency varying from f_0 to f_1 during t_s. After t_s, the signal repeats itself. Because of its broadband characteristic, one can utilize a deconvolution technique, or the estimation of the impulse response function, to determine the time of flight. Alternatively, a cross correlation function can be used to determine the TOF [11, 61].

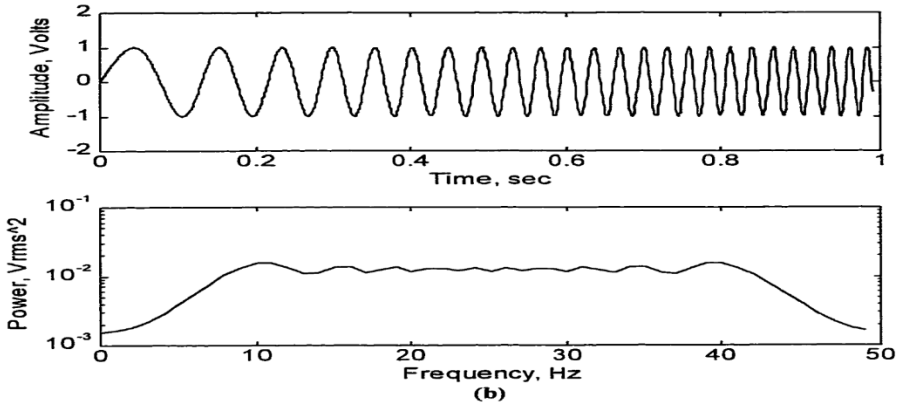

Figure 3-6 A linear frequency sweep chirp and its spectrum

(a) The signal in the time domain

(b) The power spectrum of the chirp

3.4.3 Pseudorandom code

Pseudorandom code (PN code) is a special sequence which acts like noise. Its autocorrelation function demonstrates a similar property to white noise, which has no correlation to itself except at $\tau=0$. Figure 3.7 shows a typical l5-bit PN sequence and its auto-correlation function. The peak in the autocorrelation function occurs at $\tau=0$ and its value is equal to one; while sidelobes are equal to -1/N. The width of peak is equal to one bit length in time. Thus, the shorter the chip duration, the narrower the peak.

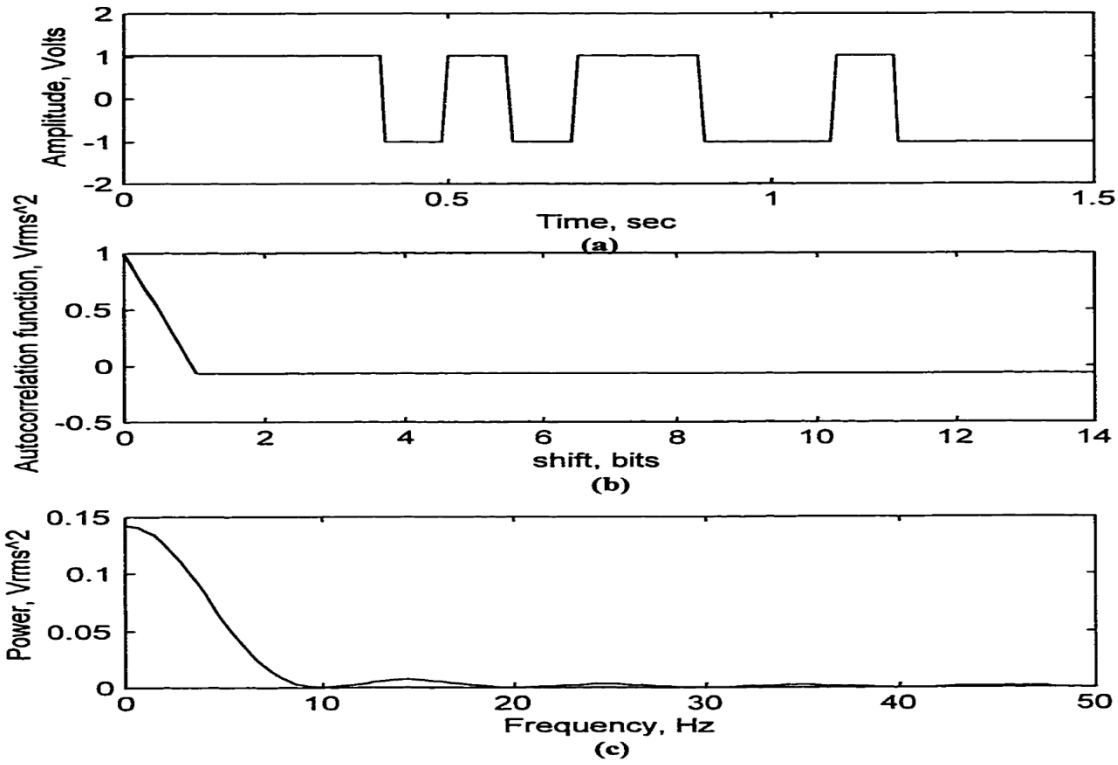

Figure 3-7 An example of a PN code

(a) A 15-bit PN code in the time domain

(b) The autocorrelation of the PN code

(c) The power spectrum of the PN code

Because of its noise-like characteristic, PN code has a broad spectrum. Its bandwidth is decided by the bit rate (number of bits transmitted per second). For example, a 15-bit sequence transmitted in 1.5 sec results in a 20 Hz mainlobe bandwidth (null to null),

(Figure 3.7c). Note that a simple PN code is a base-band signal that starts to spread its spectrum from zero Hz [43].

3.5 Modern applications of ultrasonics

Since the first application of ultrasonics in 1883, when Galton devised a high frequency whistle to measure the upper frequency limit of response of the human ear, ultrasonics has been widely applied in industry, research and medical practice, etc. In this section, some applications of ultrasonics will be introduced briefly.

3.5.1 Ultrasound flaw detection

The Pulse-Echo method can be applied for flaw detection. Assuming that a longitudinal wave probe is mounted on one of the two parallel surfaces of a specimen, it transmits an ultrasound burst through the specimen and receivers an echo that is reflected by the other surface, named as the *bottom echo*. If there is a flaw in the specimen, an extra echo will be received before the bottom echo, thus indicating the presence of the flaw. Here, the time delay of the extra echo determines the depth of the flaw, and the amplitude indicates the extent of the defect. Improvements on this method were made by employing variable-angle transducers that do not necessarily have to be parallel to the surface to detect flaws.

3.5.2 The ultrasonic flowmeter

The ultrasonic flowmeter operates on the Doppler principle. Two reversible transducers are placed in the liquid along the line of flow, one acting as transmitter and the other as receiver of ultrasonic pulses. At short regular intervals, they are switched over so that the transmitter becomes a receiver and the receiver acts as a transmitter. The acoustic velocities are $c + u$ along the direction of flow and $c - u$ in the receiver direction, where c represents the local velocity of sound without flow, and u the velocity of the streamline flow of liquid. Peaks, corresponding to these velocities appear on the screen of an oscilloscope and, because the frequency of switching over the transducers is high, the two

peaks are observed almost simultaneously. The distance between the peaks gives a direct indication of the velocity of flow of the liquid.

3.5.3 Underwater application

Marine applications of ultrasonics date back to the first World War, 1914-18, when they were used for locating submarines. Considerable advances have been made since in this field and pulsed ultrasonic waves are now commonly used for sounding ocean beds. With an ultrasonic pen recorder, one can chart the ocean bed using the reflected pulses. It is also possible to locate shoals of fish by this method, and it has been claimed that a given fish species can be indentified from the characteristics of the recorded traces. Because of the long path lengths in seawater, frequencies in the lower kilocycle range must be used to avoid too high an attenuation. Signalling is another underwater application of ultrasonics. With ultrasonic waves as a carrier, modulation devices enable the transmission of speech between ships.

3.5.4 Medical applications

The techniques used for flaw detection have been extended with a considerable degree of success to medical diagnosis. The characteristic impedance and absorption coefficients of different parts of the human body, such as fat layers, muscle, bone, etc., are sufficiently different to render these methods highly successful. It has also been found that the acoustic properties of healthy and malignant tissue differ to such an extent that an early diagnosis of cancer is sometimes possible. The uses of miniature transducers have made possible ophthalmic and dental examinations by ultrasonics. Care must be taken to ensure that the acoustic powers used are not so high as to cause damage to the body either by heating or by cavitation.

Frequencies in the lower megacycle range are commonly used, and coupling is normally achieved by the immersion technique. One method is to use water contained in a vessel

having a rubber bottom, which can be placed in contact with the skin. Scanning is achieved by moving the transducer inside the vessel.

One of the most important modern applications of ultrasonics for medical diagnoses is the 'B-scan' technique of flaw detection, for which the position of the transducer is indicated on a vertical axis and the echo distance on the horizontal axis. The intensity of the sound reflected from a discontinuity modulates the intensity of the scanning electron beam and a 'picture' of the examined part of the body is thus obtained. The results obtained during the whole period of the scan can be automatically recorded and stored on a laptop. This technique has been applied successfully for the location of brain tumours and for the foetal examination of expectant mothers.

Examinations of the heart have been conducted by means of a Doppler technique. Ultrasonic waves are directed towards the heart and reflected back again. The velocity of the walls of the heart is determined by the observed change in frequency. Any irregularities from normal functioning can readily be detected. The ultrasonic flowmeter discussed earlier has also been used successfully for the measurement of the rate of flow of blood through the human body.

3.5.5 Applications of airborne ultrasonics

At present, there are not many applications of airborne ultrasonics, and these applications are restricted to the lower kilocycle range, where attenuation is not too great. One successful commercial application of airborne ultrasound is an intruder alarm system for the detection of burglars and fire in enclosed premises. A magnetostrictive transducer is placed at some point in a room and the pulses are propagated in all directions. These are reflected by the walls and furniture and eventually picked up by a receiver, from which a constant indication is obtained. Any variation in the sound field, caused by an intruder or increase in temperature, gives rise to a change in this indication, which sets off an alarm.

Another application of airborne ultrasonics is a system for the guidance of blind people. A small portable device contains two electrostatic dielectric transducers. One, acting as transmitter. is excited by a periodic modulated frequency, sweeping from 30 kHz to 60 kHz. Ultrasonic waves produced in this way are reflected from obstacles, detected by the other transducer, and then converted to audible signals. Such a device, the Palmsonar PS231, is available from the Royal National for the Blind and can be used to detect an obstacle up to 4m away.

Applications of airborne ultrasonics are also found in industry. Mahajan [44] Presented an ultrasonic seam tracking system developed for robotic welding which tracks a seam that curves freely on a two-dimensional surface. The seam is detected by scanning the area ahead of the torch and monitoring the amplitude of the waves received after reflection from the work piece surface. This seam tracking system is capable of detecting seams less than 0.5mm wide and 0.5mm deep.

3.5 Summary

Ultrasonics is the study and application of sound waves having frequencies higher than those to which the human ear can respond (about 20kHz), and therefore it covers all the works that has been done in this project. In this chapter some related topics of ultrasonics have been briefly introduced.

This chapter has introduced some basic considerations of ultrasound, including velocity, reflection, refraction and attenuation. The information given here will be used in Chapter 5, where ultrasound models are developed. The working principles of the piezoelectric transducers that are used in the ultrasonic 3D measurement system and transmitted ultrasonic signals have been briefly introduced. At the end of this chapter, some of the countless ultrasonic applications are mentioned, to provide a general view of the developments in modern ultrasonics.

In the next chapter, previous work on the ultrasonic 3D measurement systems is presented in detail.

Chapter 4 Previous work on ultrasonic 3D measurement systems

4.1 Introduction

As mentioned in the last chapter, the characteristics of ultrasound, such as the velocity and attenuation, are determined by the medium through which ultrasound propagates. Therefore, airborne ultrasonics, with its unstable medium of air, is rarely used for high accuracy measurement.

In the previous ultrasonic 3D measurement systems, TOF (Time-of-Flight) technique was applied to determine the distances between the position and the surrounding receivers [4, 6]. The results were then used to evaluate the 3D coordinates of the position. These systems have been tested on different applications.

In this chapter, the working principle of the previous ultrasonic 3D measurement systems will be introduced in detail, followed by a discussion on the 3D measurement systems limitations. First, in the following section, the algorithm used for position coordinate in the previous 3D measurement systems will be introduced.

4.2 Configuration of the previous ultrasonic 3D measurement systems

The development of the previous ultrasonic 3D measurement system started in the middle of the 1980s by Dickinson [31]. During the development period, in 2002, Mahajan [5] helped in building the hardware of the 3D measurement system.

Figure 4.1, shows that the system is composed of a transmitter and six receivers located around the area of interest. The transmitter is located at an unknown position (u, v, w). The receivers are located at known positions: $R_1(x_1, y_1, z_1)$, $R_2(x_2, y_2, z_2)$, $R_3(x_3, y_3, z_3)$, $R_4(x_4, y_4, z_4)$, $R_5(x_5, y_5, z_5)$, $R_6(x_6, y_6, z_6)$ The TOF between the transmitter and any receiver is unknown, but the difference between times when the receivers sense the signals can be measured. This system is using spark transmitter which is transmit the signal in difference directions [53].

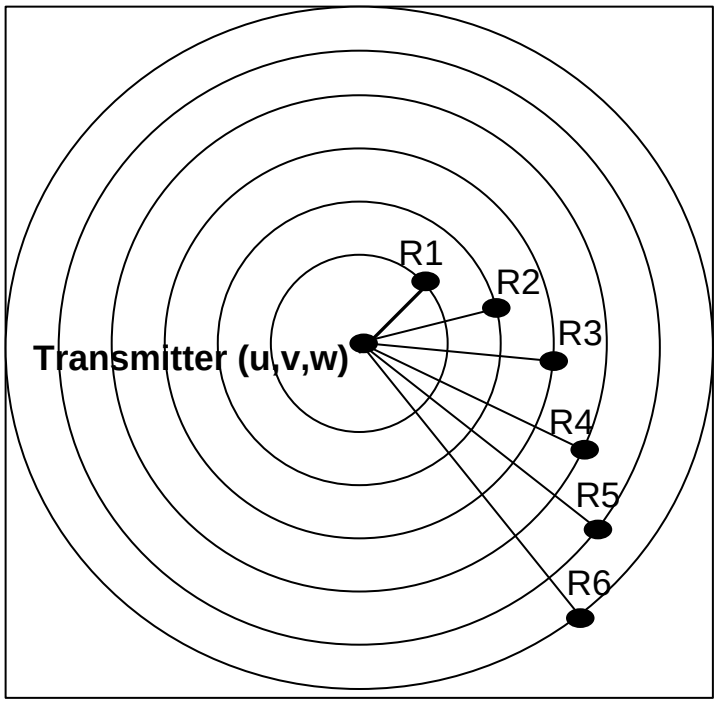

Figure 4-1 Geometric setup of the measurement system

In other words, if the transmitters send a signal at time $T=0$, the receivers will sense the signals at the unknown times T_1, T_2, T_3, T_4, T_5 and T_6. The difference between the TOFs is electronically measured as follows:

$$\Delta T_{12} = T_2 - T_1 \ , \ \Delta T_{13} = T_3 - T_1 \ , \ \Delta T_{14} = T_4 - T_1$$

$$\Delta T_{15} = T_5 - T_1 \ , \ \Delta T_{16} = T_6 - T_1 \qquad 4\text{-}1$$

This yields various known time differences that can be used in conjunction with the receiver locations to determine the point of signal origin (u, v, w). Other ΔT values, such as ΔT_{23}, could be found, and may be used to give a redundant system, i.e., more number of equations than variables. In this case, a least squares estimate may be used to estimate the values of the unknowns.

One receiver is always the first to sense the signal and this receiver (R_1) is considered to be at a distance d from the transmitter. Another receiver will be the second one to sense

the signal and this receiver is at a distance $d + c\,\Delta T_{12}$, where c is the velocity of sound. The third, fourth, fifth and sixth receivers are then at distances $d + c\,\Delta T_{13}$, $d + c\,\Delta T_{14}$, $d + c\,\Delta T_{15}$, and $d + c\,\Delta T_{16}$, respect-timely, from the transmitter. Since sound travels in circular waves form the point source (transmitter), six concentric circles can be drawn around the transmitter. The formulation for 3D position at transmitter is:

$$\begin{bmatrix} 2(x_1-x_2) & 2(y_1-y_2) & 2(z_1-z_2) & -2\Delta T_{12} & -2\Delta T_{12}^2 \\ 2(x_1-x_3) & 2(y_1-y_3) & 2(z_1-z_3) & -2\Delta T_{13} & -2\Delta T_{13}^2 \\ 2(x_1-x_4) & 2(y_1-y_4) & 2(z_1-z_4) & -2\Delta T_{14} & -2\Delta T_{14}^2 \\ 2(x_1-x_5) & 2(y_1-y_5) & 2(z_1-z_5) & -2\Delta T_{15} & -2\Delta T_{15}^2 \\ 2(x_1-x_6) & 2(y_1-y_6) & 2(z_1-z_6) & -2\Delta T_{16} & -2\Delta T_{16}^2 \end{bmatrix} * \begin{bmatrix} u \\ v \\ w \\ cd \\ c^2 \end{bmatrix}$$

$$= \begin{bmatrix} x_1^2+y_1^2+z_1^2-x_2^2-y_2^2-z_2^2 \\ x_1^2+y_1^2+z_1^2-x_3^2-y_3^2-z_3^2 \\ x_1^2+y_1^2+z_1^2-x_4^2-y_4^2-z_4^2 \\ x_1^2+y_1^2+z_1^2-x_5^2-y_5^2-z_5^2 \\ x_1^2+y_1^2+z_1^2-x_6^2-y_6^2-z_6^2 \end{bmatrix} \qquad 4\text{-}2$$

This is final formulation for estimating the 3D position of the transmitter using the differences in the measured TOFs as estimating the speed of sound at every ranging operation.

This system was tested in a workspace of 1000 × 1000 mm, the absolute error 2mm for distance less than 700 mm.

In 2002, Martin [6] builds the hardware of another 3D measurement system. The performance of this system was demonstrated experimentally on a robot.

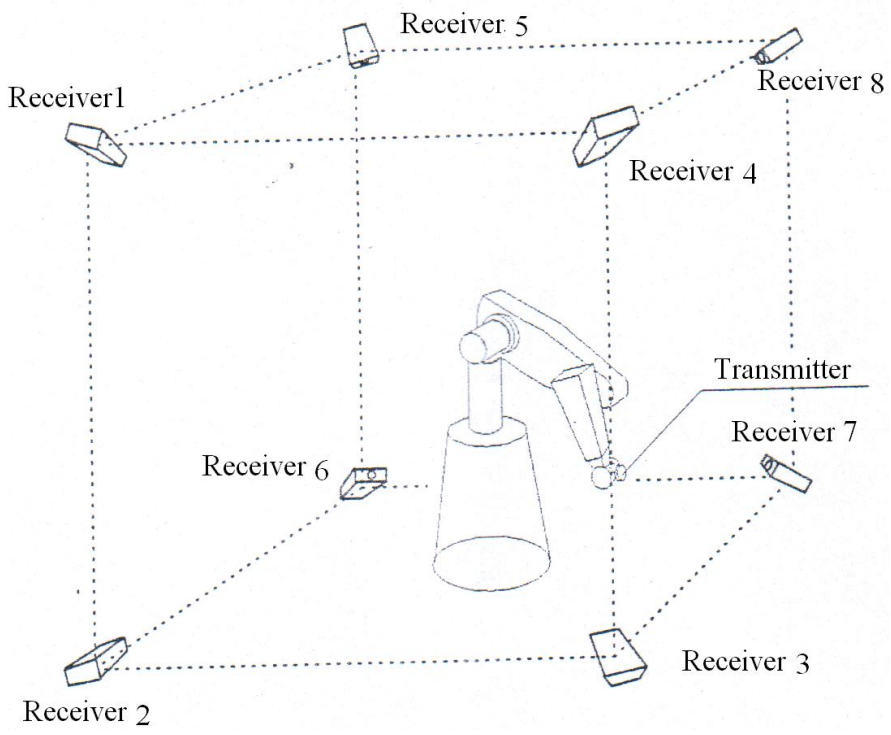

Figure 4-2 Geometric setup of the measurement system

As shown in the above figure, eight receivers are arranged at the corners of a virtual cube, facing towards the centre of the cube. This ensures that, in any situation, at least three receivers can work properly, and therefore enable the tracking system to continuously provide information on the transmitter position.

Once the distance between the transmitter and the receivers are measured, the data from each receiver is sent to the computer to calculate the 3D position of the transmitter. Among these 8 receivers, any combination of three adjacent receivers composes a coordinate frame, in which the 3D coordinate position of the transmitter can be calculated.

As mentioned above, the determination of the position of the transmitter is based on the measurements of distance between the transmitter and the receivers. Therefore, the

accuracy and the resolution of the whole tracking system depend on the accuracy and the resolution of the individual measurements of distance by each of the receivers.

In this 3D measurement system, the TOF (Time-Of-Flight) is selected for distance measurement, which is achieved by recording the travelling time, t of the ultrasound flying from the transmitter to the receiver. The following equation shows how the distance is calculated from the recorded time of flight.

$$d = c.t \tag{4-3}$$

Here, d denotes the distance between the transmitter and the receiver, and c is the speed of the ultrasound, which is normally regarded as a predetermined constant. The distances between transmitter and each receiver determined as this equation:

$$\begin{aligned} d_1^2 &= x^2 + y^2 + z^2 \\ d_2^2 &= (x - x_2)^2 + y^2 + z^2 \\ d_3^2 &= (x - x_3) + y^2 + (z - z_3)^2 \end{aligned} \tag{4-4}$$

The performance of this system has been verified experimentally by building a prototype consisting of a set of eight ultrasonic receivers placed in a metallic frame, while the moving element (a spark transmitter) is mounted on top of a robotic arm. The prototype showed a maximum error of 1 mm within a work area of 3×3×3m.

The previous ultrasonic 3D measurement systems have same problem as other TOF systems' poor accuracy. Therefore, to achieve a high-resolution distance measurement, a new technique other then the TOF is needed. One suitable alternative technique is the multiple-frequency continuous wave frequency modulation system [45, 46, 47] developed in this project, which will be introduced in the following chapter. In spite of the low resolution, the previously developed ultrasonic 3D measurement system also has other limitations, such as the insufficient accuracy and flexibility [7]. Therefore, in order to overcome these drawbacks and construct a better and more practical 3D measurement system, new techniques and algorithms were introduced in the development of the new

3D measurement system, which will be detailed in the following chapters. Next in this chapter, the limitations of the previous 3D measurement systems will be studied in more detail.

4.3 Limitations of the previous ultrasonic 3D systems

4.3.1 Limitations on the arrangement of the receivers

As mentioned in section 4.2, in order to overcome the obstacle problems, 6 receivers are arranged in figure 4.1 and 8 receivers are arranged in figure 4.2. However, in practice, it is very difficult or even impossible to place the receivers at the desired position precisely and therefore errors in the placement of the receivers introduced significant errors into the position calculations. Furthermore, it takes a long time to set up a system, even if it is possible to actually place the receivers at the right positions. This arrangement still has problem of poor adaptability and flexibility. In industry, the working environment is rather complicated, and there may be no room for the receivers to be placed in such a way. Even if there is available space for the receivers, large obstacles in the workspace may totally block the transmission path. In addition, due to changes of the working environment, it may be necessary to change the arrangement of the receivers from time to time. Therefore, a new geometric algorithm, with which the receivers can be placed at any convenient places, is required for 3D positioning. Such a new algorithm has been developed and will be discussed in detail in the next chapter. Moreover, another algorithm was also developed to locate the receivers, so the set-up procedure of the new 3D system is much simplified. These two new algorithms together improved the flexibility and adaptability of the system considerably.

4.3.2 Limitation in the measurement accuracy

As shown in section 4.2, the accuracy of the previous 3D measurement systems is between ± 2.5mm to ± 1mm, which is far from the required accuracy of ±100μm. the

errors may be caused by either errors in the predetermined ultrasonic speed or inaccurate detections of the ultrasound bursts, or both.

The low amplitude and poor S/N ratio of the first few cycles of the received ultrasound burst makes the starting point difficult to detect with good accuracy. Therefore, with TOF method used in previous 3D measurement system, a random time delay is normally added to the measured time of flight and high sensitivity to changing in temperature and humidity caused to increase the error in time delay. Overcoming this drawback, the new methods avoided the detection of the starting point with some digital processing techniques. Though these new techniques demonstrated considerable improvements in their accuracy, one should notice that they are aimed for static distance measurement with a stationary transmitter/ target, which is obviously not the case in 3D measurement system. Therefore, in the new ultrasonic 3D measurement system, both multi-frequency continuous wave (MFCW) and frequency modulation (FM) are employed for static and dynamic distance measurement, and result in sub-micrometer accuracy.

The estimation of the ultrasound speed is another difficult task in ultrasonic distance measurement. As introduced in Chapter 3, the velocity of ultrasound is determined by the characteristics of the medium, mainly the temperature in the case of airborne ultrasound. As the air temperature changes frequently and randomly, even a well-calibrated ultrasound velocity is not sufficient for accurate measurement. Therefore, during the development of the new 3D measurement system, a novel algorithm was developed to adapt the ultrasound speed drifting, while measuring the position. This technique will be introduced in chapter 5 for ultrasound speed evaluation.

4.4 Summary

This chapter has reviewed previous work on ultrasonic 3D measurement systems, whose working principles were introduced in terms of the systems configuration and the TOF technique used for distance measurement. The limitations of these measurement systems were also addressed in the preceding section.

In order to simplify the algorithm and speed up the calculation for position coordinate, the measuring system restricts the receivers to be orthogonally placed. This brings about considerable practical difficulties in receiver positioning, especially when more (8) receivers are used. The systems also employed TOF technique for distance measurement, which lacks in measurement accuracy. Though the research improves the accuracy of TOF distance measurement significantly, their resolution limitation is inherent and cannot be overcome with TOF. Thus, another technique, in this case the (MFCWFM) technique is introduced to the new 3D measurement system and will be discussed later.

In the coming chapters, the new ultrasonic 3D measurement system developed in this project will be introduced in terms of its working principles, hardware/software implementations and experimental results.

Chapter 5 Enhanced 3D measurement system

5.1 Introduction

In order to overcome the drawbacks and limitations of previous ultrasonic 3D measurement systems, new techniques and algorithms were developed and introduced into a new 3D measurement system to achieve improvements in measurement accuracy and system adaptability.

In this chapter, the working principle of this enhanced ultrasonic 3D measurement system is introduced, using the Data Flow Diagram (DFD), to model the details of the system in term of its functionality.

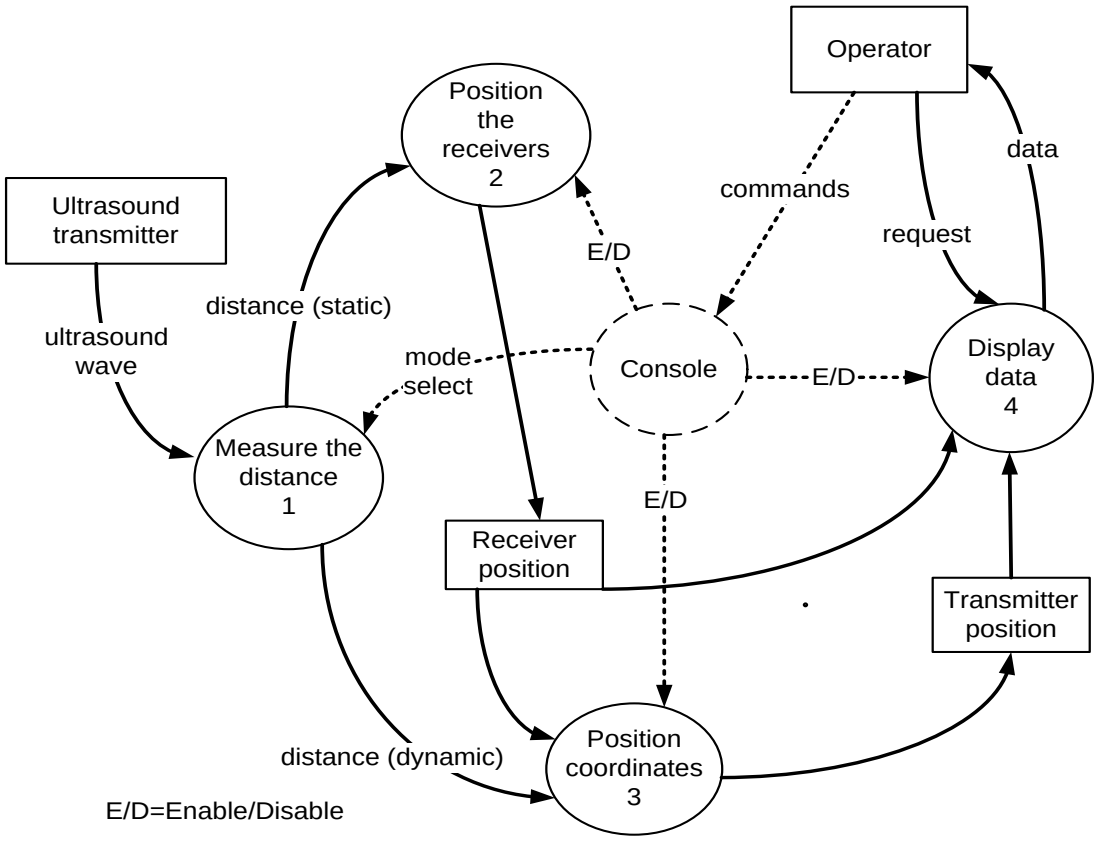

Figure 5-1 Top level DFD of the new ultrasonic 3D measurement system

Figure 5.1 above shows the top level DFD of the new ultrasonic 3D measurement system. It contains four data transformations (circles), one control process (dashed circle) and two data stores (two parallel lines). The ultrasound signal is received at transformation 1, *'Measure the distance'*, where the distances are measured by the MFCWFM technique (see Section 5.2) in the system setup stagte, controlled by the control process, *'Console'*. The static distances between the transmitter and the receivers are measured sequentially, one by one, by combined MFCW and FM (see Section 5.2.1) and sent to transformation 2, *'Position the receiver'*, to determine the receiver's position. During the measuring, the 3D positions coordinate of the transmitter are determined at transformation 3, *'Position coordinate'*, with the dynamic distances measured at transformation 1 and receiver position from *'Receiver position'*. The positions and the transmitter data is stored at the data stores, *'Receiver position'* and *'Transmitter position'* respectively, and can be viewed, on request, by the *'Operator'* though the transformation 4 *'Display data'*.

In this chapter, the working principles of the new 3D measurement system will be detailed in terms of the data transformations: *'Measure the distance'*, *'Position the receivers'* and *'Position coordinates'*.

5.2 Distance measurement

Just as in previous ultrasonic 3D measurement systems, establishing position coordinates requires knowledge of the distances between the transmitter and a minimum of three receivers, so at least three data transformations will be contained in transformation 1 in order to measure the distances to each receiver, as shown by the DFD in Figure 5.2.

In the figure, the transformations are selected by the control signal *'mode select'* for either static distance measurement or dynamic distance measurement. The former is used to determine the position of the receivers for system setup at transformation 2, *'Position the receivers',* and the latter is sent to transformation 3, *'Position coordinate'*, for transmitter

positioning. To improve the accuracy, the newly developed MFCWFM system replaced the previous TOF system for distance measurement.

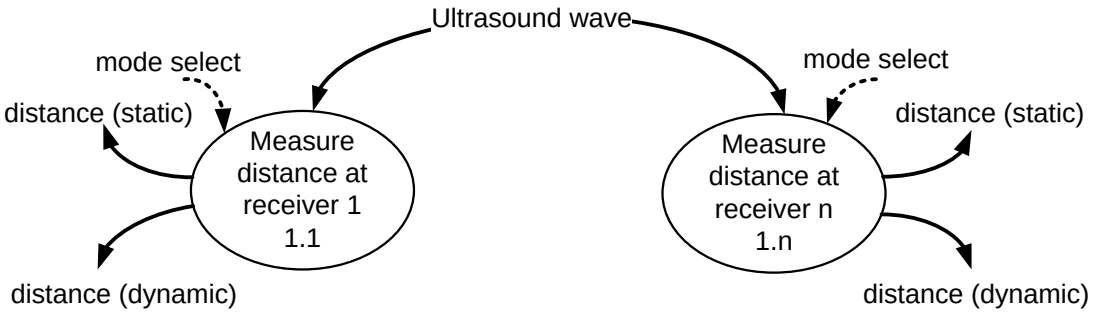

Figure 5-2 DFD of transformation 1 'Measure the distance'

Figure 5.3 shows the DFD of the new system containing the MFCWFM system for both 1D static and dynamic distance measurement. During system setup, transformation 1.1.2 *'Measure static distance'* is enabled by the control process to measure the static distances to determine the position of the receiver.

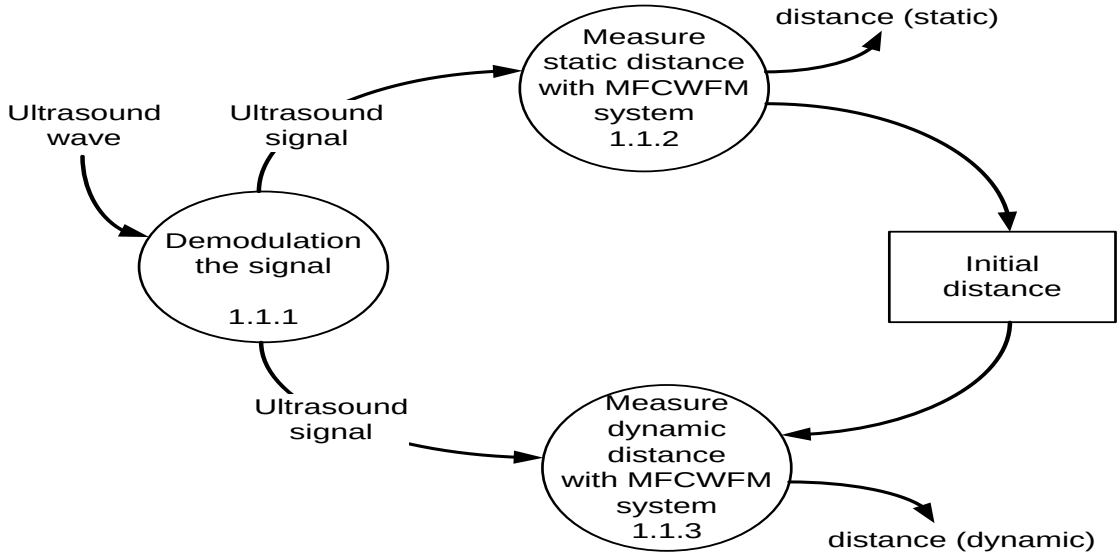

Figure 5-3 DFD of transformation 1.1 'Measure distance at receiver 1'

Initially, in the measurement procedure, the distance between the transmitter and the receiver is measured at transformation 1.1.2 and saved in the data store, '*Initial distance'*. Then transformation 1.1.3 *'Measure dynamic distance'* is implemented to measure transmitter displacement. Then, knowing the initial distances, absolute distances between the transmitter and the receivers are determined and sent to the next stage for coordinate determination. A prototype of this system has been developed and has greatly improved the accuracy of distance measurement. The working principles of the MFCWFM system are introduced in the following sections.

5.2.1 MFCWFM distance measurement

In this section, a simple yet accurate MFCWFM system developed by the author is introduced [45, 47]. Its principles and use in the 3D measurement system for both static and dynamic distance measurement are illustrated by the DFD in Figure 5.4.

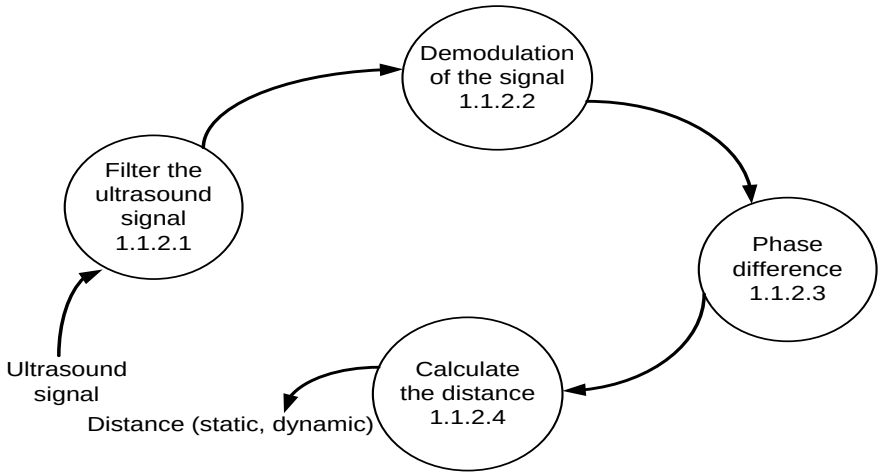

Figure 5-4 DFD of transformations 1.1.2 and 1.1.3 'Measure distance with MFCWFM'

The above diagram provides a view of the MFCWFM system from receiving the signal, with the corresponding software implementations and experimental results introduced later. As seen in Figure 5.4, the input signal is first filtered to eliminate the DC offset,

then transformation 1.1.2.2, *'Demodulation of the signal'*, demodulates and separates the frequencies. The output of the transformation 1.1.2.3, *'Phase difference'*, is the phase difference between the transmitted and received signals. Finally, this phase difference is used by transformation 1.1.2.4, *'Calculate the distance'*, to calculate the distance between transmitter and receiver.

Working principles

The distance between transmitter and receiver is determined from the measurement of the phase difference between the received and transmitted signals. If the transmitter is energized with a continuous sinusoidal signal, the signal at the receiver can be written as:

$$V(t) = A\sin(\omega t + \varphi) \qquad 5\text{-}1$$

Here A is the peak value of the received signal, ω is the angular frequency of the wave form and φ is the phase shift with respect to the wave at the transmitter and its value is proportional to the separation between source and receiver. The ranging distance d can be uniquely determined by the phase shift φ if the maximum ranging distance does not exceed the half wavelength of the lowest frequency used, otherwise a phase ambiguity will occur. The maximum achievable range with transducers transmitting a pure tone of 25 kHz (this is a frequency commonly used in air ranging applications) is about 7mm which is usually far too small for most 3D ranging requirements. Here several low frequencies are used to modulate the 25 kHz resonant frequency which then acts as the carrier, and it is the phase and phase shift of the envelop of the received signal which is measured to calculate the distance [48]. In this case two modulating frequencies are used, 1 kHz and 100 Hz, and a maximum detectable range of about 1.2m is achieved which meets most requirements for 3D measurement. Here the carrier signal and both modulation signals are considered sinusoidal with no phase shift as they are emitted by the transmitter, see Figure 5.5.

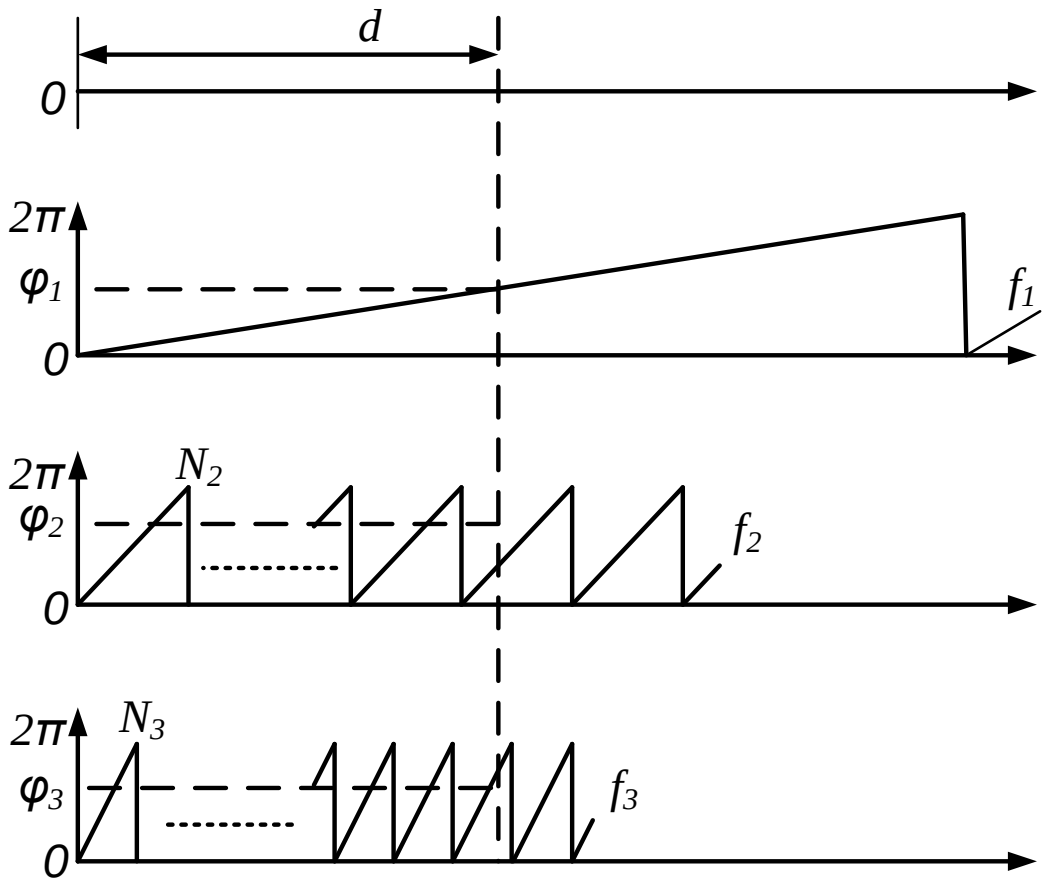

Figure 5-5 The motion distances are measured with three difference frequencies

It is assumed in Figure 5.5 that the phase change corresponding to the target range (source-receiver separation) does not exceed π for the 100 Hz signal. The phase shift φ_1 at the frequency f_1 = 100 Hz, which has the longest wavelength λ_1, as shown in Figure 5.5, gives the first estimate of the moving distance as:

$$d = d_1 = \frac{\varphi_1}{2\pi} \times \lambda_1 \qquad 5\text{-}2$$

A modulating signal with a higher frequency, f_2 = 1 kHz, is then used to measure the same range with a finer resolution. This is achieved because a small change in the source-receiver separation, the measured range, creates a greater phase shift between the transmitted and received signals than occurred with frequency f_1. For example, a phase shift of π for the 100 Hz signal corresponds to a distance of about 1.7 m, and at 1 kHz a distance of about 170 mm. Thus a more accurate approximation to the measured range is obtained from

$$d_2 = \frac{\varphi_2}{2\pi} \times \lambda_2 \qquad 5\text{-}3$$

The integer number, N_2, of the wavelength of λ_2 between transmitter and receiver can be obtained from

$$N_2 = Int[\frac{d_1}{\lambda_2}] \qquad 5\text{-}4$$

Equation (5-2) may be rewritten as:

$$d = N_2 \times \lambda_2 + \frac{\varphi_2}{2\pi} \times \lambda_2 \qquad 5\text{-}5$$

Similarly, the measured range d_3 corresponding to the phase shift φ_3 at frequency f_3 = 25kHz is given by:

$$d_3 = \frac{\varphi_3}{2\pi} \times \lambda_3 \qquad 5\text{-}6$$

The integer number N_3 of the wavelength λ_3 can be calculated from:

$$N_3 = Int[\frac{d_2}{\lambda_3}] \qquad 5\text{-}7$$

$$d = N_3 x \lambda_3 + \frac{\varphi_3}{2\pi} \times \lambda_3$$

The estimation of the measured displacement distance using three frequencies can be expressed by the following equation:

$$d = Int[\frac{\varphi_1(t)}{2\pi} \times \frac{\lambda_1}{\lambda_2}] \times \lambda_2 + Int[\frac{\varphi_2(t)}{2\pi} \times \frac{\lambda_2}{\lambda_3}] \times \lambda_3 + \frac{\varphi_3(t)}{2\pi} \times \lambda_3 \qquad 5\text{-}8$$

Where:

$$\lambda_1 = \frac{c}{f_1} \quad , \quad \lambda_2 = \frac{c}{f_2} \quad , \quad \lambda_3 = \frac{c}{f_3}$$

The final equation derived from the above is:

$$d = Int[\frac{\varphi_1(t)}{2\pi} \times \frac{f_2}{f_1}] \times \frac{c}{f_2} + Int[\frac{\varphi_2(t)}{2\pi} \times \frac{f_3}{f_2}] \times \frac{c}{f_3} + \frac{\varphi_3(t)}{2\pi} \times \frac{c}{f_3} \qquad 5\text{-}9$$

Where c is the local value of the speed of sound which is a function of temperature and humidity. To reduce any error in c these quantities should be evaluated for the workspace. In fact, during this research a MFCWFM technique was used to produce a new highly accurate system for humidity and temperature measurement in air [35].

5.2.2 Evaluation of temperature

The theoretical expression for the speed of sound c in an ideal gas is

$$c = \sqrt{\frac{\mu P}{\rho}} \qquad 5\text{-}10$$

Where P is the ambient air pressure, ρ the local density of the gas, and μ the ratio of major specific heats of gas and will depend upon the number of degrees of freedom of the gas molecules:

$\mu = 1.67$ for monatomic molecules

$\mu = 1.40$ for diatomic molecules

$\mu = 1.33$ for triatomic molecules.

Since air is composed primarily of diatomic molecules, the speed of sound in air is

$$c = \sqrt{\frac{1.4P}{\rho}}$$

Assuming the equation of state for air is that of an ideal gas *(PV = RT)* and expressing the density ρ as mass per unit volume, the equation may be rewritten as:

$$c = \sqrt{\frac{1.4RT}{M}} \qquad 5\text{-}11$$

Where R is the universal gas constant *(R= 8.315410 J.mol^{-1}.K^{-1})*, T the absolute temperature in degrees Kelvin *(T = t +273.14)*, and M is the mean molecular weight of gas. Equation (5-11) may be rewritten as:

$$c = 331.45\ \sqrt{1 + \frac{t}{273.14}} \qquad 5\text{-}12$$

Where t is the temperature in degrees Celsius. Thus, the speed of sound can be found if the temperature t is known. Also, the equation (5-8) can be rewritten as:

$$d = (Int[\frac{\varphi_1(t)}{2\pi} \times \frac{f_2}{f_1}] \times \frac{1}{f_2} + Int[\frac{\varphi_2(t)}{2\pi} \times \frac{f_3}{f_2}] \times \frac{1}{f_3} + \frac{\varphi_3(t)}{2\pi} \times \frac{1}{f_3}) \times 331.45\ \sqrt{1 + \frac{t}{273.14}} \qquad 5\text{-}13$$

The above equation can be used either to assist the measurement of distance or to measure temperature if the distance between transmitter and receiver is known.

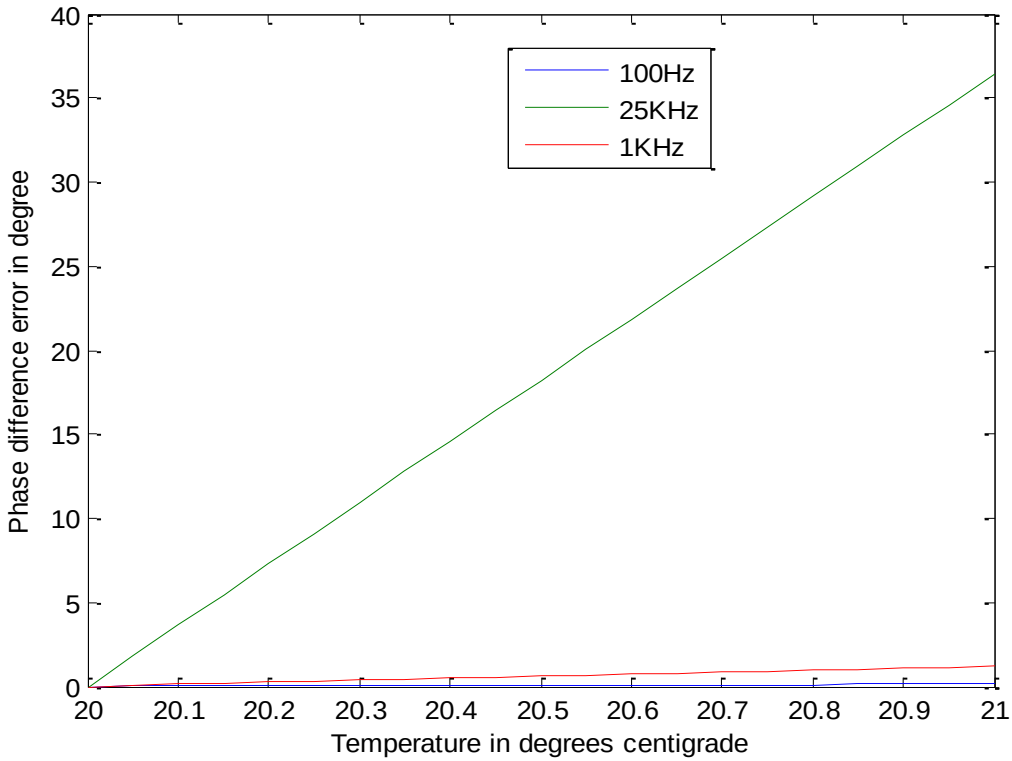

Figure 5-6 The effect of changing temperature on phase difference of the received signal

The effect of change in temperature on measured phase difference between transmitted and received signals is shown on Figure 5.6. The sensitivities of φ_1 and φ_2 to changes in temprature are very small, but the sensitivity of φ_3 is very much larger. In fact, the phase change will be proportional to the frequency of the acoustic wave. For example, for the 25 kHz wave, a change temperature from 20^0C to 20.05^0C produced a measured change in phase of 1.8^0. This system can measure a phase shift of 0.5^0, which is equivalent to a temperature change of 0.02^0C.

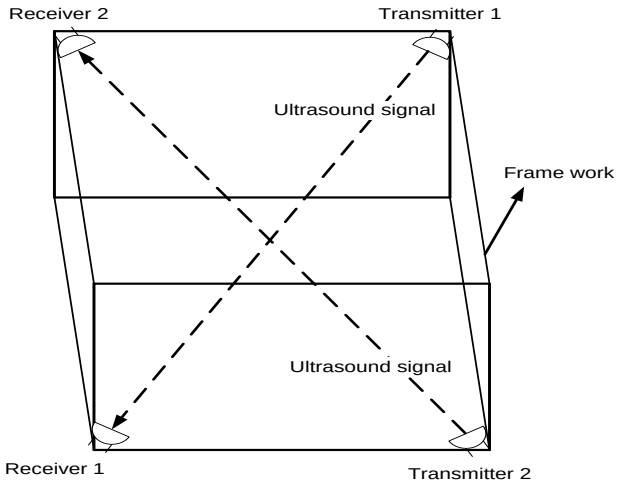

Figure 5-7 Evaluation of the temperature in a work space

Figure 5.7 is a schematic diagram showing the essentials necessary to evaluate temperature in a rectangular work space. The measurement system consists of two separate ultrasound systems [35]. The output of the first system (Receiver1 and Transmitter1) is temperature t_1 and the output of system 2 (Receiver2, Transmitter2) is t_2. Since the system is symmetrical, the temperature in the work space may be taken to be the simple average:

$$t_{ave} = \frac{t_1 + t_2}{2} \qquad 5\text{-}14$$

t_1 and t_2 are obtained from Equation (5.13).

The measurement of temperature can be made an integral part of the measurement system so that it is continually monitored and the error produced by changes in temperature is largely eliminated. In practice, the new design has improved the accuracy in the experiment to ±20μm in a range of 1100 mm.

5.2.3 Evaluation of humidity

Equation (5-11) does not include the effects of the actual specific heat ratio of the different types of molecules in the air nor the moisture in the air on the speed of sound.

The specific heat ratio μ can be expressed more exactly by letting d_f equal the number of excited degrees of freedom for the air molecules. For dry air this gives [49]:

$$\mu = (d_f + 2)/d_f \qquad 5\text{-}15$$

Because the composition of dry air is mostly diatomic molecules, $d_f = 5$ and $\mu = 1.4$.

However, air usually contains a proportion of water vapour, with $d_{fw} = 6$, so the presence of water causes the average number of degrees of freedom per molecule to increase. If h is the fraction of air molecules that are water, the average number of degrees of freedom per molecule changes and Equation (5-15) must be rewritten to include the effects of moisture in the air:

$$\mu_w = \frac{5(1-h)+6h+2}{5(1-h)+6h}$$

$$\mu_w = \frac{7+h}{5+h} \qquad 5\text{-}16$$

Thus, if the water vapour comprised 1% of the air, μ would still be 1.4 to an accuracy of 0.05%, and if water vapour comprised 10% air the value of μ would be 1.399.

The average molecular weight of air decreases with added moisture. To see this, M is calculated first for dry air. Dry air composition is

78% nitrogen with molecular weight = 28.

21% oxygen with molecular weight = 32, and

1% argon with molecular weight = 40.

Thus the molecular weight for the mixture is equal to

$$(0.78)\ (28) + (0.21)\ (32) + (0.01)\ (40) = 29$$

The presence of water with a molecular weight of 18 decreases the average molecular weight to $(29(1 - h) + 18h)$, or

$$M_w = 29 - 11h \qquad 5\text{-}17$$

Equations (5-16) and (5-17) modify the terms, 1.4 and *M*, in Equation (5-11) since both are a function of the water molecule fraction *h*.

h can be expressed in terms of the Relative humidity (*RH*, expressed as a percentage) as:

$$h = \frac{0.01RH.e(t)}{p} \qquad 5\text{-}18$$

Where *p* is ambient pressure (1.013×10^5Pa at 1 standard atmosphere) and *e(t)* is the vapor pressure of water at temperature *t*. For temperature in degrees Celsius.

$$e(t) = 669.08\, e^{0.0609\, t} \qquad 5\text{-}19$$

Equation (5-8) may now be rewritten as:

$$d = (Int[\frac{\varphi_1(t)}{2\pi} \times \frac{f_2}{f_1}] \times \frac{1}{f_2} + Int[\frac{\varphi_2(t)}{2\pi} \times \frac{f_3}{f_2}] \times \frac{1}{f_3} + \frac{\varphi_3(t)}{2\pi} \times \frac{1}{f_3}) \times \sqrt{\frac{\mu_w\, R(t + 273.14)}{\mathrm{M_w}}} \qquad 5\text{-}20$$

By knowing the temperature and distance between transmitter and receiver, the relative humidity can be determined. The method for evaluating temperature in the work volume (Figure 5.7) can also be used to evaluate the humidity in the work space. The effect of changing humidity on measured phase difference between transmitted and received signals is shown on Figure 5.8. The sensitivity of low frequency acoustic waves to changes in humidity is not strong, so the changes in φ_1 and φ_2 due to changes in humidity are very small. However, as the frequency increases into the kHz region the sensity rapidly increases. Thus the sensitivity of φ_3 to changes in humidity is much larger and, for

example, a change humidity from 75% to 78% produced a measured change in phase of 1.82^0, equivalent to a temperature change of 0.05^o.

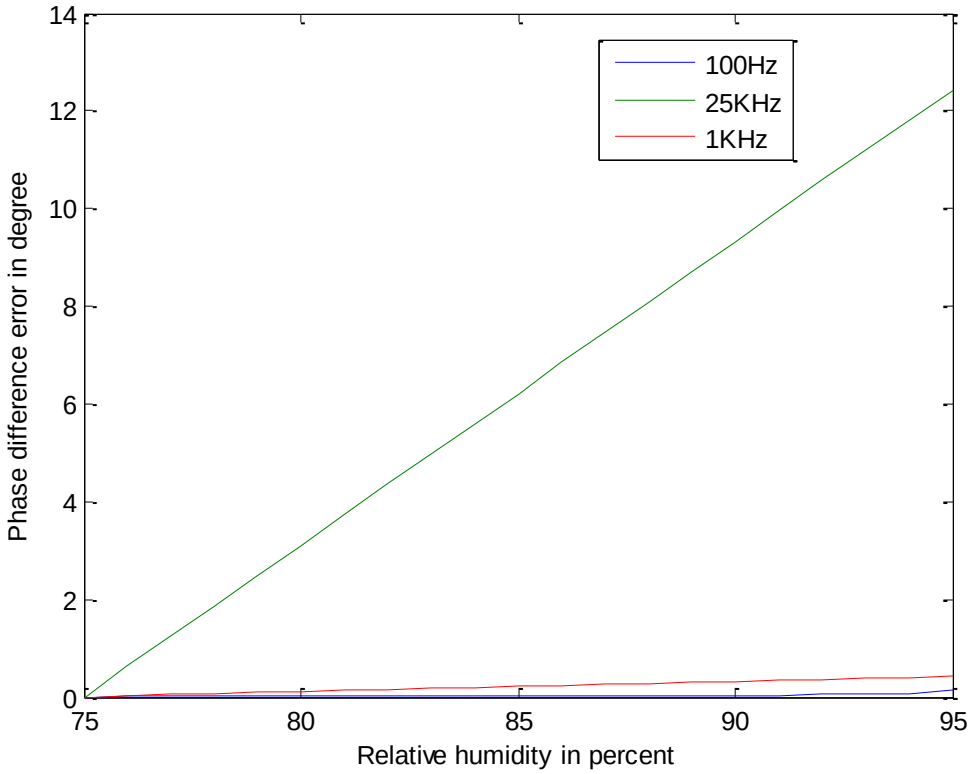

Figure 5-8 The effect of changing humidity on phase difference

More details of the evaluation of temperature and humidity will be given in the experimental chapters.

5.3 3D position calculation

So far in this section, the techniques used in the new ultrasound distance measurement have been introduced. Now, the working principles of the transformation 2, *'Position the receivers',* and transformation 3, *'Position the transmitter',* are introduced to show how the measured distances are used to locate the receivers and position the transmitter in 3D space.

After the distances between the transmitter and the receivers are measured at transformation 1, *'Measure the distances'*, the transmitter 3D positions are determined at transformation 3, *'Position coordinates'*, using the pre-measured position of the receivers. In earlier work as introduced in the previous chapter, the triangulation method used for position tracking requires the receivers to be located orthogonally. In practice, it is very difficult to satisfy this requirement, especially in later versions where up to eight receivers (see Figures 4.1 and 4.3) have to be precisely located at the corners of a cube. To improve the system flexibility, a new algorithm for position coordinate was developed to allow the receivers to be located arbitrarily at convenient positions [50].

First consider the following case, where 3 receivers, R_1, R_2 and R_3 are employed:

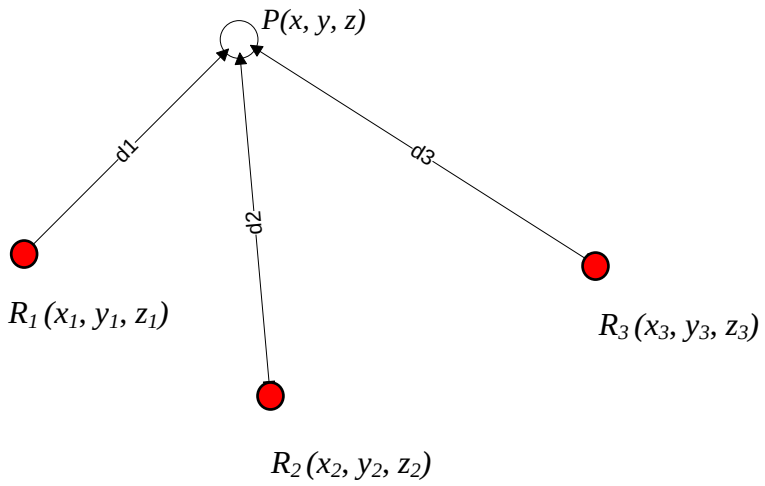

Figure 5-9 Locations of the transmitter position and three receivers

The coordinate of the position $p(x, y, z)$ can be evaluated by solving the following system of equations [44]:

$$\begin{cases} (x-x_1)^2+(y-y_1)^2+(z-z_1)^2=d_1^2 \\ (x-x_2)^2+(y-y_2)^2+(z-z_2)^2=d_2^2 \\ (x-x_3)^2+(y-y_3)^2+(z-z_3)^2=d_3^2 \end{cases} \quad 5\text{-}21$$

Where, x_n, y_n *and* z_n are the coordinates of *n*th receiver and d_n is the measured distance between the transmitter and corresponding receiver. The Newton iteration method shown in the following equation is used to solve the system of equations:

$$X_{n+1} = X_n - F(X_n)^{-1} f(X_n) \qquad n \geq 0$$

Where,

$$X_{n+1} = \begin{bmatrix} x_{n+1} \\ y_{n+1} \\ z_{n+1} \end{bmatrix} \qquad X_n = \begin{bmatrix} x_n \\ y_n \\ z_n \end{bmatrix}$$

$$F(X_n) = \begin{bmatrix} (2x_n - 2x_1) & (2y_n - 2y_1) & (2z_n - 2z_1) \\ (2x_n - 2x_2) & (2y_n - 2y_2) & (2z_n - 2z_2) \\ (2x_n - 2x_3) & (2y_n - 2y_3) & (2z_n - 2z_3) \end{bmatrix}$$

$$f(X_n) = \begin{bmatrix} (x - x_1)^2 + (y - y_1)^2 + (z - z_1)^2 - d_1^2 \\ (x - x_2)^2 + (y - y_2)^2 + (z - z_2)^2 - d_2^2 \\ (x - x_3)^2 + (y - y_3)^2 + (z - z_3)^2 - d_3^2 \end{bmatrix}$$

Estimation of the solution to these equation can be determined to any level of accuracy desired, but at the expense of considerable computational time, since the Jacobian matrix $\boldsymbol{F(X_n)}$ and the vector $\boldsymbol{f(X_n)}$ are calculated and multiplied together at every iteration.

In order to simplify the computation, a new approach is introduced to evaluate the solutions of Equation (5-21). First, it establishes a new coordinate system, so that the receivers have the coordinates $R_1(0,0,0)$, $R_2(x_2^{'},0,0)$ and $R_3(x_3^{'}, y_3^{'},0)$. This depends on the simple Euclidian observation that a single plane can always be drawn through any three points in space. This new coordinate system can be obtained by rotation and translation of the original coordinate system, and the positions of the receivers can be established using the following equations:

$$\begin{bmatrix} x'_{i,t} \\ y'_{i,t} \\ z'_{i,t} \\ 1 \end{bmatrix} = Tran\ (x_1, y_1, z_1)\ .\ \begin{bmatrix} x_i \\ y_i \\ z_i \\ 1 \end{bmatrix} \qquad \begin{bmatrix} x'_{i,tz} \\ y'_{i,tz} \\ z'_{i,tz} \\ 1 \end{bmatrix} = Rot\ (z, \alpha)\ .\ \begin{bmatrix} x_{i,t} \\ y_{i,t} \\ z_{i,t} \\ 1 \end{bmatrix}$$

$$\begin{bmatrix} x'_{i,tzy} \\ y'_{i,tzy} \\ z'_{i,tzy} \\ 1 \end{bmatrix} = Rot\ (y, \beta)\ .\ \begin{bmatrix} x'_{i,tz} \\ y'_{i,tz} \\ z'_{i,tz} \\ 1 \end{bmatrix} \qquad \begin{bmatrix} x'_{i} \\ y'_{i} \\ z'_{i} \\ 1 \end{bmatrix} = \begin{bmatrix} x'_{i,tzyx} \\ y'_{i,tzyx} \\ z'_{i,tzyx} \\ 1 \end{bmatrix} = Rot\ (x, \theta)\ .\ \begin{bmatrix} x'_{i,tzy} \\ y'_{i,tzy} \\ z'_{i,tzy} \\ 1 \end{bmatrix} \qquad 5\text{-}22$$

Where, i is the index of the receivers, **Tran**(x, y, z) and **Rot** (axis, angle) are the translation and rotation matrices:

$$Tran\ (x_1, y_1, z_1) = \begin{bmatrix} 1 & 0 & 0 & -x_1 \\ 0 & 1 & 0 & -y_1 \\ 0 & 0 & 1 & -z_1 \\ 0 & 0 & 0 & 1 \end{bmatrix} \qquad Rot\ (z, \alpha) = \begin{bmatrix} \cos\alpha & \sin\alpha & 0 & 0 \\ -\sin\alpha & \cos\alpha & 0 & 0 \\ 0 & 0 & 1 & 0 \\ 0 & 0 & 0 & 1 \end{bmatrix}$$

$$Rot\ (y, \beta) = \begin{bmatrix} \cos\beta & 0 & -\sin\beta & 0 \\ 0 & 1 & 0 & 0 \\ \sin\beta & 0 & \cos\beta & 0 \\ 0 & 0 & 0 & 1 \end{bmatrix} \qquad Rot\ (x, \theta) = \begin{bmatrix} 1 & 0 & 0 & 0 \\ 0 & \cos\theta & \sin\theta & 0 \\ 0 & -\sin\theta & \cos\theta & 0 \\ 0 & 0 & 0 & 1 \end{bmatrix}$$

The rotation angles α, β and θ on the corresponding axis can be determined as follows:

$$\alpha = \arctan\left(\frac{y_2 - y_1}{x_2 - x_1}\right) \qquad \beta = \arctan\left(\frac{z'_{2,x}}{x'_{2,x}}\right) \qquad \theta = \arctan\left(\frac{z'_{3,xy}}{y'_{3,xy}}\right)$$

After the coordinates of the receiver are determined using Equation (5-22), and substituting them into Equation (5-21) yields:

$$\begin{cases} x'^2 + y'^2 + z'^2 = d_1^2 \\ (x' - x_2')^2 + y'^2 + z'^2 = d_2^2 \\ (x' - x_3')^2 + (y' - y_3')^2 + z'^2 = d_3^2 \end{cases}$$

Where the solution, coordinates of the position in new coordinate system $p'(x', y', z')$ can be found directly with the following equations:

$$\left.\begin{array}{r} x' = \dfrac{x_2'^2 + d_1^2 - d_2^2}{2x_2'} \\ y' = \dfrac{y_3'^2 + d_1^2 - d_3^2 + x_3'^2 - 2x'x_3'}{2y_3'} \\ z' = \sqrt{d_1^2 - x'^2 - y'^2} \end{array}\right\} \quad \text{5-23}$$

As the rotation angles α, β and θ have already been determined earlier, the position in the original coordinate system can be simply obtained by multiplying the above solutions with an inverse transformation matrix, which is derived as follows:

$$\begin{bmatrix} x \\ y \\ z \\ 1 \end{bmatrix} = \left[Rot\,(x,\theta).Rot\,(y,\beta).Rot\,(z,\alpha).Tran(x_1, y_1, z_1)\right]^{-1}.\begin{bmatrix} x' \\ y' \\ z' \\ 1 \end{bmatrix}$$

$$= \begin{bmatrix} \cos\beta\cos\alpha & \cos\beta\sin\alpha & \sin\beta & a \\ -\sin\theta\sin\beta\sin\alpha - \cos\theta\sin\alpha & -\sin\theta\sin\beta\sin\alpha + \cos\theta\cos\alpha & \sin\theta\cos\beta & b \\ -\cos\theta\sin\beta\cos\alpha + \sin\theta\sin\alpha & -\cos\theta\sin\beta\cos\alpha - \sin\theta\cos\alpha & \cos\theta\cos\beta & c \\ 0 & 0 & 0 & 1 \end{bmatrix}^{-1} \cdot \begin{bmatrix} x' \\ y' \\ z' \\ 1 \end{bmatrix}$$

Where

$$a = -x_1 \cos\beta\cos\alpha - y_1 \cos\beta\sin\alpha - z_1 \sin\beta$$
$$b = x_1(\sin\theta\sin\beta\cos\alpha + \cos\theta\sin\alpha) + y_1(\sin\theta\sin\beta\sin\alpha - \cos\theta\cos\alpha) - z_1 \sin\theta\cos\beta$$
$$c = x_1(\cos\theta\sin\beta\cos\alpha - \sin\theta\sin\alpha) + y_1(\cos\theta\sin\beta\sin\alpha + \sin\theta\cos\alpha) - z_1 \cos\theta\cos\beta$$

$$\begin{bmatrix} x \\ y \\ z \\ 1 \end{bmatrix} = \begin{bmatrix} \cos\beta\cos\alpha & -\sin\theta\sin\beta\cos\alpha - \cos\theta\sin\alpha & -\cos\theta\sin\beta\cos\alpha + \sin\theta\sin\alpha & x_1 \\ \cos\beta\sin\alpha & -\sin\theta\sin\beta\sin\alpha + \cos\theta\cos\alpha & -\cos\theta\sin\beta\sin\alpha - \sin\theta\cos\alpha & y_1 \\ \sin\beta & \sin\theta\cos\beta & \cos\theta\cos\beta & z_1 \\ 0 & 0 & 0 & 1 \end{bmatrix} \cdot \begin{bmatrix} x' \\ y' \\ z' \\ 1 \end{bmatrix}$$

5-24

This algorithm has a much higher computational efficiency than the Newton iteration introduced earlier, and can be seen clearly in the data flow diagram DFD shown in Figure 5.10. The transformation 3.1, '*Calculate the receivers' coordinates in new coordinate system'* and transformation 3.2, '*Calculate inverse transformation matrix*', are activated during the system initialization to transfer the coordinates of the receivers into the new coordinate system and calculate the inverse transformation matrix.

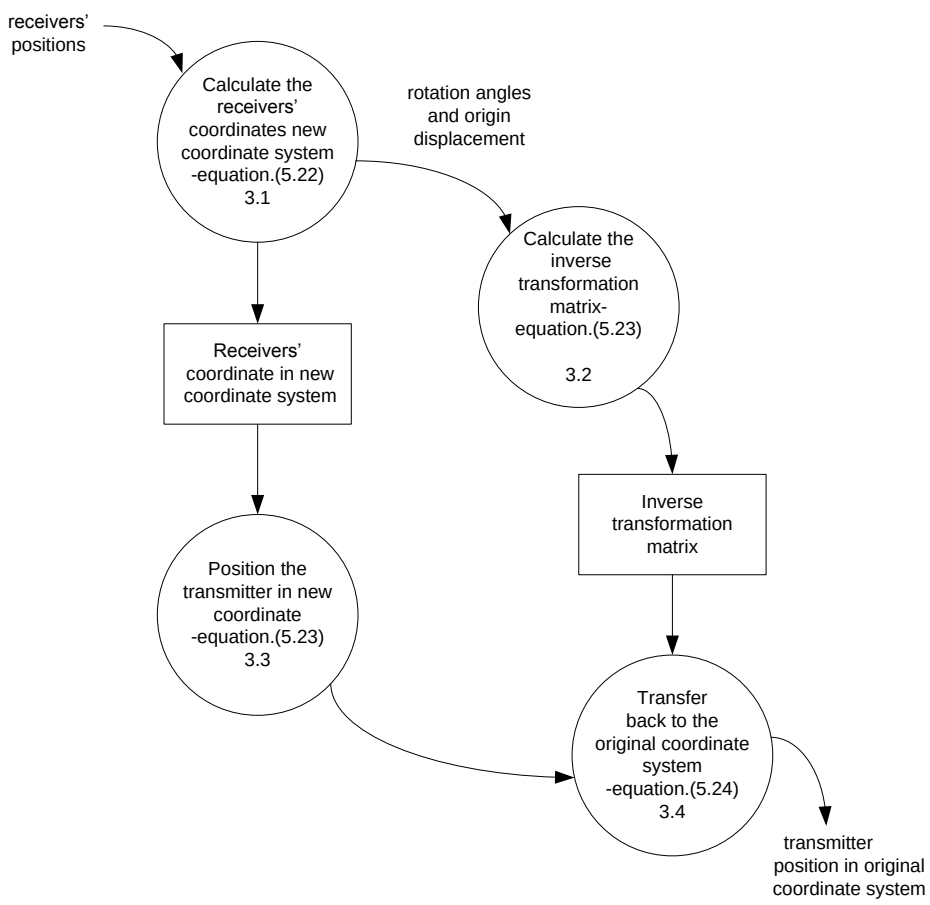

Figure 5-10 DFD- Transformation three receivers

The results are stored in the corresponding data store. Transformation 3.3, '*Position in new coordinate system*', and transformation 3.4, '*Transfer back to the original coordinate system*', are activated. First, calculated position is directly determined with equation (5-23) at transformation 3.3, then the result is transferred back to the original coordinate system by multiplying it with the pre-calculated inverse transformation matrix. Obviously, this algorithm requires much less computational time during each position change.

As shown in Equation (5-23), the accuracy of the position depends on the distance measurement errors denoted Δd_1, Δd_2 and Δd_3.

Assuming that the errors are small compared to the distance being measured, so that errors in the calculated coordinates $\Delta x', \Delta y', \Delta z'$ can be determined by partial differential:

$$\begin{bmatrix} \Delta x' \\ \Delta y' \\ \Delta z' \end{bmatrix} = \begin{bmatrix} \frac{\partial x'}{\partial d_1} & \frac{\partial x'}{\partial d_2} & \frac{\partial x'}{\partial d_3} \\ \frac{\partial y'}{\partial d_1} & \frac{\partial y'}{\partial d_2} & \frac{\partial y'}{\partial d_3} \\ \frac{\partial z'}{\partial d_1} & \frac{\partial z'}{\partial d_2} & \frac{\partial z'}{\partial d_3} \end{bmatrix} . \begin{bmatrix} \Delta d_1 \\ \Delta d_2 \\ \Delta d_3 \end{bmatrix} \qquad 5\text{-}25$$

Then, substituting Equation (5-23) into Equation (5-25), yields:

$$\begin{bmatrix} \Delta x' \\ \Delta y' \\ \Delta z' \end{bmatrix} = \begin{bmatrix} \frac{d_1}{\partial d_1} & -\frac{d_2}{\partial d_2} & 0 \\ \frac{d_1'}{y_3} - \frac{d_1 x_3}{y_3 x_2} & \frac{d_2 x_3'}{x_2 y_3} & -\frac{d_3}{y_3} \\ b & e & f \end{bmatrix} . \begin{bmatrix} \Delta d_1 \\ \Delta d_2 \\ \Delta d_3 \end{bmatrix} \qquad 5\text{-}26$$

Where, the *b*, *e* and *f* are derived using the MATLAB symbolic toolbox:

$$b = 1/4(4d_1^2 - (x_2^2 + d_1^2 - d_2^2)^2 / x_2^2 - (y_3^2 + d_1^2 - d_3^2 + x_3^2 - (x_2^2 + d_1^2 - d_2^2)/x_2 x_3)^2 / y_3^2)^{1/2}$$
$$(8d_1 - 4(x_2^2 + d_1^2 - d_2^2)/x_2^2 d_1 - 2(y_3^2 + d_1^2 - d_3^2 + x_3^2 - (x_2^2 + d_1^2 - d_2^2)/x_2 x_3 / y_3^2 (2d_1 - 2d_1 / x_2 x_3))$$

$$e = 1/4(4d_1^2 - (x_2^2 + d_1^2 - d_2^2)^2 / x_2^2 - (y_3^2 + d_1^2 - d_3^2 + x_3^2 - (x_2^2 + d_1^2 - d_2^2)/x_2 x_3)^2 / y_3^2)^{1/2}$$
$$(4(x_2^2 + d_1^2 - d_2^2)/x_2^2 d_2 - 4(y_3^2 + d_1^2 - d_3^2 + x_3^2 - (x_2^2 + d_1^2 - d_2^2)/x_2 x_3 / y_3^2 d_2 / x_2 x_3)$$

$$f = 1/4(4d_1^2 - (x_2^2 + d_1^2 - d_2^2)^2 / x_2^2 - (y_3^2 + d_1^2 - d_3^2 + x_3^2 - (x_2^2 + d_1^2 - d_2^2)/x_2 x_3)^2 / y_3^2)^{1/2}$$
$$(y_3^2 + d_1^2 - d_3^2 + x_3^2 - (x_2^2 + d_1^2 - d_2^2)/x_2 x_3)/y_3^2 d_3$$

5.4 Positioning of the receivers

Precise determination of the transmitter position requires accurate estimation of the receivers' position. However, in the previous work by Mahajan [4] and Martin [6], no comment was made on where to position the receivers. In this section the procedure and algorithms used by the new 3D measurement system for positioning the transceivers will be introduced and details given.

First, establish the transceivers' positions (R_1, R_2 and R_3) in an *xyz* coordinate system ***R,*** as shown in figure 5.11.

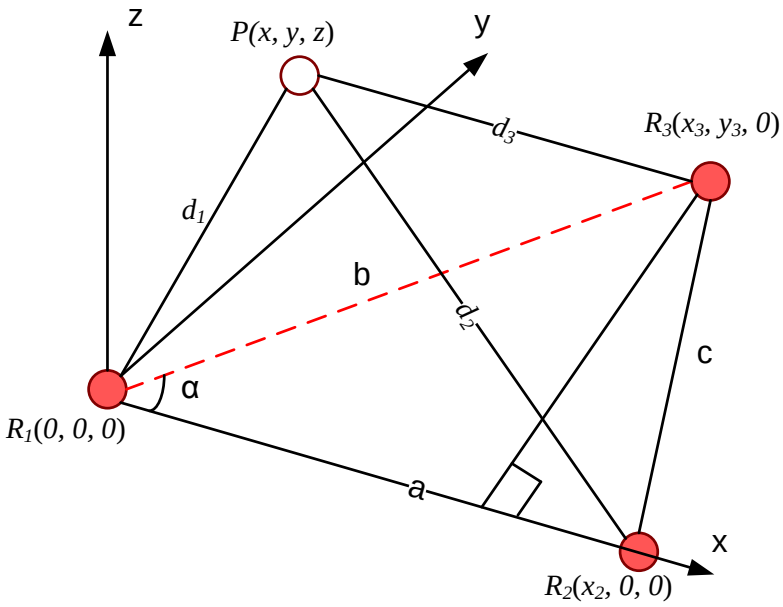

Figure 5-11 Positions of the transceivers' in coordinate system R

Transceiver 1 is assumed to be at the origin so its position will be $R_1(0, 0, 0)$. The coordinate system is such that transceiver 2 is on the x-axis, and its position is $R_2(x_2, 0, 0)$. Thus the distance between transceiver R_1 and R_2 is x_2, which can be measured quite simply with multiple-frequency continuous wave frequency modulation (MFCWFM) if transceiver 2 is used as a transmitter. The distances between the transceivers, R_1R_2, R_1R_3, and R_2R_3 are *a*, *b* and *c* respectively, as shown in Figure 5.11.

$$x_2 = a \tag{5-27}$$

Here the z-axis is orthogonal with the plane $R_1R_2R_3$, which is determined by the three transceivers, and is positioned such that transceiver 3 has the coordinate $R_3(x_3, y_3, 0)$ with:

$$x_3 = b.\cos\alpha$$

Then, substituting,

$$\cos\alpha = \frac{a^2 + b^2 - c^2}{2ab}$$

This yields:

$$x_3 = \frac{a^2 + b^2 - c^2}{2a} \tag{5-28}$$

Where b, c are also measured using the MFCWFM system with transceiver 3 as a transmitter. Once x_3 is determined, y_3 can then be calculated:

$$y_3 = \sqrt{b^2 - x_3^2} \tag{5-29}$$

Accurate determination of the receivers' coordinates depends totally on the precision of the measurements of the distances between the receivers. Thus the errors in the distance measurement, Δd_1, Δd_2 and Δd_3 will have direct consequences for the calculated errors in the position coordinates $\Delta a, \Delta b$ and Δc. If it is assumed that the errors in distance measurements are very small compared to the distances between the transceivers, then:

$$\begin{bmatrix} \Delta x_2 \\ \Delta x_3 \\ \Delta y_3 \end{bmatrix} = \begin{bmatrix} \frac{\partial x_2}{\partial a} & \frac{\partial x_2}{\partial b} & \frac{\partial x_2}{\partial c} \\ \frac{\partial x_3}{\partial a} & \frac{\partial x_3}{\partial b} & \frac{\partial x_3}{\partial c} \\ \frac{\partial y_3}{\partial a} & \frac{\partial y_3}{\partial b} & \frac{\partial y_3}{\partial c} \end{bmatrix} . \begin{bmatrix} \Delta a \\ \Delta b \\ \Delta c \end{bmatrix}$$

Substituting Equations (5-27), (5-28) and (5-29) into the above equation, yields:

$$\begin{bmatrix} \Delta x_2 \\ \Delta x_3 \\ \Delta y_3 \end{bmatrix} = \begin{bmatrix} 1 & 0 & 0 \\ 1-\frac{s}{2a^2} & \frac{b}{a} & -\frac{c}{a} \\ \frac{s^2-2sa^2}{2a^2\sqrt{4a^2b^2-s^2}} & \frac{2ba^2-sb}{a\sqrt{4a^2b^2-s^2}} & \frac{sc}{a\sqrt{4a^2b^2-s^2}} \end{bmatrix} . \begin{bmatrix} \Delta a \\ \Delta b \\ \Delta c \end{bmatrix} \qquad 5\text{-}30$$

Where, $s = a^2 + b^2 - c^2$

After the receiver positions are determined in the coordinate system ***R***, the next step is to transfer the receivers' coordinates to the machine coordinate. Equation 5.24 is used to transfer data to machine coordinates.

5.5 Summary

This chapter has introduced the working principle of the enhanced ultrasonic 3D measurement system, with the aspects of its functionality explained using Data Flow Diagrams (DFDs). The detailed hardware and software implementations will be introduced in Chapter 6.

This new 3D measurement system employs new techniques and algorithms for distance measurement and transmitter/receiver positioning. Compared with the previous measurement system, these new techniques improved the overall performance of the new system in the following aspects:

1. *Higher accuracy and resolution:* The concept of MFCWFM introduced in Section 5.2.1 allows the distance to be measured continuously by monitoring the phase difference between transmitted and received ultrasonic signals. In practice, the prototype MFCWFM system demonstrated high linear measurement accuracy of.019mm over the axis stroke. This will be discussed in Chapter 8.

2. *Better adaptability and flexibility:* This is achieved with the new algorithms and procedures for receiver and transmitter positioning. Unlike the previous 3D measurement system, where the receivers have to be located orthogonally, these new algorithms allow the receivers to be placed at arbitrary positions to adapt to different industrial environments. Moreover, the better flexibility is achieved with the relatively simple procedure introduced in Section 5.4 for receiver positioning, allows receivers to be easily relocated according to changes in the environment.

Chapter 6 Prototype measurement system and experimental tests

6.1 Introduction

The last chapter introduced new techniques and algorithms for high accuracy distance measurement, precise receiver/transmitter positioning and to improve the accuracy and system flexibility of previous ultrasonic 3D measurement systems. Based on those techniques, a prototype 3D measurement system was developed and this chapter gives a detailed description of the implementation of the hardware and software. Figure 6.1 shows a block diagram of the prototype's hardware.

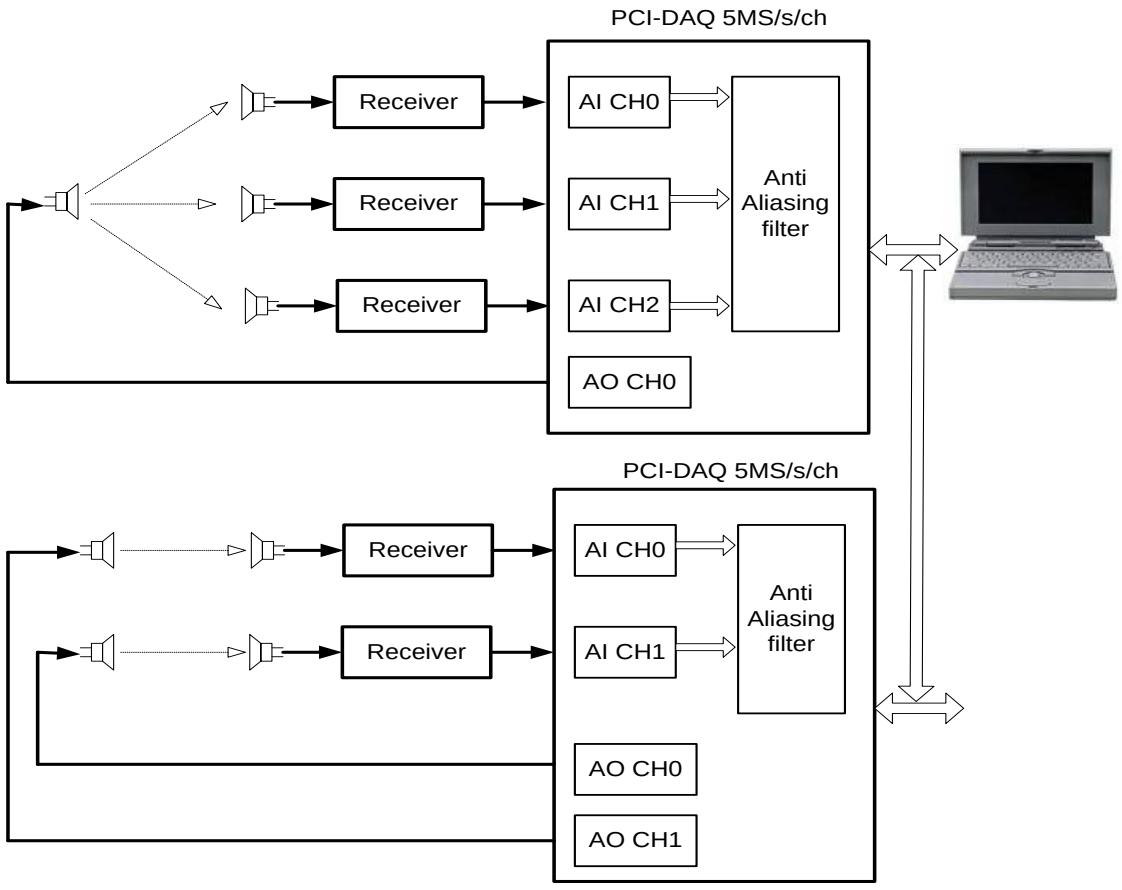

Figure 6-1 Block diagram of the new 3D measurement system hardware

Effectively the system is in two parts. In the first, ultrasound is transmitted to the three receivers located around the workspace area to measure the 3D position of the transmitter. The second part is used to evaluate the temperature and humidity within the workspace. Ultrasound is radiated from each of two transmitters to two corresponding receivers, see Figure 6.1. The signals are then sent to Data Acquisition card (PCI-6110). The computer runs a LABVIEW application to generate and modulate the ultrasound signals and to collect process and display the measured data.

6.2 Transmitters and transceivers

Piezoceramic ultrasonic transducers, see Figure 6.2 [54], are used as both transmitters and receivers. The frequency responses are shown in Figure 6.3(a) [54], the red colour recording to transmitter response and blue one recording to receiver response. The directionality of the transducers for a 25kHz signal is shown in Figure 6.3(b).

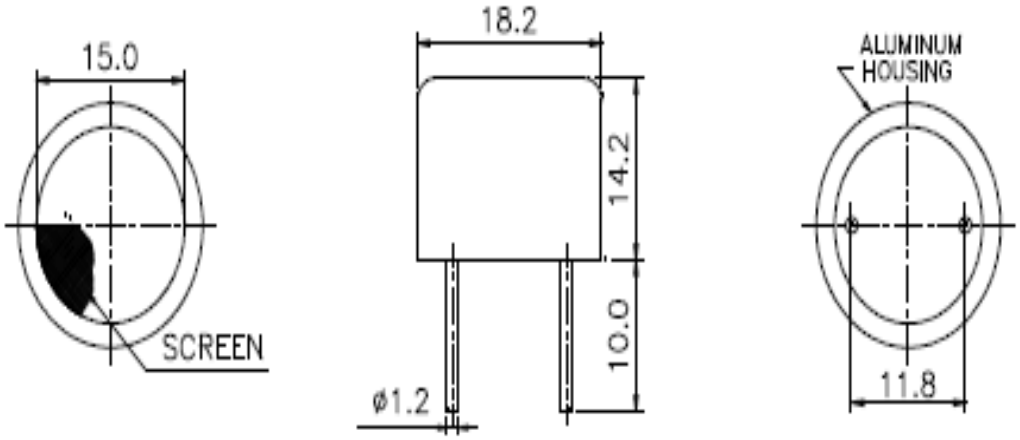

Figure 6-2 Dimensions of the ultrasonic transducer in mm

As the new 3D measurement system uses MFCWFM technique for distance measurement, the transmitter is selected to emit continuous ultrasound signal directly from the DAQ output.

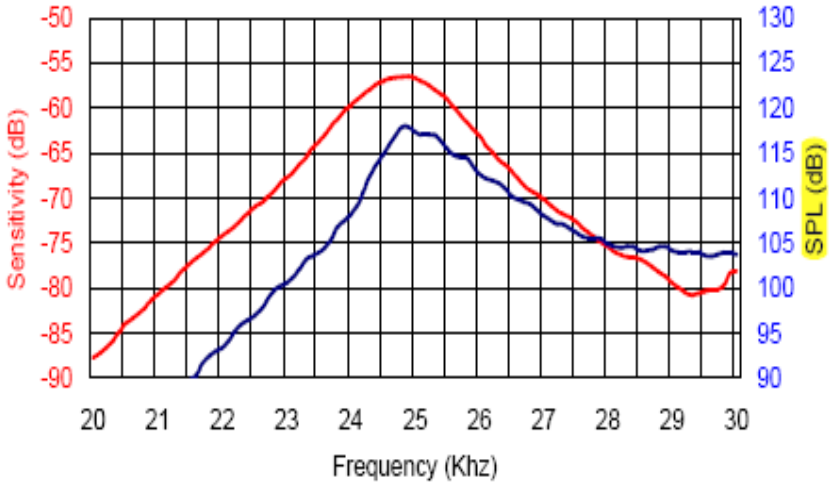

(a)

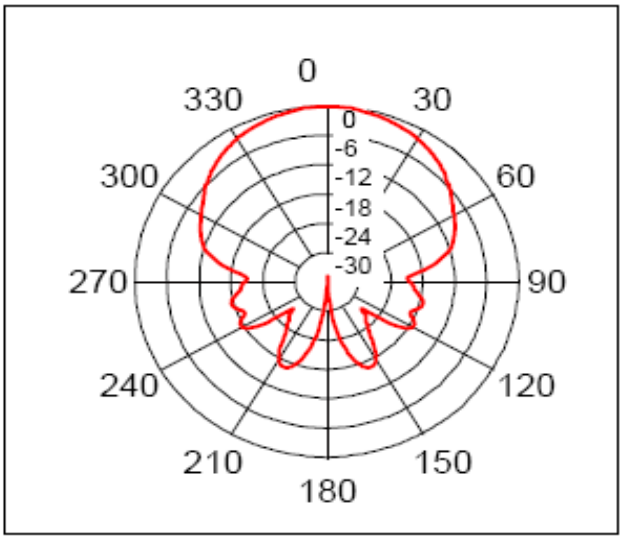

(b)

Figure 6-3 (a) Sensitivity of the ultrasonic transducer
(b) Directionality of the transducer

The ultrasound waves are picked up by the transducers acting as receivers and amplified by three stages as shown in Figure 6.4. The output of this 'limiting amplifier' circuit was constant amplitude for a wide range of input amplitudes, the output then went to the DAQ input.

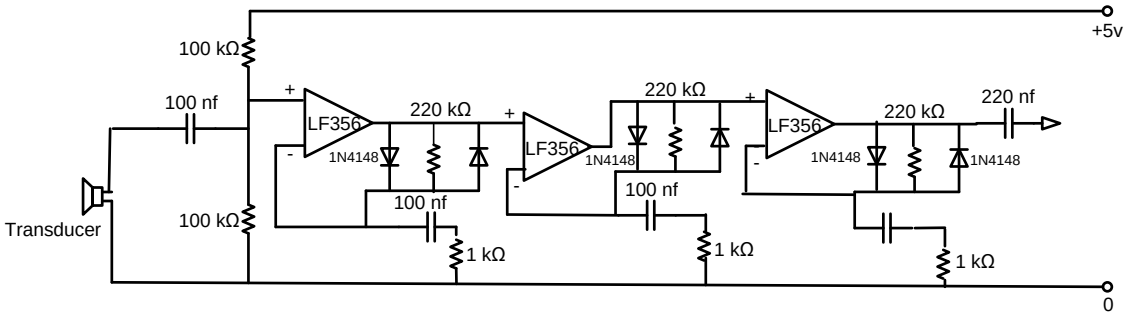

Figure 6-4 Circuit of the receiver amplifier

6.3 DAQ card interface (PCI-6110)

The PCI-6110 was produced by National Instruments (NI), contains seven 24-bit counters and three 16-bit counters. The counters are divided into the following three groups:

1. Analog input __ two 24-bit, two 16-bit counters
2. Analog input __ three 24-bit, one 16-bit counters
3. General __ purpose counter/time functions __ two 24-bit counters

The PCI-6110 device has a maximum sampling rate of 5 MS/s regardless of whether 1 or 4 channels are acquiring data, and this was the main reason for choosing this device.

The PCI-6110 device has bipolar inputs only, with the input voltage range of 20 V (±10V). The software-programmable gain on this device increases its overall flexibility by matching the input signal ranges to those which the ADC can accommodate. It has gains of 0.2, 0.5, 1, 2, 5, 10, 20, and 50, and is suited for a wide variety of signal levels. With the proper gain setting, the full resolution of the ADC can be used to measure the input signal. Table 6.1 shows the overall input range and precision according to the gain used.

Table 6-1 Actual range and measurement resolution

Range configuration	Gain	Actual Input Range	Resolution
-10 to +10 V			
	5.0	-2 to +2 V	976.56 μV
	10.0	-1 to +1 V	488.28 μV
	20.0	-500 to +500 mV	244.14 μV

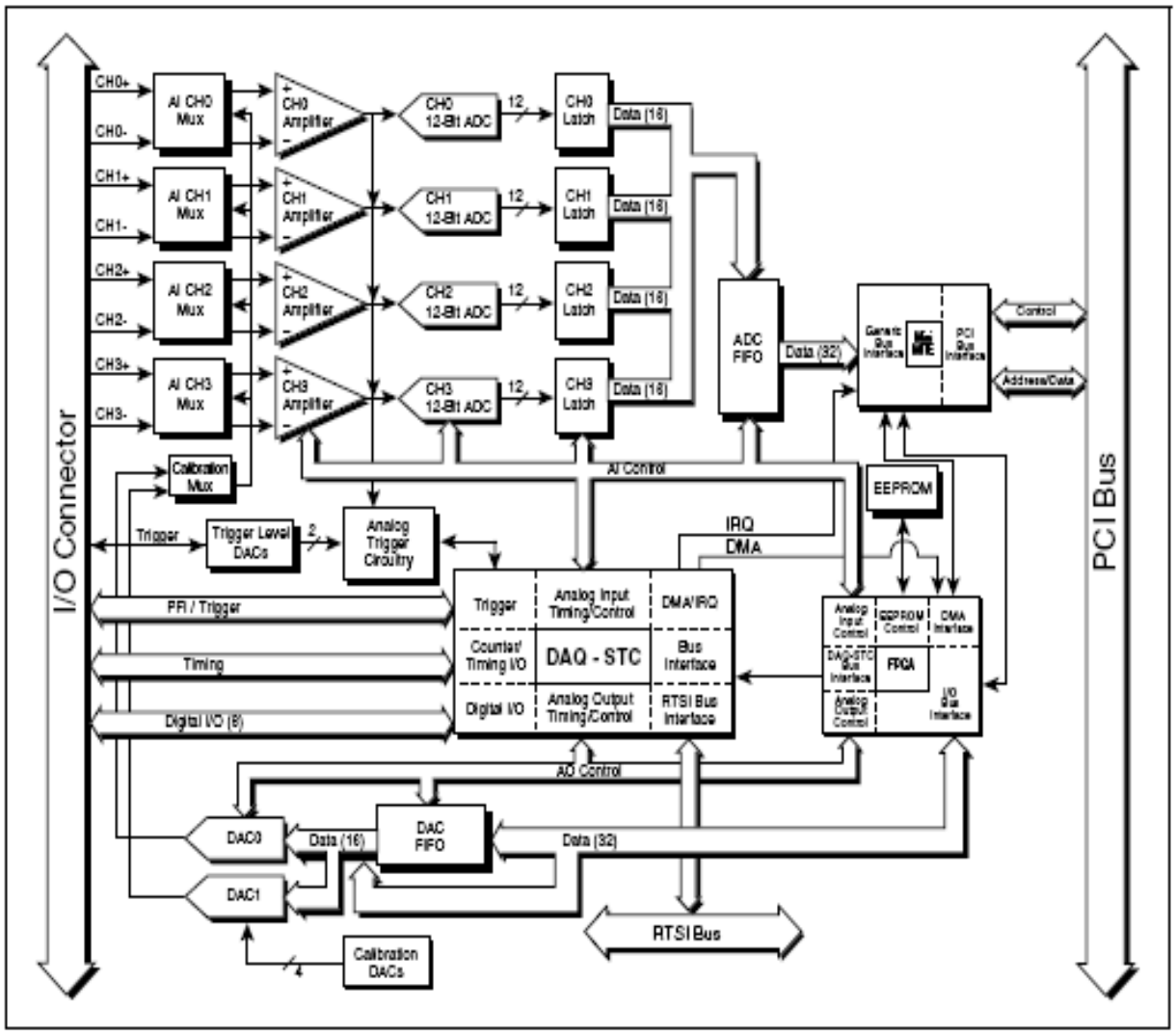

Figure 6-5 PCI-6110 Block diagram

The analogue input signals are AI CH <0..3> + and AI CH <0..3> - as shown in Figure 6.5 [57]. The AI CH <0..3> + signals are routed to the positive input of the programmable gain instrumentation amplifier (PGIA), and signals connected to AI CH <0..3> - are routed to the negative input of the PGIA, as shown in Figure 6.6. The PGIA applies gain and common-mode voltage rejection, and presents high input impedance to the analogue input signals connected to the PCI-6110. The PGIA converts the two input signals to a single signal that is the difference between them multiplied by the gain

setting of the amplifier, see Figure 6.6. The amplifier output voltage is referenced to the ground for the device. The PIC-6110 device A/D converter (ADC) measures this output voltage when it performs the A/D conversions.

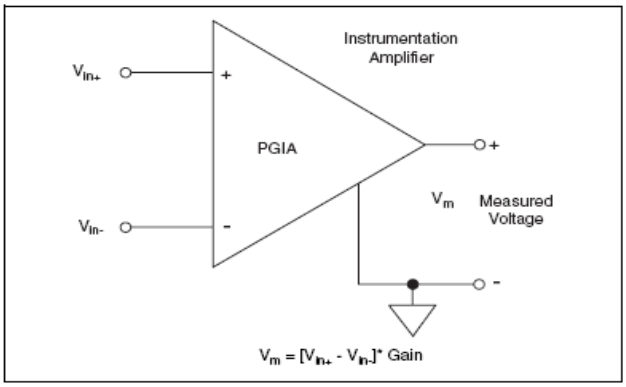

Figure 6-6 Programmable gain instrumentation amplifier (PGIA)

The analogue output signals are DAC0OUT, DAC1OUT, and AOGND. Figure 6.7 shows how the analogue output connections to the PCI-6110 device.

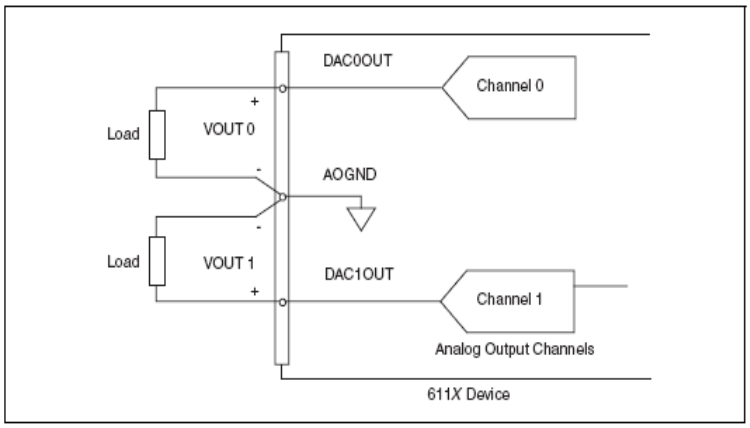

Figure 6-7 Analogue output connections

DAC0OUT is the voltage output signal for analogue output channel 0, DAC1OUT is the voltage output signal for analogue output channel 1, and AOGND is the ground reference signal for the analogue output channels. More details in appendix B

The I/O connector for PCI-6110 has 68 pins whose assignments are shown in Figure 6.8. The PCI-6110 is connected to subsequent devices using the SH6868EP shielded cable.

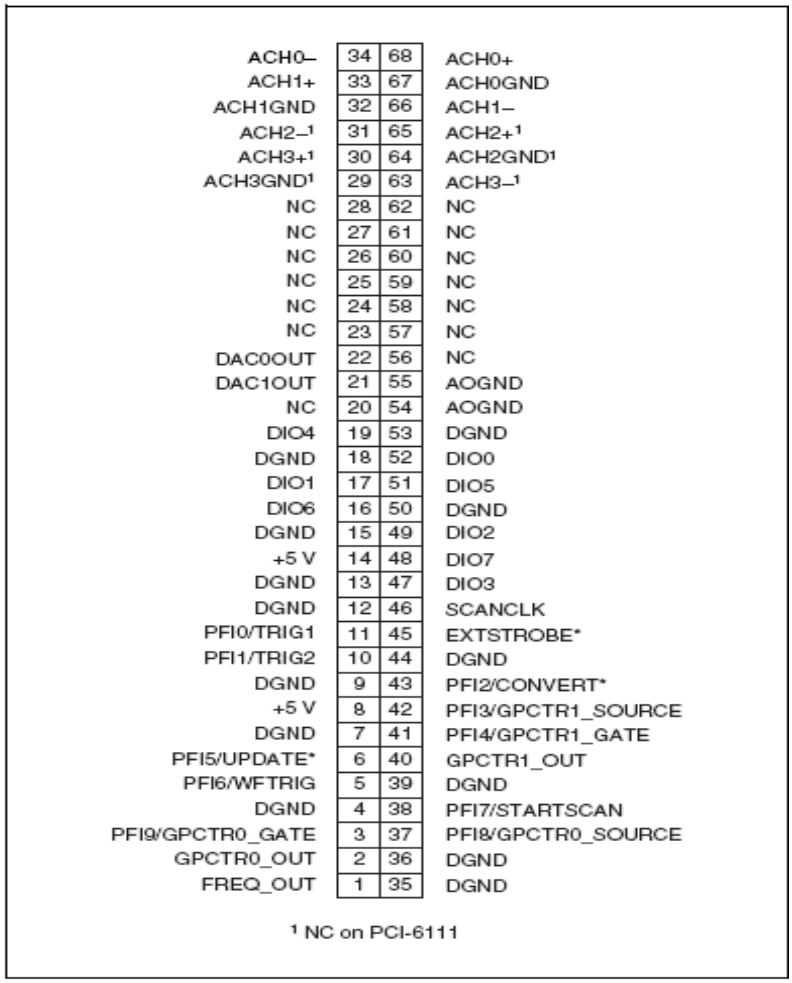

ACH0–	34	68	ACH0+
ACH1+	33	67	ACH0GND
ACH1GND	32	66	ACH1–
ACH2–[1]	31	65	ACH2+[1]
ACH3+[1]	30	64	ACH2GND[1]
ACH3GND[1]	29	63	ACH3–[1]
NC	28	62	NC
NC	27	61	NC
NC	26	60	NC
NC	25	59	NC
NC	24	58	NC
NC	23	57	NC
DAC0OUT	22	56	NC
DAC1OUT	21	55	AOGND
NC	20	54	AOGND
DIO4	19	53	DGND
DGND	18	52	DIO0
DIO1	17	51	DIO5
DIO6	16	50	DGND
DGND	15	49	DIO2
+5 V	14	48	DIO7
DGND	13	47	DIO3
DGND	12	46	SCANCLK
PFI0/TRIG1	11	45	EXTSTROBE*
PFI1/TRIG2	10	44	DGND
DGND	9	43	PFI2/CONVERT*
+5 V	8	42	PFI3/GPCTR1_SOURCE
DGND	7	41	PFI4/GPCTR1_GATE
PFI5/UPDATE*	6	40	GPCTR1_OUT
PFI6/WFTRIG	5	39	DGND
DGND	4	38	PFI7/STARTSCAN
PFI9/GPCTR0_GATE	3	37	PFI8/GPCTR0_SOURCE
GPCTR0_OUT	2	36	DGND
FREQ_OUT	1	35	DGND

[1] NC on PCI-6111

Figure 6-8 I/O connector pin assignment for PCI-6110

Note that in the new 3D measurement system the positive channels are connected to the ground channels.

System software

In addition to the hardware introduced so far, the new 3D measurement system also includes software which;

- *Generates the signals*: three stable frequencies (100Hz, 1kHz and 25kHz), with sampling rate 250kS/s for 25kHz, 10kS/s for both 100Hz and 1kHz.
- *Modulates the signals*: using a frequency modulation (FM) technique to modulate the 25kHz carrier frequency at 100Hz and 1kHz.
- *Demodulates the signals*: demodulates and separates the signals at the receiver stage and measure the phase difference between transmitted and received signal for each of the frequencies.
- *Data processing*: using the algorithms introduced in the previous chapter, determines the receivers and transmitter position coordinates.
- *Data display*: provides different graphic views of the data; local velocity of sound, distance, temperature and humidity within the work space.

6.4 Signal generation

The new 3D measurement system uses MFCWFM for distance measurement so there is a need to generate three sine waves with stable frequencies of 100Hz, 1kHz and 25kHz.

LABVIEW software is used to generate a stable frequency sine wave. Figure 6.9 shows the procedure used to generate an array containing a sine wave. The reset phase determines the initial phase of the sine wave. The default is TRUE. If reset phase is TRUE, LABVIEW sets the initial phase to phase in. If reset phase is FALSE, LABVIEW uses the value of phase out from when the vi was last executed as the initial phase of sine wave. The amplitude set as 1 for all frequencies. Figure 6.10 shows the device for generating a waveform containing the sine waves, the sampling rate is set as 10kS/s for both 100Hz and 1Hz, and 250kS/s for frequency 25kHz.

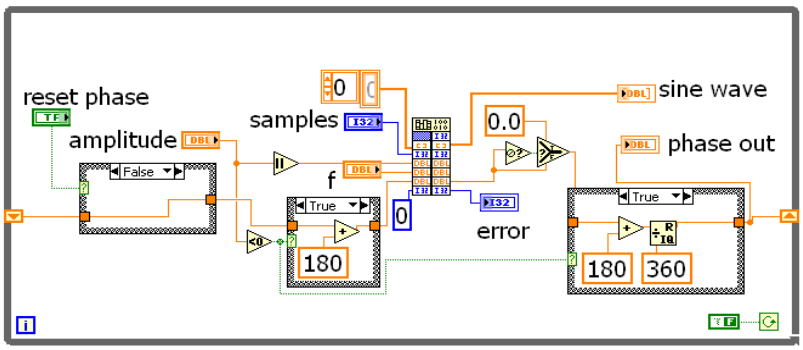

Figure 6-9 Generation of an array containing a sine wave

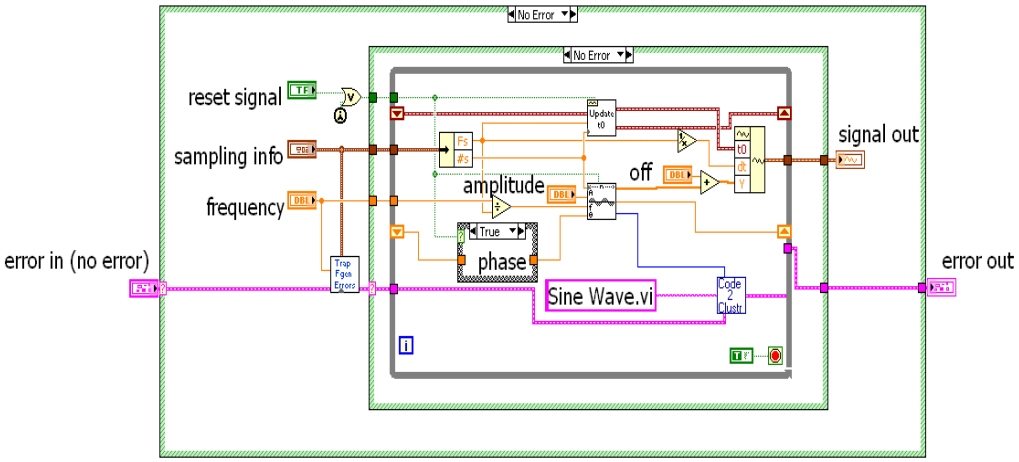

Figure 6-10 Generation of a waveform containing a sine wave

Figures 6.9 and 6.10 show a simple method for the generation of a sine wave signal with the possibility of changing the frequency, amplitude, sampling information and sampling rate. This method is used instead of normal circuit hardware, which would be likely to have had problems with stability of the frequency, and changing parameters such as amplitude, frequency, sampling rate and sampling information.

6.5 FM modulation

The transducers have frequency response which peaks at 25kHz, and this was used as the carrier frequency. However it was necessary to transmit and receive 100 Hz and 1kHz

signals using the same transducers. This was achieved by frequency modulation of the carrier frequency, which avoided errors in measuring phase difference produced by amplitude variations.

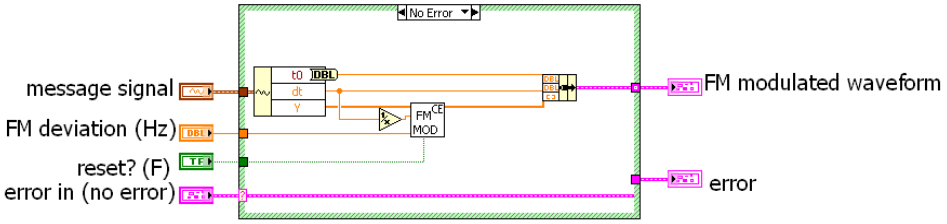

Figure 6-11 Frequency modulation device

After generation, the 100Hz and 1kHz signals were added together, see Figure 6.11 which shows the FM device. The FM deviation specifies the desired frequency deviation of the frequency modulated signal returned in the FM modulated waveform output. In frequency modulation, frequency deviation refers to the maximum absolute difference, during a specified period between the instantaneous frequency of the modulated wave and the carrier frequency. The new 3D measurement system used an FM deviation of 100Hz because, in tests with the transducers, 100Hz was sufficient to cover all amplitude variations at 25kHz, with the frequency responses shown in Figure 6.3(a). The output of Figure 6.11 is a FM modulated waveform containing the baseband signal data and the complex envelope of the frequency-modulated signal which contains the following elements:

- **t0:** trigger (start) time of the signal data.
- **dt:** time interval between data points in the signal data.
- **y:** complex- valued time domain data array, the real and imaginary parts of this complex data array correspond to the in-phase (I) and quadrature-phase (Q) data, respectively.

The output frequency-modulated wave is described by the following equation:

$$FM = e^{\left(2\pi \frac{frequency\,\text{deviation}}{f_s} \int ((\text{message signal})dt + \text{carrier phase})\right)}$$

6-1

Where, f_s is the sampling frequency.

The output of the modulated FM function (FM modulated waveform) connects to the input complex waveform of the fractional resample function as shown in Figure 6.12. To resample a waveform, a desired sample rate (250kS/s) that differs from the existing sample rate of the input complex waveform entered. To realign a waveform without changing its sample rate, input a value to the desired sample rate parameter equal to the existing sample rate. In this case the initial sample offset parameter (sec) is set as zero to resample a waveform without changing the relative timing offset between the input and output complex waveforms.

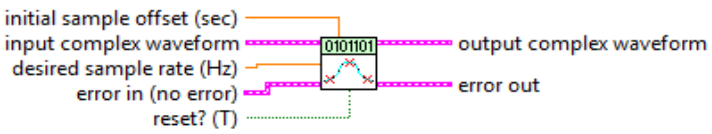

Figure 6-12 Fractional resample

The carrier frequency is applied in an upconvert baseband function as shown in Figure 6.13. This function converts the baseband signal data to its real passband equivalent. Upconverted data of the specified bandwidth is returned in the passband waveform output. Baseband waveform contains envelope signal data for upconversion to its passband equivalent which contains the following arrays:

- **t0:** specifies the trigger (start) time of the acquired signal.
- **dt:** specifies the time interval between data points in the acquired signal.
- **y:** specifies the complex-valued time domain data array. The real and imaginary parts of this complex data array correspond to the in-phase (I) and quadrature-phase (Q) data, respectively.

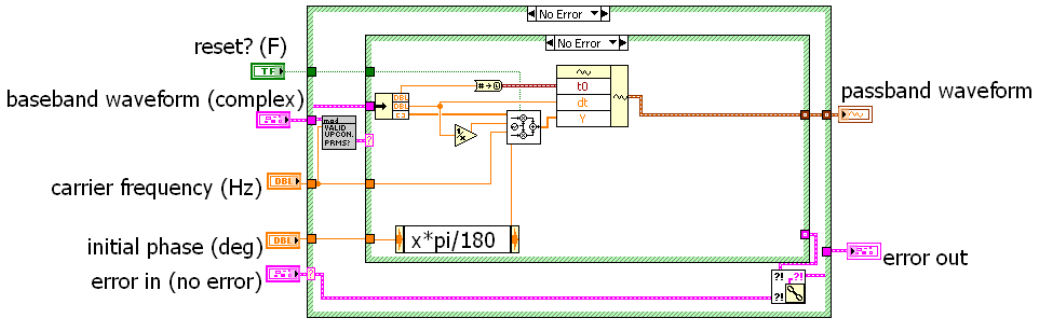

Figure 6-13 Upconvert baseband

The carrier frequency is the centre of the passband, the incoming signal is upconverted to centre around this frequency. Input the desired carrier frequency of the outgoing signal to this control. Outputs the upconverted signal in passband form, which contains the following elements:

- **t0:** trigger (start) time of the acquired signal.
- **dt:** time interval between data points in the acquired signal.
- **y:** the upconverted information signal array.

The DAQmx write function (Figure 6.14) is used to write samples to the task or virtual channels specified in DAQmx create channel function as shown in Figure 6.15. The instances specify the format of the samples to write, whether to write one or multiple samples, and whether to write one or multiple channels. In this case the DAQmx write is used to write one channels ao0 with multiple samples. The DAQmx create channel function is used for the created output channel (ao0) or input channels (ai0, ai1, ai2, ai3) for each PCI-6110.

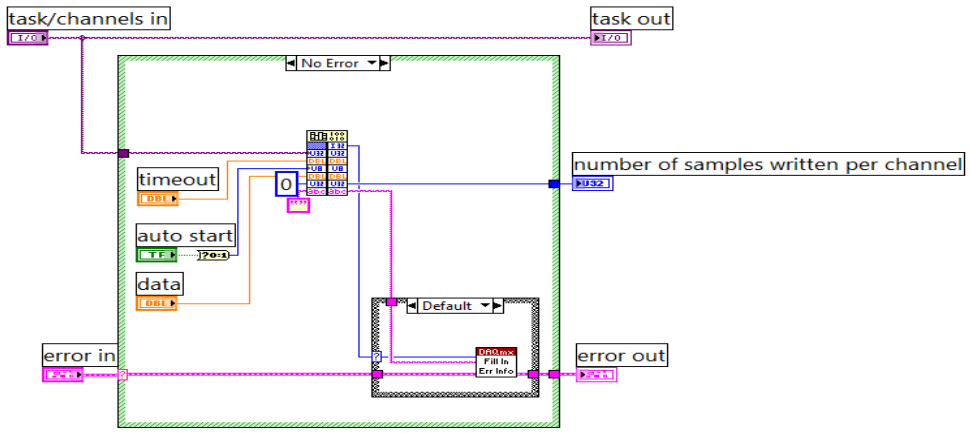

Figure 6-14 DAQmx write

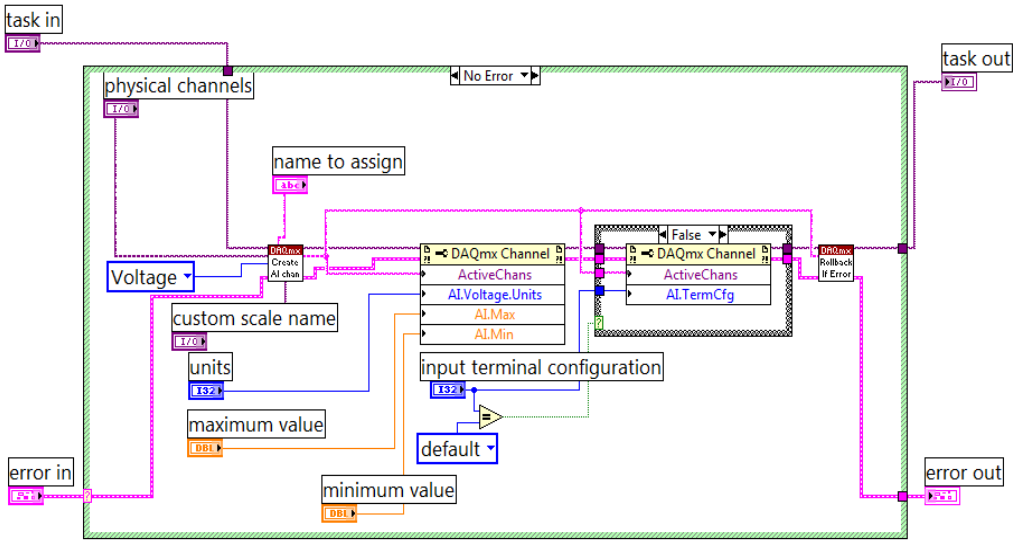

Figure 6-15 DAQmx creates a virtual channel

DAQmx Timing

DAQmx timing used to configure the number of samples to acquire or generate a buffer when needed. For high resolution the sampling rate was set as 250kS/s per channel and sample mode set for continuous sampling. These parameters were used for both transmitted and received signals. Figure 6.16 shown the block diagram for this function.

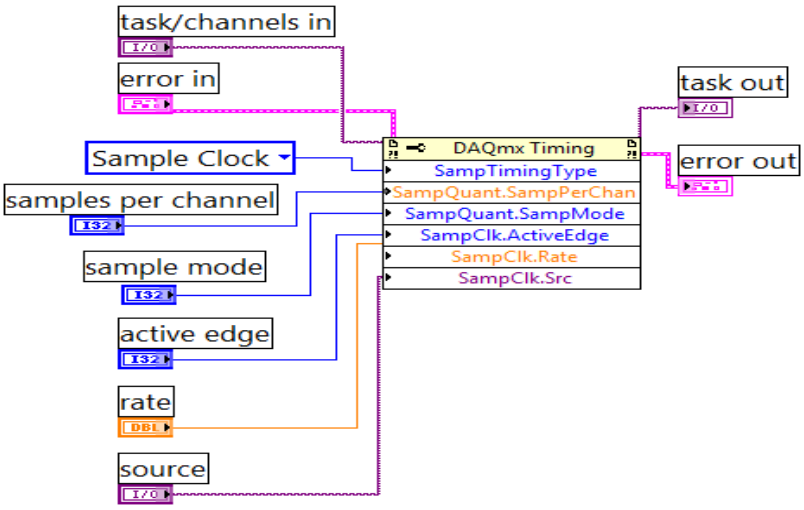

Figure 6-16 DAQmx timing (sample clock)

6.6 FM demodulation

The DAQmx function is used to read multiple samples from multiple channels, e.g. the four inputs AI0, AI1, AI2, and AI3 at the receiver stage for each PCI-6110, see Figure 6.17. For demodulated FM the downconverts function as shown in Figure 6.18, was designed to downconvert the real passband signal data of a user specified bandwidth. The baseband IQ signal (complex envelop) is returned in the downconverted waveform output. When the enable filter parameter is TRUE, the downconverted IQ signal is filtered by a software lowpass FIR filter whose design parameters were dictated by the following considerations:

- If the carrier frequency is greater than passband bandwidth, the filter stopband begins at the carrier frequency.
- If the carrier frequency is less than the passband, then the filter stopband begins between carrier frequency and 2×carrier frequency – passband bandwidth/2.

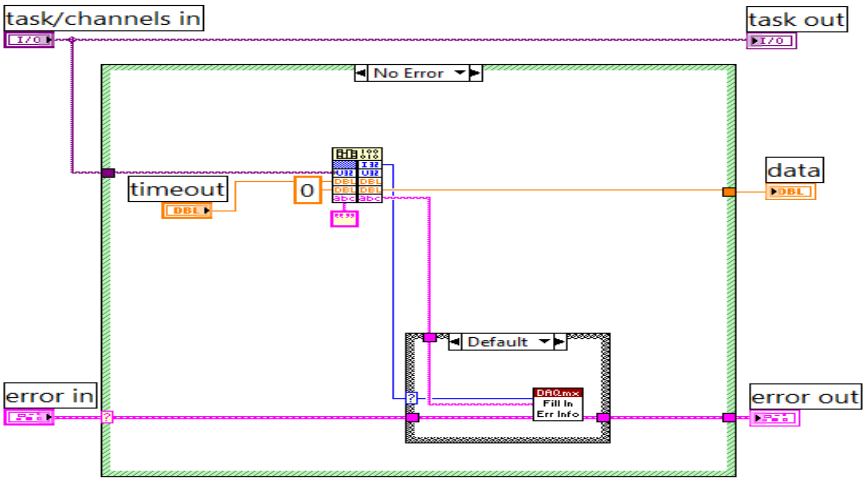

Figure 6-17 DAQmx read

In the downconvert function the waveform inputs the signal for downconversion in passband form and contains the following elements:

- **t0:** trigger (start) time of the acquired signal.
- **dt:** time interval between data points in the acquired signal.
- **y:** complex array representing the signal for downconversion.

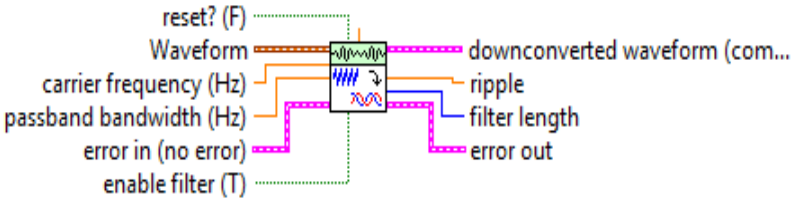

Figure 6-18 Downconvert passband

The carrier frequency (25kHz) is the centre of the passband, this frequency is downconversion to 0Hz (DC), and in this case should be the centre of the expected carrier frequency of the incoming signal for downconversion. The passband bandwidth (1500Hz) specifies the bandwidth of the passband signal data, this parameter is ignored if the reset input is FALSE.

The downconversion waveform (output of downconversion function) contains the downconversion signal in complex envelope format which contains the following arrays:

- **t0:** trigger (start) time of the acquired signal.
- **dt:** time interval between data points in the acquired signal.
- **y:** complex-valued time domain data array. The real and imaginary parts of this complex data array correspond to the in-phase (I) and quadrature-phase (Q) data, respectively.

The downconversion waveform is connected to the demodulate FM function which performs frequency demodulation on the incoming IQ signal. The recovered information signal is returned in the FM demodulated waveform output. The information signal is computed as a result of a demodulation process, which takes place in two steps internally, first the incoming IQ data is phase-demodulated, and then the result of this phase demodulation is differentiated using a software FIR with three tops.

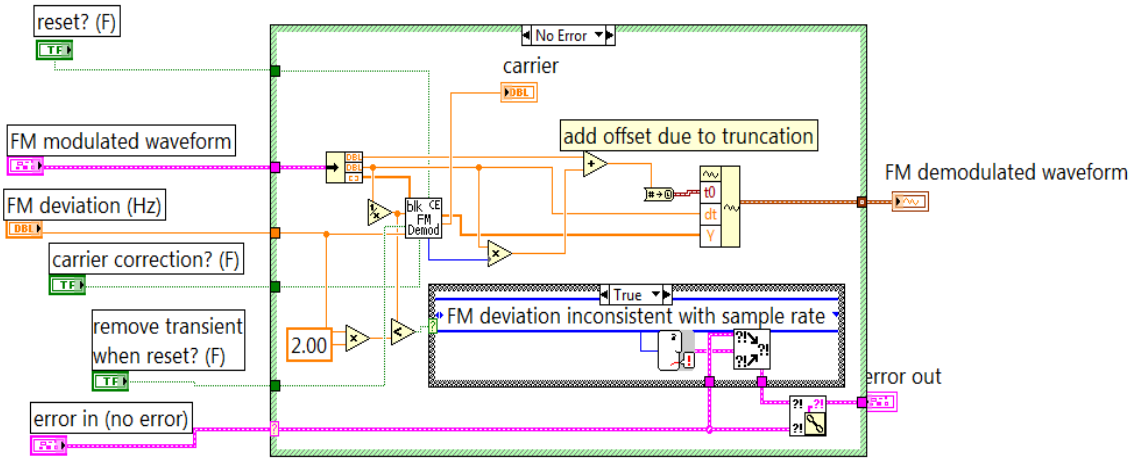

Figure 6-19 Demodulated FM

The demodulation device shown in Figure 6.19, calculates any residual frequency left in the IQ data (complex) input. The demodulate FM function used with NI hardware and the residual frequency is the offset from the expected carrier frequency specified in the MT

configure downconversion setting. If the actual carrier frequency of the acquired signal is different from the centre frequency of the receiver, a DC offset is introduced into the output FM demodulated waveform. If the carrier correction parameter is set to TRUE, this offset is removed. The correction is a software correction only.

In Figure 6.20 the FM modulated waveform inputs baseband (downconverted) time-domain data for demodulation which contains the following arrays:

- **t0:** specifies the trigger (start) time of the acquired signal.
- **dt:** specifies the time interval between data points in the acquired signal.
- **y:** complex-valued time domain data array. The real and imaginary parts of this complex data array correspond to the in-phase (I) and quadrature-phase (Q) data, respectively.

The FM demodulation waveform consist of two frequencies 100Hz and 1kHz, by using an analogue bandpass filter whose centre frequency was set at 1kHz to recover the 1kHz signal, and set at 100Hz to recover the 100Hz signal.

Calculation of phase difference

The LABVIEW software also designed to calculate the phase difference between the two waveform of the same frequency. In Figure 6.20 the two signal inputs (A, B) are received and the device determines whether they are of the same frequency, and if they are, it calculates the phase difference between them. Of course the phase difference is simply the shift occurring in the time the wave takes to travel between each transmitter and receiver.

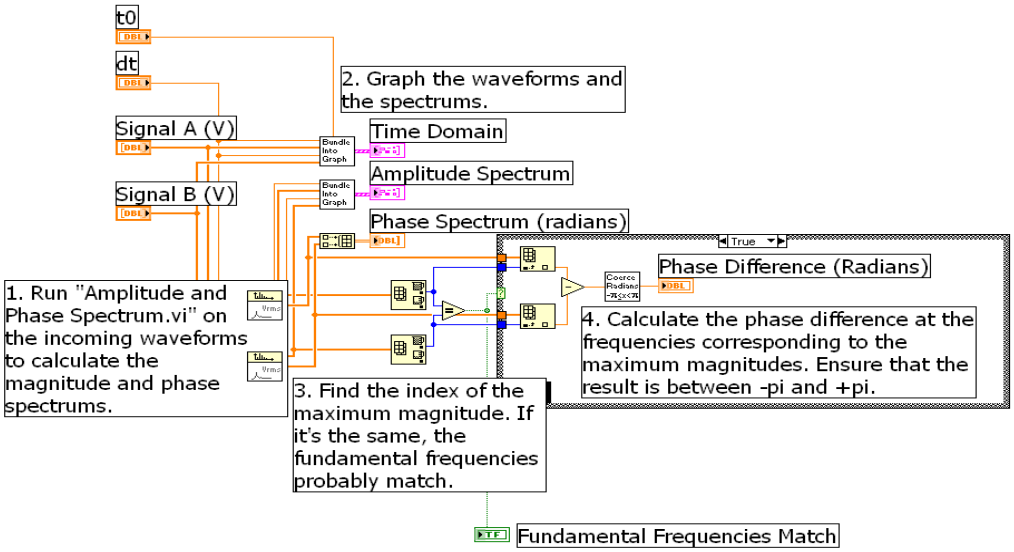

Figure 6-20 Calculation of phase difference

To provide a clearer view of how the signals are modulated and demodulated Figure 6.21 shows all the stages. The first sequence measures the phase differences for the 100Hz and 1kHz signals, and the second sequence measures the phase difference for 25kHz carrier frequency.

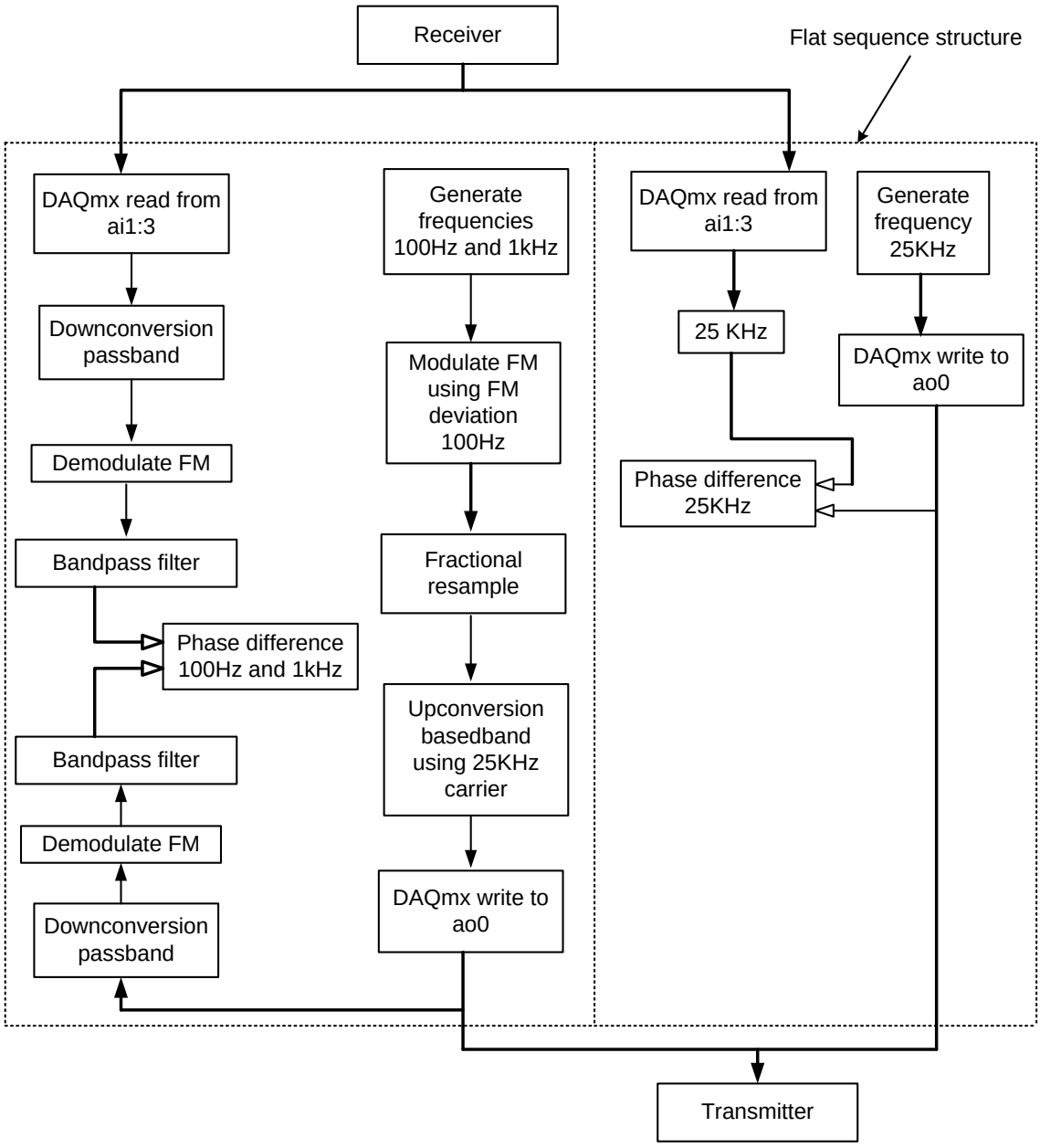

Figure 6-21 Block diagram for modulation and demodulation of the ultrasonic signals

6.7 Summary

This chapter has described the hardware and software implementation of the new 3D measurement system. The hardware of the new 3D measurement system includes three integrated transmitters, five receivers and a multifunctional PCI interface card. The hardware has responsibilities of two-mode ultrasound transmitting, ultrasound receiving and data communication with the computer. The software has the responsibilities for generating the carrier signal, modulating and demodulating the signal, processing the data and displaying the results. The experimental testing of this prototype will be described in the next chapter.

Chapter 7 Enhancement of the measurement system

7.1 Introduction

The new 3D measurement system achieved considerable improvements in measurement accuracy, resolution and system flexibility, which takes the system one step closer to industrial application. However, if the system were to be applied in a complex industrial environment, much stronger external disturbances are to be expected, which could significantly reduce the system's performance. Therefore, in this chapter, the effect of the environment on system measurement will be studied, with emphasis on two major environmental effects: interference caused by ultrasound echoes/reflections and changes in the condition of the air. For each of these problems, a technique has been developed, and the experimental tests will be introduced in this chapter.

7.2 Eliminating distortions in frequency measurement

Besides drift in the speed of the ultrasound wave due to changes in air temperature and humidity in the workspace, ultrasound echo interference is a second major error source in the new 3D measurement system, causing significant distortion in the measurement of the phase of the received ultrasound signal. Therefore, in this section, a frequency measurement technique will be introduced that eliminate these frequency distortions by employing Short-Time-Fourier-Transform (STFT). The frequency is measured by applying bandpass filter, see figure 7.1.

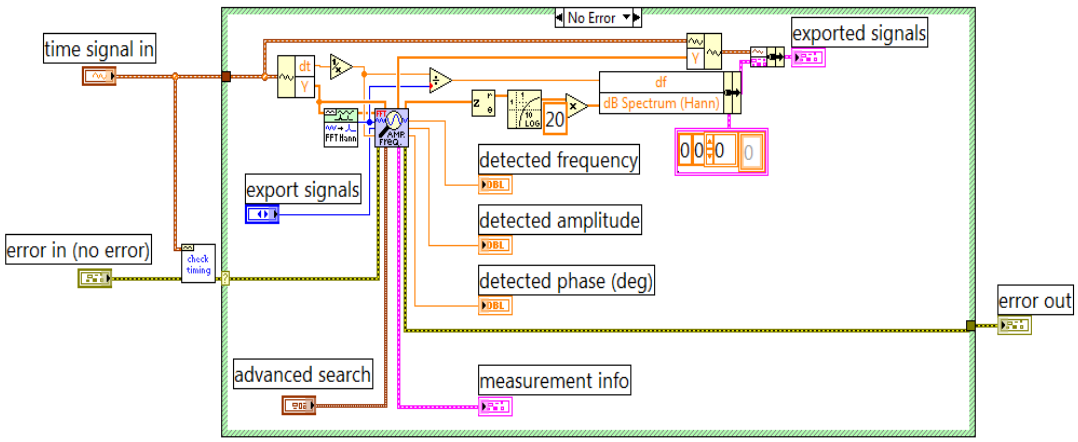

Figure 7-1 Frequency measurement

Figure 7.2 shows the first 1200 measurements of frequency obtained in an experiment where the frequencies f_1 and f_2 were transmitted by FM modulation and f_3 transmitted directly to receiver. In plots (a) and (b) of Figure 7.2 the effect of ultrasound echoes on measure frequencies of the 100Hz and 1kHz signals are seen to very small In plot (c) of figure 7.2, however, the ultrasound echoes, result in significant frequency distortions in the measurement of the frequency of the 25kHz signal.

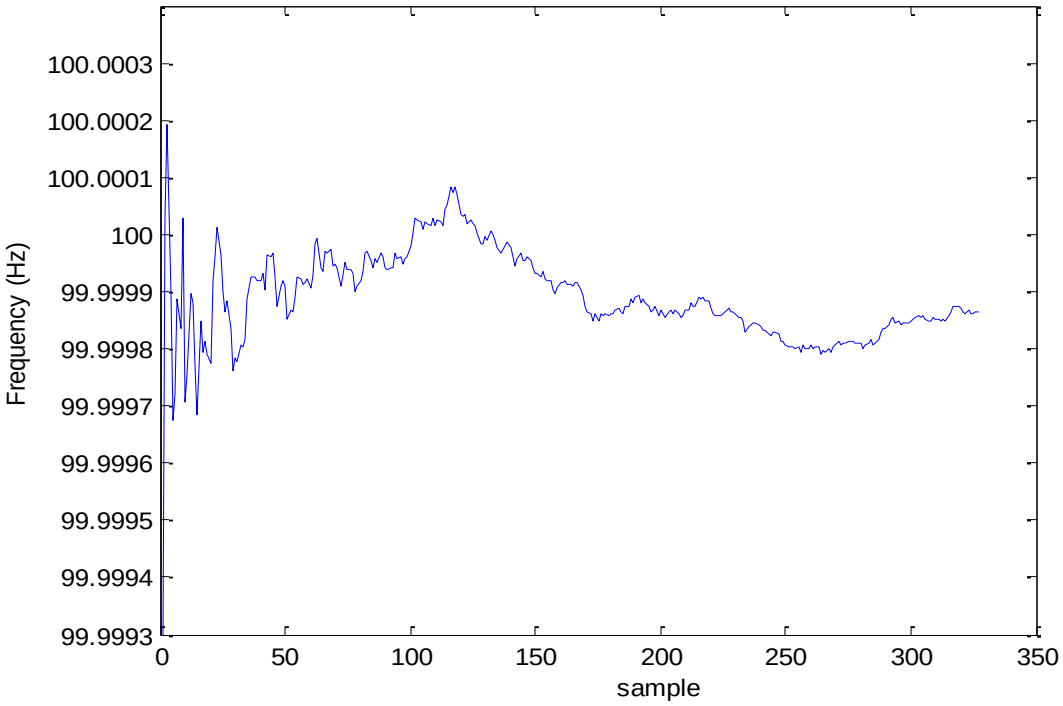
Frequency (Hz)
100.0003
100.0002
100.0001
100
99.9999
99.9998
99.9997
99.9996
99.9995
99.9994
99.9993
0
50
100
150
200
250
300
350
sample

(a)

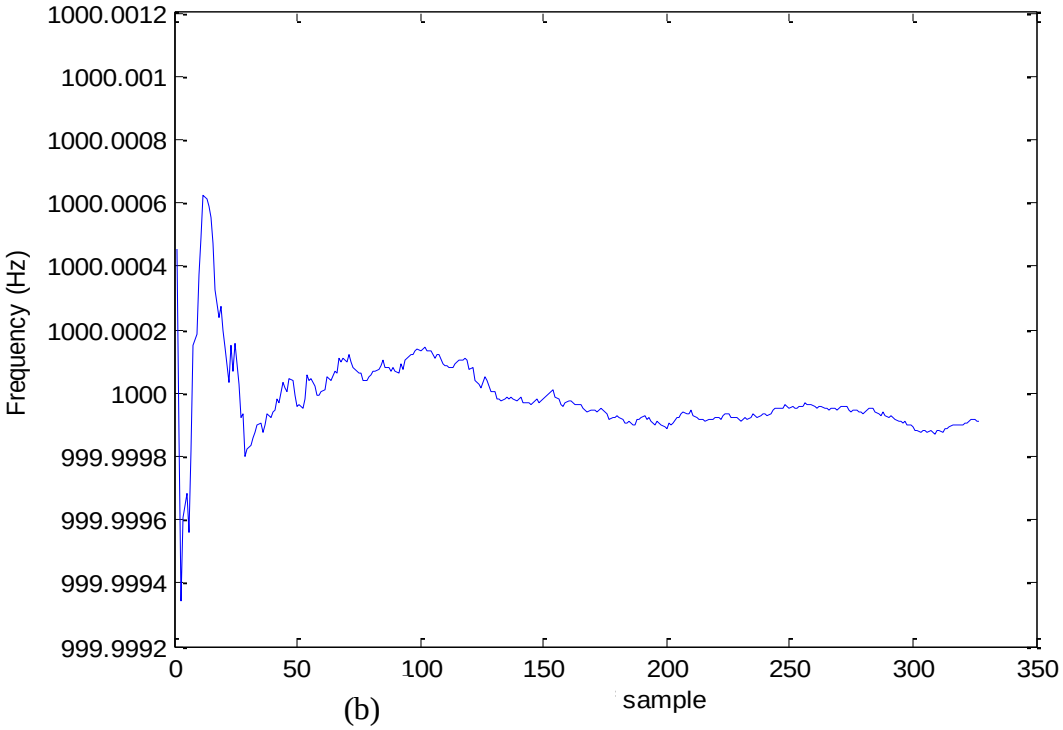
Frequency (Hz)
1000.0012
1000.001
1000.0008
1000.0006
1000.0004
1000.0002
1000
999.9998
999.9996
999.9994
999.9992
0
50
100
150
200
250
300
350
sample

(b)

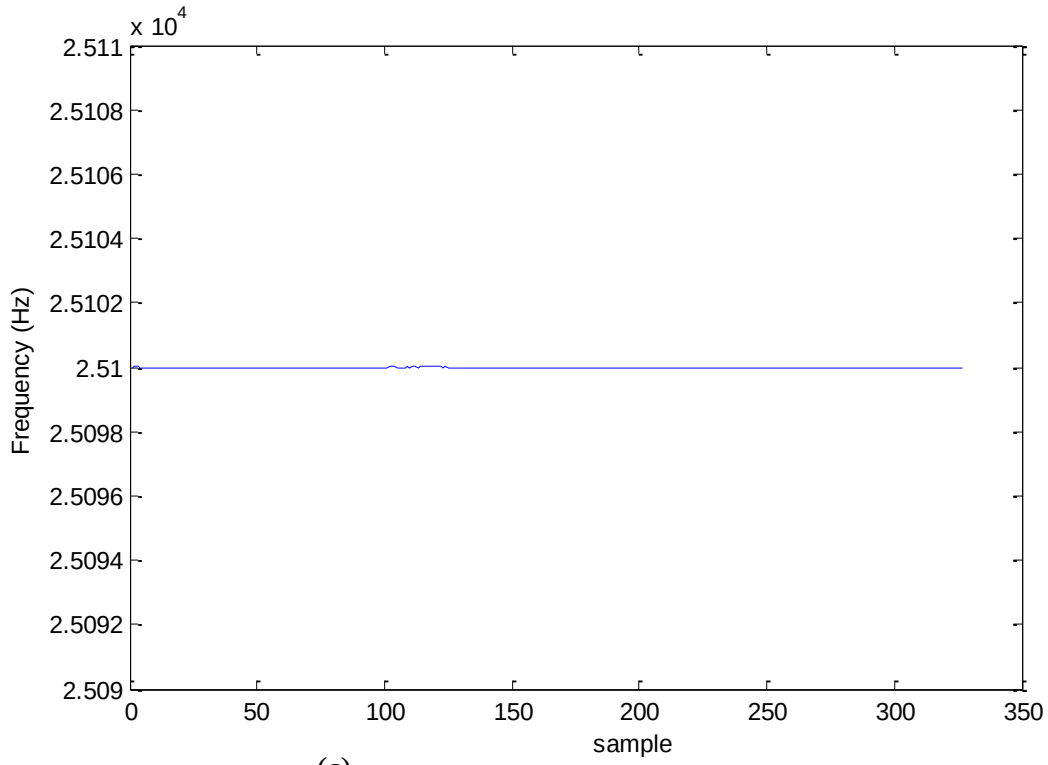

(c)

Figure 7-2 Measured frequencies using MFCWFM technique with obstacles in workspace

(a) 100Hz signal

(b) 1kHz signal and

(c) 25kHz signal

To overcome these problems, and eliminate the distortions in the frequency measurements, a different frequency measurement technique was used [55, 56]. This technique is capable of distinguishing the 25kHz frequency of the main signal from the echoes and reduces the error due to standing wave effects on the 100Hz and 1kHz signals.

7.2.1 Modelling of the ultrasound transmitter-receiver signal

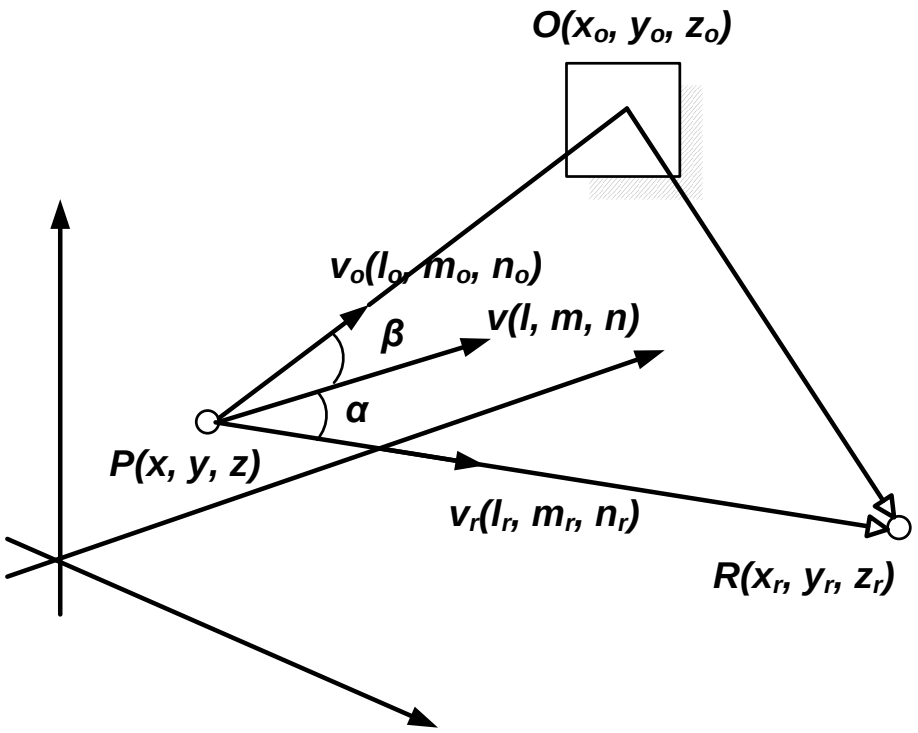

Figure 7-3 Illustration of signal paths used for the mathematical model

Considering the case illustrated in the above figure, the transmitter at $P(x, y, z)$ is moving at speed $v(l, m, n)$. Some of the ultrasound energy radiates from the transmitter directly to the receiver $R(x_r, y_r, z_r)$, and carries information on the v's subsector $v_r(l_r, m_r, n_r)$, which has the following expression [47]:

$$|v_r| = |v|.\cos\alpha \qquad 7\text{-}1$$

Where, α is the inclination between v and v_r, which is on the vector $\overline{PR}$ $(x_r\text{-}x, y_r\text{-}y, z_r\text{-}z)$, therefore, the $cos\alpha$ can be evaluated by the following equation:

$$\cos\alpha = \frac{\left|l(x_r - x) + m(y_r - y) + n(z_r - z)\right|}{\sqrt{l^2 + m^2 + n^2}.\sqrt{(x_r - x)^2 + (y_r - y)^2 + (z_r - z)^2}}$$

$$\cos\alpha = \frac{\left|l(x_r - x) + m(y_r - y) + n(z_r - z)\right|}{|v|.\sqrt{(x_r - x)^2 + (y_r - y)^2 + (z_r - z)^2}} \qquad 7\text{-}2$$

Cross multiplying and substituting Equation (7-1) into Equation (7-2), yields:

$$|v_r| = \frac{\left|l(x_r - x) + m(y_r - y) + n(z_r - z)\right|}{.\sqrt{(x_r - x)^2 + (y_r - y)^2 + (z_r - z)^2}} \qquad 7\text{-}3$$

The subsector v_r is frequency modulated to the ultrasound wave (y_{direct}) that is transmitted to the receiver:

$$y_{direct} = \exp\left[j2\pi(1 \pm \frac{|v_r|}{c - |v_r|} ft \right] \qquad 7\text{-}4$$

Where, f is the frequency of the transmitted ultrasound, c denotes the wave speed and the positive sign indicates that the transmitter is moving towards the receiver.

Similarly to Equation (7-3), the portion of the received signal that is reflected by the surface $O(x_o, y_o, z_o)$ can be derived as:

$$y_{echo} = A\exp\left[j2\pi(1 \pm \frac{|v_o|}{c - |v_o|} ft \right] \qquad 7\text{-}5$$

Where, v_o is the subsector of the speed v on the direction of $\overline{PO}$ (x_o-x, y_o-y, z_o-z), with the expression:

$$|v_o| = \frac{\left|l(x_o - x) + m(y_o - y) + n(z_o - z)\right|}{.\sqrt{(x_o - x)^2 + (y_o - y)^2 + (z_o - z)^2}}$$

The 'A' in Equation (7-5) represents the attenuation of the echo compared with the un-reflected signal y_{direct}, whose amplitude is assumed to be unity, so A will be a quantity less than 1. As mentioned in the section 3.2.3, assuming spherical radiation, the ultrasound attenuation is proportional to the square of the travelled distance, thus A can be determined as [34]:

$$A = \frac{1}{(D_{echo} - D_{direct})^2} = \frac{1}{(PO + OR - PR)^2} \qquad 7\text{-}6$$

In this case, further attenuation caused by scattering on other reflectors is not considered. The simulation assumes the worst scenario, where the reflector is hard and smooth so there is little or no loss of energy on reflection. The model of the received ultrasound signal can be presented as:

$$y = y_{direct} + \sum_{k=1}^{m} y_{echo,k} \qquad 7\text{-}7$$

$$y = \exp\left[j2\pi(1 \pm \frac{|v_r|}{c - |v_r|}) ft \right] + \sum_{k=1}^{m} A_k \exp\left[j2\pi(1 \pm \frac{|v_{o,k}|}{c - |v_{o,k}|}) ft \right] \qquad 7\text{-}8$$

Where, *m* and *k* denote the number and the index of echoes.

The received signal is shifted down by around 5Hz. The block diagram for this process is shown in Figure 7.4.

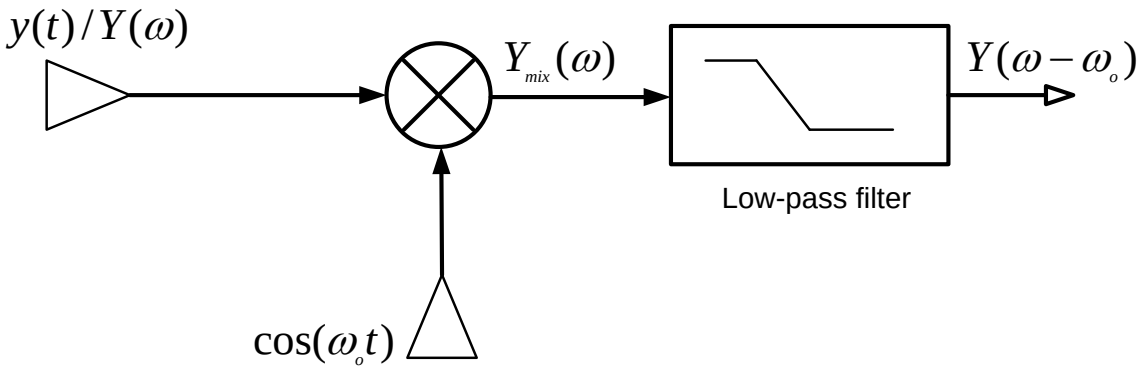

Figure 7-4 Block diagram of the system to shift the frequency of the input signal down by ω_o.

The received signal *Y(t)*, which has the spectrum *Y(ω)*, is multiplied by a signal $cos(\omega_o t)$, where $\omega_o = 2\pi.24995k$ rads/s at the mixer. The Fourier-Transform $Y_{mix}(\omega)$ of the output is then derived as follows:

$$Y_{mix}(t) = Y(t).\cos(\omega_o t)$$

$$= \frac{1}{2}\left[Y(t).\exp(j\omega_o t) + Y(t).\exp(-j\omega_o t)\right] \quad 7\text{-}9$$

According to the shift property of Fourier-transform:

$$Y_{mix}(\omega) = \frac{1}{2}\left[Y(\omega - \omega_o) + Y(\omega + \omega_o)\right] \quad 7\text{-}10$$

Clearly, the signal, $Y_{mix}(\omega)$, contains the up-shifted and down-shifted spectrum of $Y(\omega)$. However, passing the output through a low-pass filter, gives the signal that has the spectrum, $Y(\omega - \omega_o)$, which is around 5Hz.

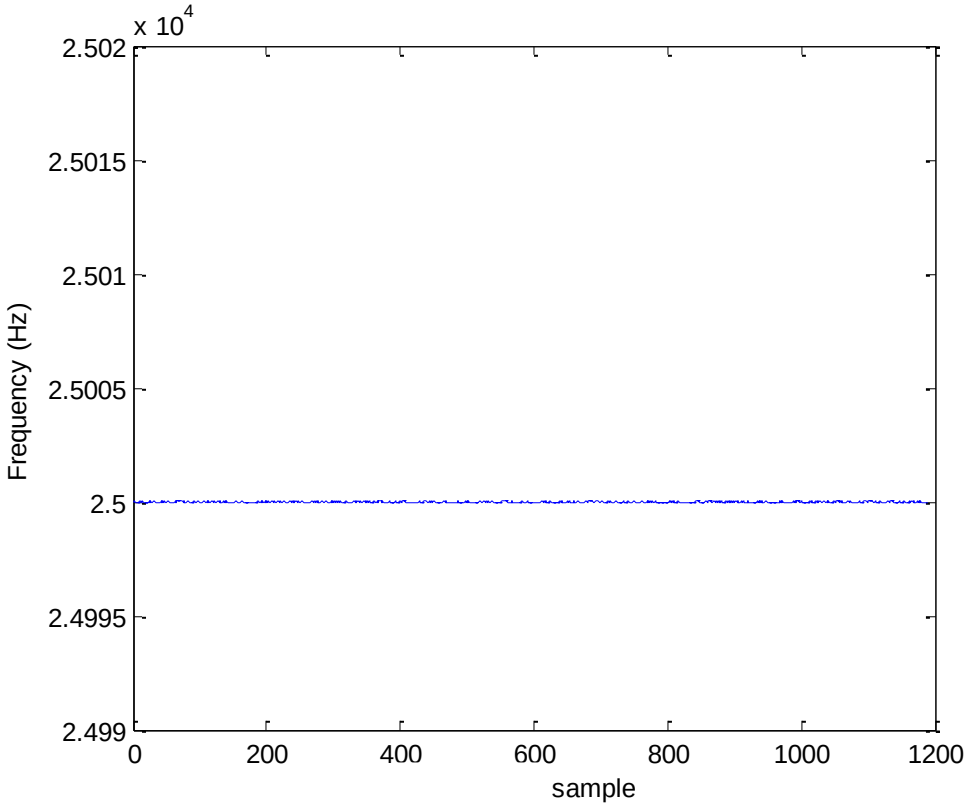

Figure 7-5 Measured frequencies, using 5Hz shift with obstacles in the workspace

The frequency of the received signal, measured directly from receiver, is shown in Figures 7.2(c) and Figure 7.5. In the former case the technique is used with MFCWFM and in the latter case after introducing the 5Hz shift. As can be seen from the values on the Frequency axis, the distortion obtained using 5Hz shift is significantly less than when using MFCWFM.

7.3 Ultrasound speed environment correction

The speed of ultrasound depends on the characteristic properties of air, and slight changes in temperature and humidity can cause significant errors in ultrasonic distance measurements. To evaluate for these ultrasound speed drifts, two systems were set up to measure average temperature and humidity in workspace, see Figure 5.7, and the values obtained were applied to the 1D distance measurement algorithm.

Equation 5-12 gives the speed of sound in air as a function of temperature, and Figure 7.6 shows the same relationship graphically. A change of air temperature by 1°C, for example, from 20 to 21°C increases speed of sound by 0.6m/s. For practical purposes the speed of ultrasound in air may be taken to be directly proportional to the air temperature, see Equation (7.11):

$$c = 331.4 + 0.61.T \qquad 7\text{-}11$$

Where T is the temperature in degrees Celsius.

Equation (5-13) for 1D distance measurement shows that, a change in the speed of sound caused by a change of only 0.5^0C – 0.3 m/s – will result in an error in the 1D distance measurement of 0.347mm. Figure 7.7, shows the possible error in the 1D distance measurement caused by changes in workspace air temperature (see Equation (5.9)).

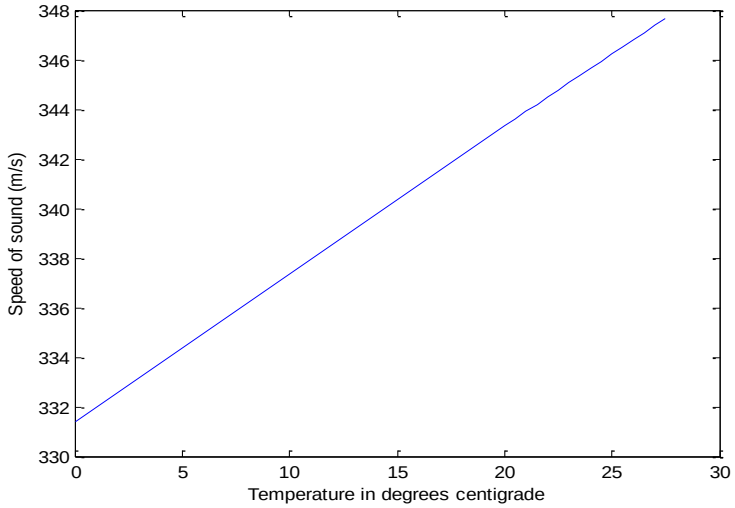

Figure 7-6 Speed of sound as a function of temperature

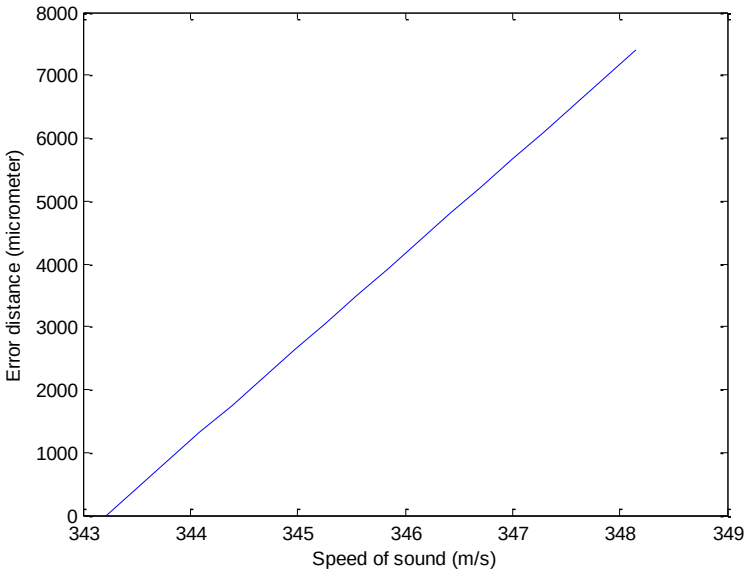

Figure 7-7 Error in 1D distance measurement as a function of the speed of sound

However, changes in humidity also cause changes in the speed of sound that may result in errors in the 1D distance measurement. The effects of changes in humidity are much less than those of temperature (see Equation (5.20)). A change of the relative humidity of 1%, 76% to 77%, will increases speed of sound by 0.01m/s as shown in Figure 7.8, which

will cause an error in the 1D distance measurement (1.2m) of only 14µm, see Figure 7.9 (see section 5.2.3).

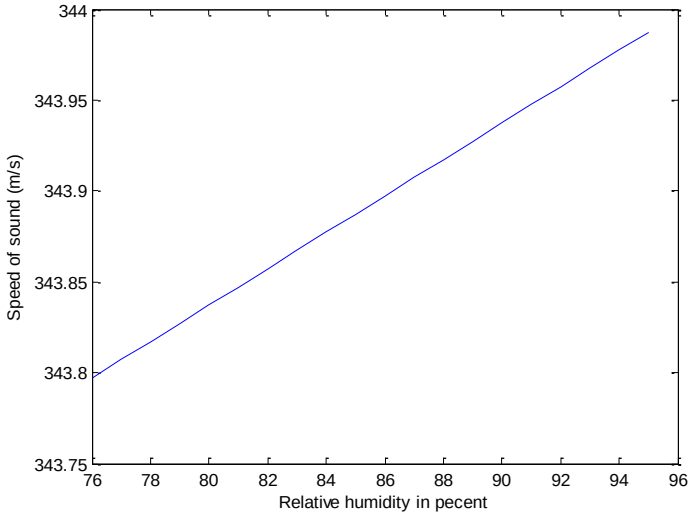

Figure 7-8 Relative humidity versus speed of sound at 20 ^{o}C

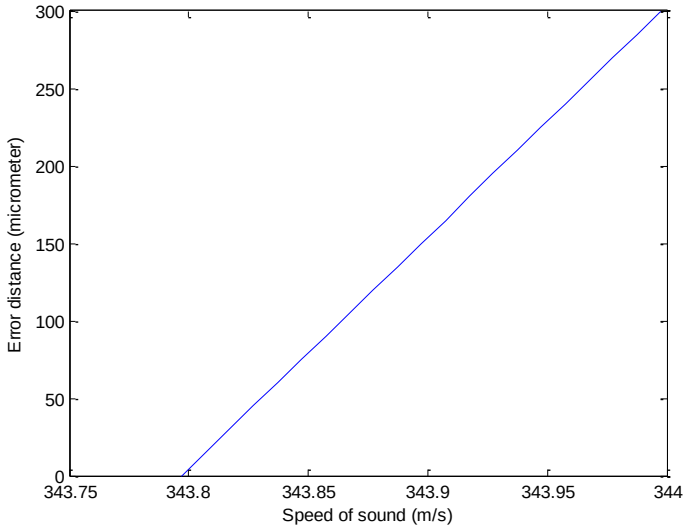

Figure 7-9 Speed of sound versus error in 1D distance measurement

A new technique was introduced in Sections 5.2.2 and 5.2.3 that provided a more effective and economical solution for ultrasound speed evaluation. This new technique is described by the author in [35]. Compared with other current techniques [34, 33], this new technique requires no additional special equipment, and thus reduces the add-on cost to the ultrasonic 3D measurement system.

The technique provides a novel way of viewing and solving the problem of ultrasound speed evaluation, compared with other existing techniques, this technique has advantages of better accuracy, efficiency and does not require extra equipment to monitor the environment. Considering these distinct advantages and the promising results obtained in the simulation, this new technique is recommended for the next generation ultrasound 3D measurement system to provide a full evaluation for a larger workspace.

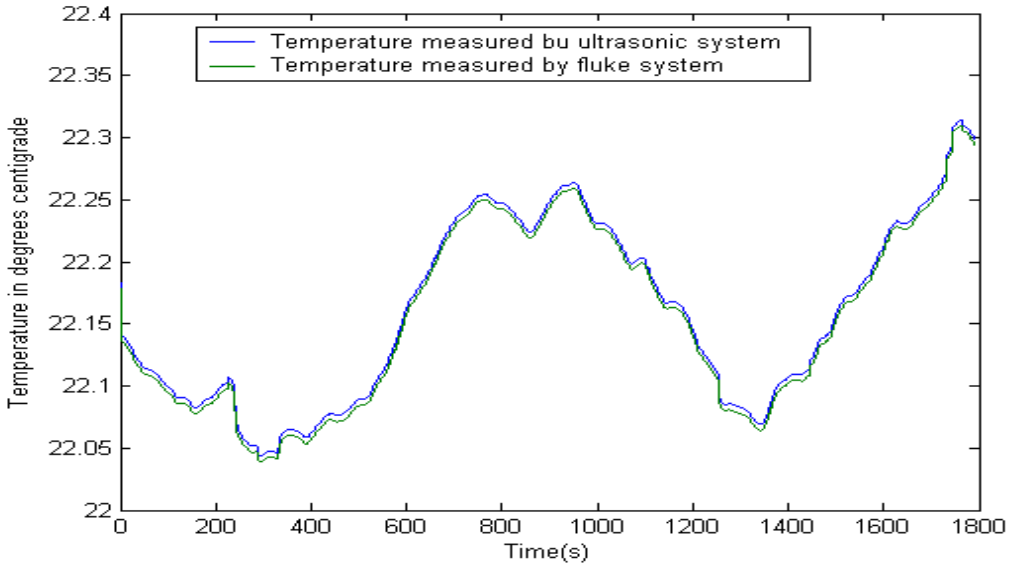

Figure 7-10 Temperature measured by ultrasonic and fluke systems

Figure 7.10 shows experimental result for temperature system. The measured difference between the ultrasonic system and fluke system for measure temperature (accuracy 0.02 ^{0}C) is seen to be about 0.05^{0}C for temperature in the range from 22.05 to 22.3^{0}C. The distance between transducers was 840.230 mm.

The new technique to evaluate temperature and humidity in workspace area was tested and proved in a simulation of 3D position measurement in a virtual environment. Without proper evaluation of the ultrasound speed, inaccurately measured distance may be used, and result in significant errors in the estimated coordinates. In Figure 7.11, the deviations of the estimated coordinates from the real coordinates are shown on the *x*, *y* and *z* axes respectively. The maximum deviation occurred during the measurement on *x*, *y* and *z* axes are 0.52mm, 1mm and 1.2mm respectively.

Figure 7.12, shows the same deviations when the environmental parameters are considered are 1.3×10^{-4}mm, 1.4×10^{-4}mm and 3.0×10^{-4}mm respectively, which are so small that they can be ignored.

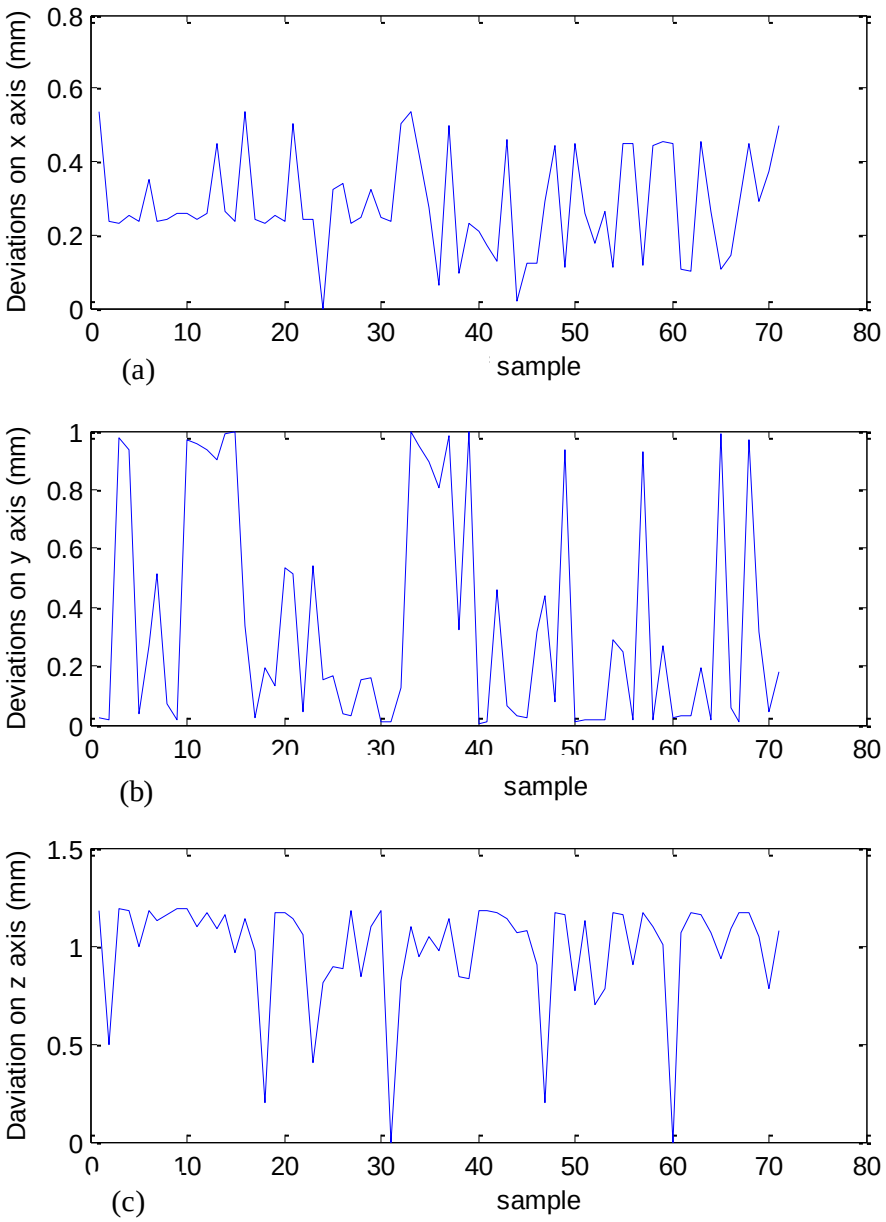

Figure 7-11 Deviations of the estimated coordinates without evaluation

(a) Deviations at x-axis.
(b) Deviations at y-axis.
(c) Deviations at z-axis.

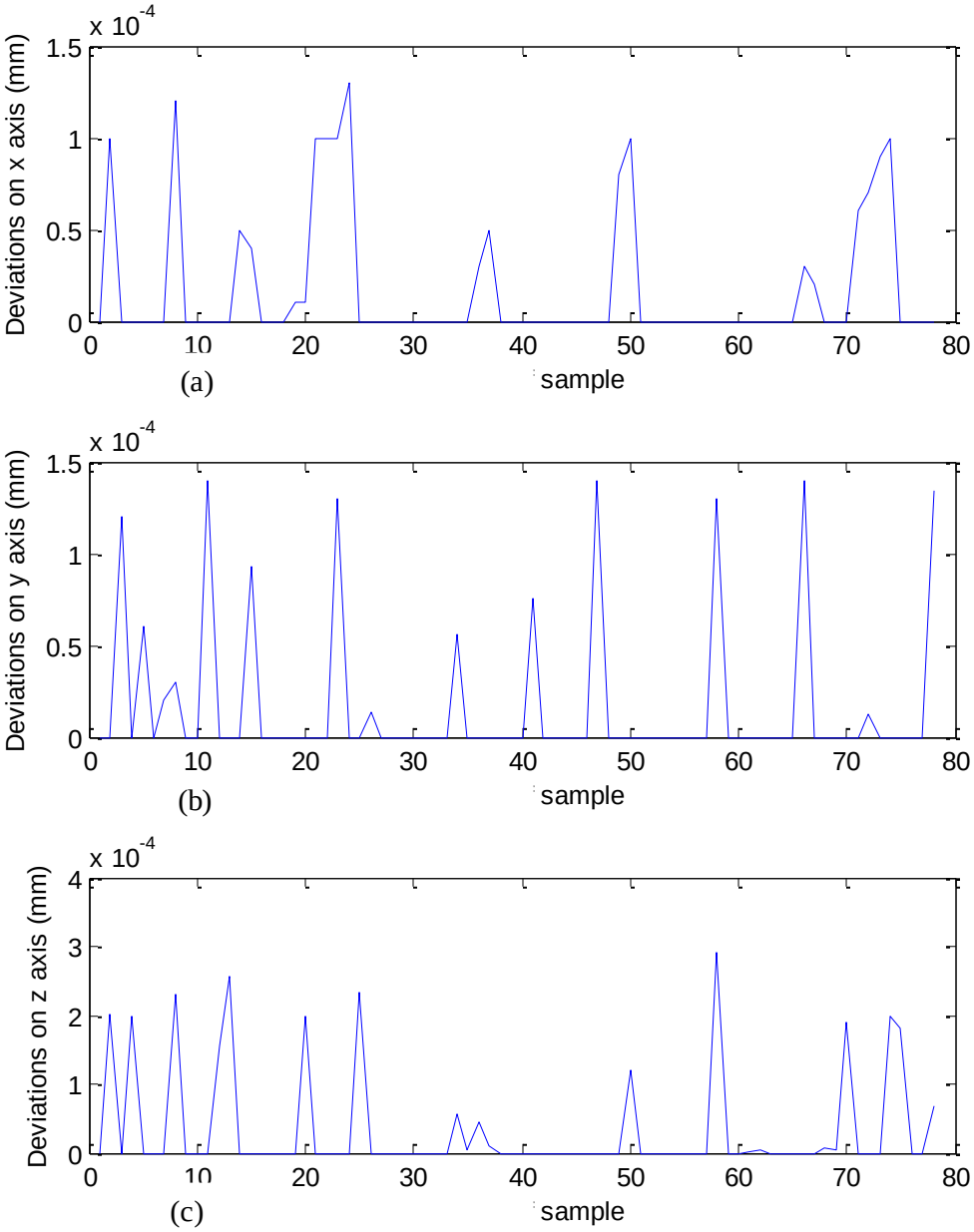

Figure 7-12 Deviations of the estimated coordinates with evaluation

(a) Deviations at x-axis.
(b) Deviations at y-axis.
(c) Deviations at z-axis.

7.4 Summary

In this chapter, major external disturbances to the proposed 3D measurement system, ultrasound speed drift and echo inference, were studied, and methods of overcoming these disturbances introduced.

With the use of the MFCWFM system for distance measurement, the disturbances caused by ultrasound echoes became more significant. During the movement of the transmitter, echoes interfere with the main signal and cause significant distortion of the measured, which means that the traditional frequency measurement technique cannot be used. Therefore, a frequency measurement technique was introduced in this chapter. This technique uses to distinguish the echoes from the main signal.

Ultrasound speed drift is caused by the changes of the condition of the air within the workspace. Without proper evaluation of temperature and humidity, a wrong estimate of the ultrasound speed could cause significant errors in distance measurement, resulting in deviations in the measured coordinates of the transmitter position. To overcome this problem, this chapter tested a novel method, which uses two ultrasound measurement systems for temperature and humidity measurements in the workspace. The use of this method allows a more accurate measurement of position coordinates.

A new technique was developed and tested in a simulation environment with LABVIEW.

Chapter 8 Experimental validation tests of the prototype measurement system

8.1 Introduction

Previous chapters introduced the working principles and hardware/software implementation of the new 3D measurement system, and described how it evaluated the speed of sound in workspace. This chapter reports the experimental testing of the new 3D measurement system.

As described earlier, the new 3D measurement system involves a MFCWFM system for fixed and dynamic distance measurement. This has been experimentally tested, including measurement of the translational movement of a transmitter in 3D space, and its benefits clearly demonstrated. To accomplish the measurements, the system needed to pass through the two phases of: system setup, and 3D measurement. This chapter will present the practical details of these stages together with the corresponding experimental results. The new 3D measurement system was tested on a Zeiss Coordinate Measurement Machine (CMM) and GEISS 5-axis CNC machine and compares the results with Renishaw XL-80 and laser tracer system (eTALON) to validate the accuracy of the system.

8.2 Ultrasound system setup on Zeiss CMM

To validate the accuracy of the ultrasound system, the first test was on a Zeiss CMM as shown on Figure 8.1 in a ±2 ^{o}C temperature controlled environment. The stated accuracy of this CMM is 2μm in the volume, which makes it an ideal reference for this testing.

As introduced earlier in Chapter 5, before starting the measurement, one procedure has to be followed, is called *System Setup*.

System Setup locates the receivers at convenient positions on Zeiss CMM, whose co-ordinate frame is co-incident with the CMM co-cordinate frame.

Figure 8-1 Ultrasound sound system on CMM

8.2.1 System setup-Positioning of the receivers

This section presents the practical implementation of the receiver positioning method introduced in Section 5.4, to evaluate the coordinates of the three receivers used in this experiment. The arrangement of the experiment including the three receivers is illustrated in Figure 8.2.

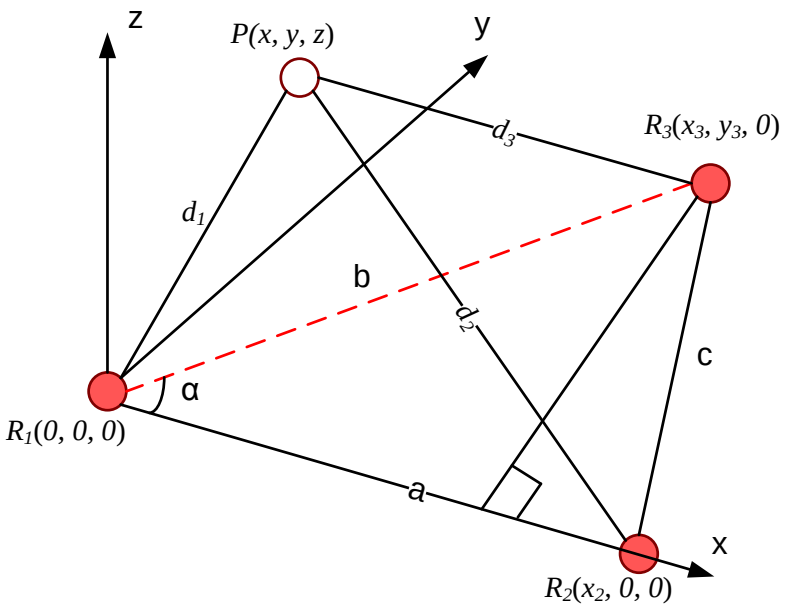

Figure 8-2 Arrangement of the receivers

The coordinates of the three receivers are established using the following setup procedure:

- Set the coordinates of the Receiver1 as (0, 0, 0)

- Determine the distance between the Receiver1 and Receiver2, noted as *a*, so that coordinates of Receiver2 can be established as (*a*, 0, 0). Here, Receiver2 is configured as a transmitter by switching its transducer to the transmitter driver. The measured result for *a* was 902.121mm, thus the coordinates of the Receiver2 were determined as (902.121, 0, 0).

- Measure the distances (*b*, *c)* from Receiver3 to Receiver1 and 2 respectively, by configuring Receiver3 as the transmitter. The measurement results of *b* and *c* are 1192.608mm and 785.794mm respectively. Substitute these values and *a* (as determined earlier) into Equations (5-28) and (5-29):

$$x_3 = \frac{a^2 + b^2 - c^2}{2a}$$

$$y_3 = \sqrt{b^2 - x_3^2}$$

The coordinates of the Receiver3 were established as (897.143, 785.794, 0).

8.2.2 Calibration of the transducers

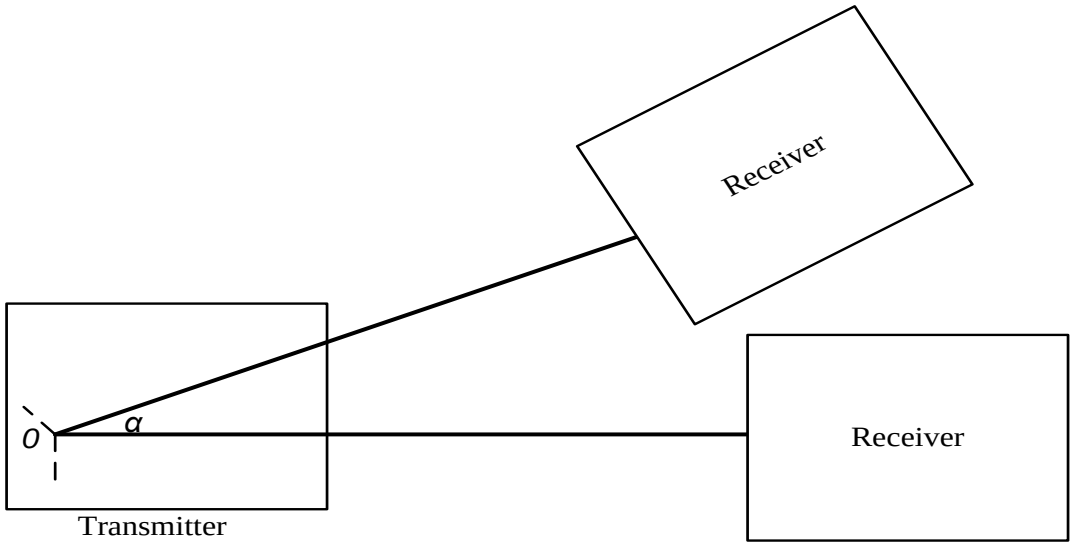

Figure 8-3 Transducer positioning

The above figure shows the transducer positions used for all receivers and transmitters. During the measurement, the position of transmitter and receiver are assumed to have the coordinate centre, *O*. Therefore, to obtain the real distances between the transmitter and the receiver, the transducers should be calibrated. The Zeiss CMM was used to calibrate all transducers by using its inherent positioning accuracy.

In addition to calibration of the transducers there is another test which shows to effect of moving transmitter with difference angle α on measure distance and then measure position as shown in Figure 8.4. The maximum deviation is 9μm.

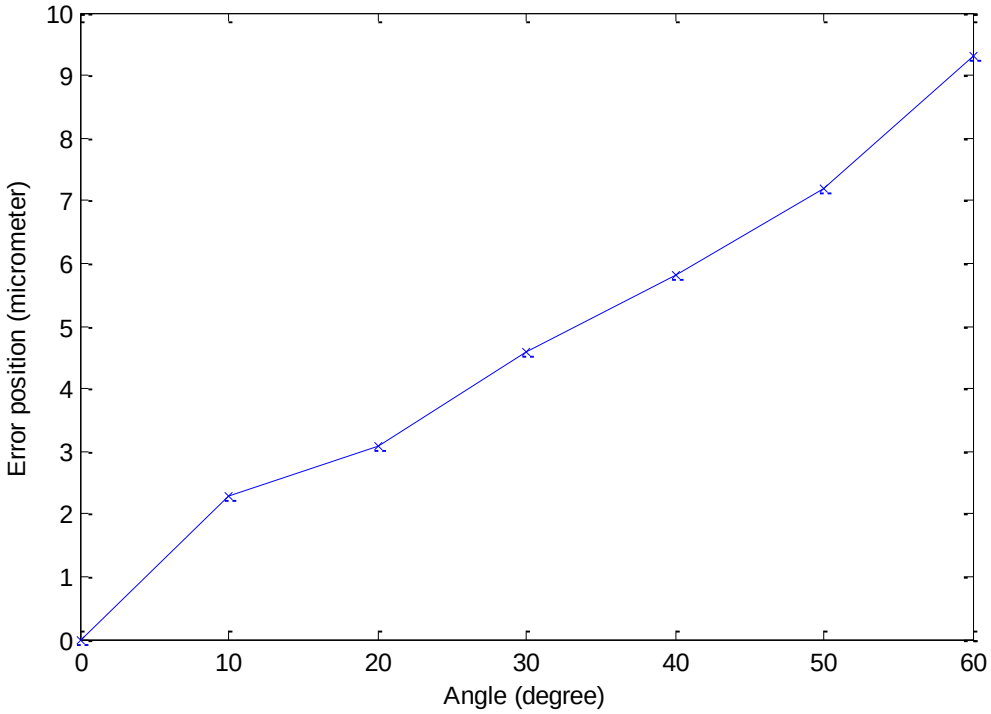

Figure 8-4 The effect of moving transmitter with angle α to measure position

Once the instantaneous distances have been determined, they and the pre-determined receivers coordinates are substituted into Equation (5-23). The corresponding 3D position of the transmitter can then be evaluated from:

$$x' = \frac{x_2'^2 + d_1^2 - d_2^2}{2x_2'}$$

$$y' = \frac{y_3'^2 + d_1^2 - d_3^2 + x_3'^2 - 2x'x_3'}{2y_3'} \quad , \quad z' = \sqrt{d_1^2 - x'^2 - y'^2}$$

$$\begin{bmatrix} x \\ y \\ z \\ 1 \end{bmatrix} = \left[Rot(x,\theta).Rot(y,\beta).Rot(z,\alpha).Tran(x_1, y_1, z_1) \right]^{-1}.\begin{bmatrix} x' \\ y' \\ z' \\ 1 \end{bmatrix}$$

Where, (x, y, z) is the coordinates of the transmitter, d_i is the distance to the *ith* receiver and (x_i, y_i, z_i) is the coordinates of the *ith* receiver. The difference between ultrasound

system and CMM for measured position with moving the x-axis in increments of 20mm is shown in the following figure.

Figure 8.5 shows the measured errors on each axis to have maximum values of 0.022mm, 0.019mm and 0.024mm, which can be regarded as the accuracy of the measurement in *x*, *y*, and *z* axis respectively.

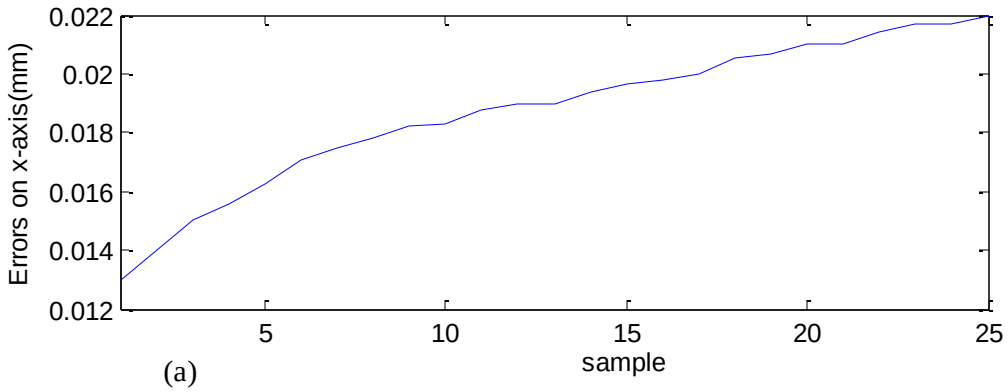

(a)

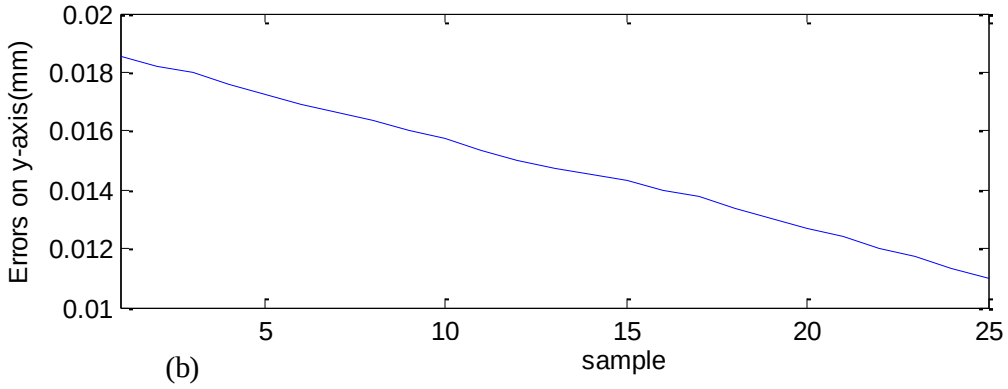

(b)

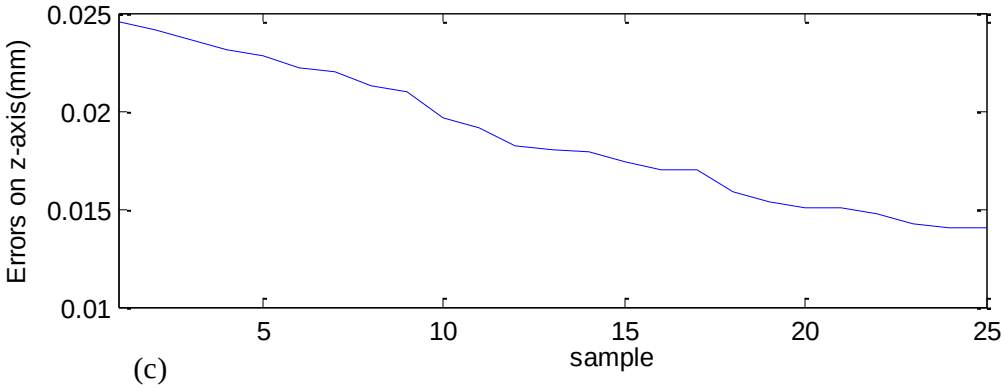

(c)

Figure 8-5 Difference between ultrasound system and CMM

(a) Measured errors on x-axis
(b) Measured errors on y-axis
(c) Measured errors on z-axis

8.3 Ultrasound system setup on GEISS 5-axis milling machine-CO-axial test

The second test was on a GEISS machine as shown in Figure 8.6 but in a normal workshop environment. The transmitter was mounted on the spindle. By using the software of the GEISS machine to move the transmitter into a zero position (0, 0, 0) and consider this zero position for both ultrasound system and GEISS work piece offset (G54).

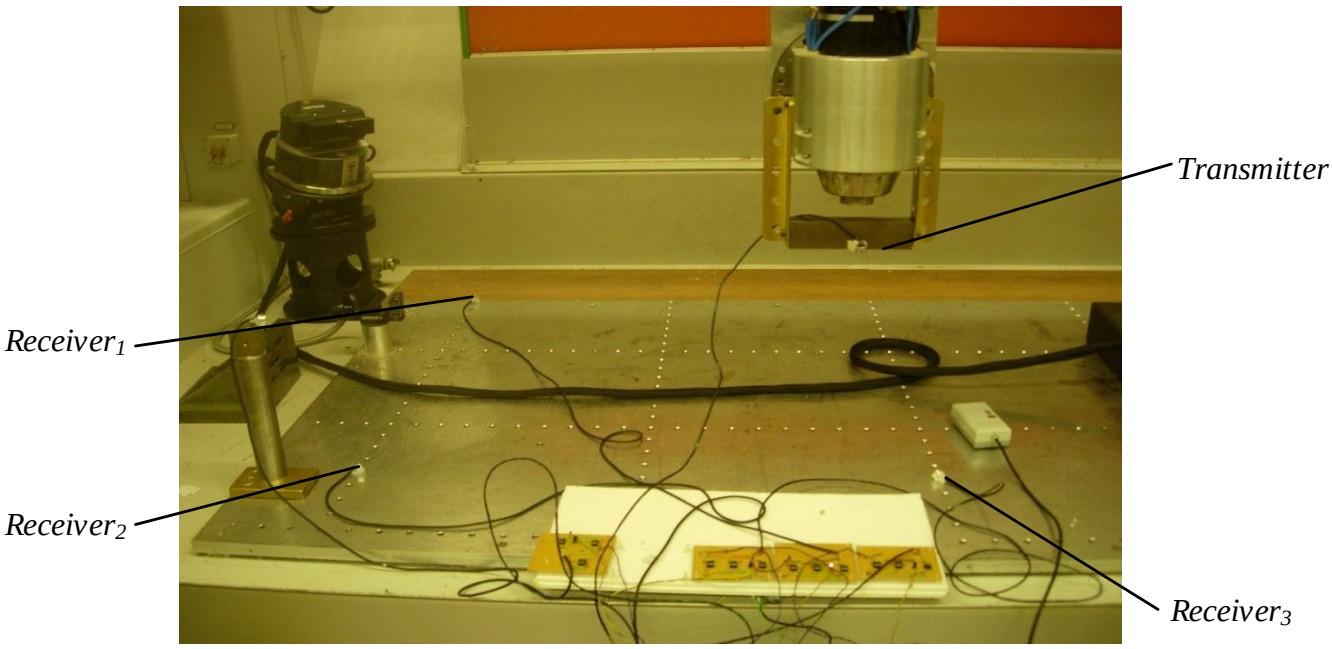

Figure 8-6 Arrangement of the receivers on GEISS machine

First the receiver's positions are established in the local frame. Then by using the control of the machine the transmitter (position) is moved on the x axis from 0 to 760mm in 40mm increments, at every point.

The next step is to transfer the data measured by ultrasound system to machine coordinates. This is achieved by calculating angles α, β and θ to determine the corresponding axis. Angles and x, y, z for measured positions are used in Equation 5.24, to calculate the new coordinates.

$$\begin{bmatrix} x \\ y \\ z \\ 1 \end{bmatrix} = \begin{bmatrix} \cos\beta\cos\alpha & -\sin\theta\sin\beta\cos\alpha - \cos\theta\sin\alpha & -\cos\theta\sin\beta\cos\alpha + \sin\theta\sin\alpha & x_1 \\ \cos\beta\sin\alpha & -\sin\theta\sin\beta\sin\alpha + \cos\theta\cos\alpha & -\cos\theta\sin\beta\sin\alpha - \sin\theta\cos\alpha & y_1 \\ \sin\beta & \sin\theta\cos\beta & \cos\theta\cos\beta & z_1 \\ 0 & 0 & 0 & 1 \end{bmatrix} \cdot \begin{bmatrix} x' \\ y' \\ z' \\ 1 \end{bmatrix}$$

The measured *x*, *y* and *z* from the ultrasound system was then compared with that measured by XL-80 (accuracy about 2μm) as shown in Figure 8.7. The same procedure was repeated on *y* and *z* axis, but on *z* axis moved from 0 to 500mm.

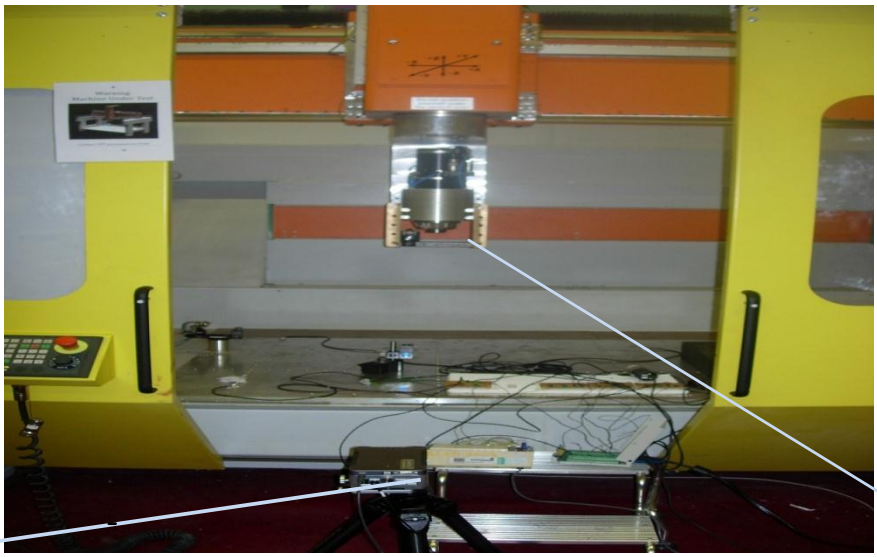

Figure 8-7 Renishaw XL-80 applied on GEISS machine

Figure 8.8 shows that the error position measured by ultrasound system and XL-80 system for each axis, and this figure shows the sensitivity of ultrasound system in measuring the geometric error of the machine moving on each axis. As can be seen, the maximum difference is 38μm.

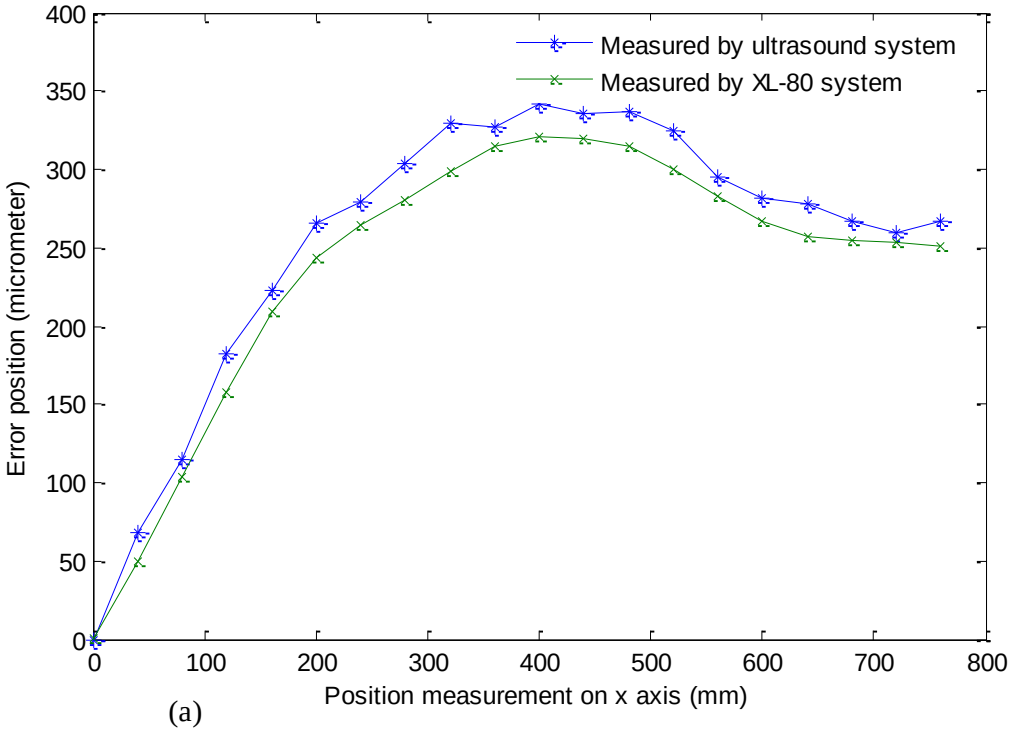
Measured by ultrasound system
Measured by XL-80 system
Error position (micrometer)
Position measurement on x axis (mm)
0
50
100
150
200
250
300
350
400
0
100
200
300
400
500
600
700
800

(a)

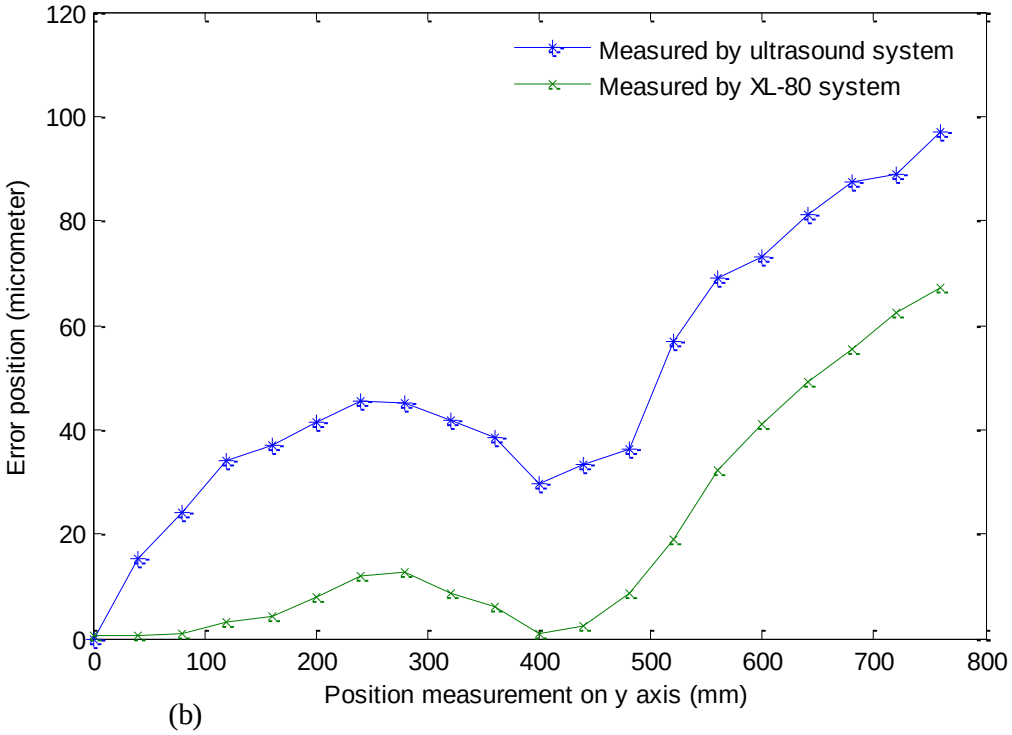
Measured by ultrasound system
Measured by XL-80 system
Error position (micrometer)
Position measurement on y axis (mm)
0
20
40
60
80
100
120
0
100
200
300
400
500
600
700
800

(b)

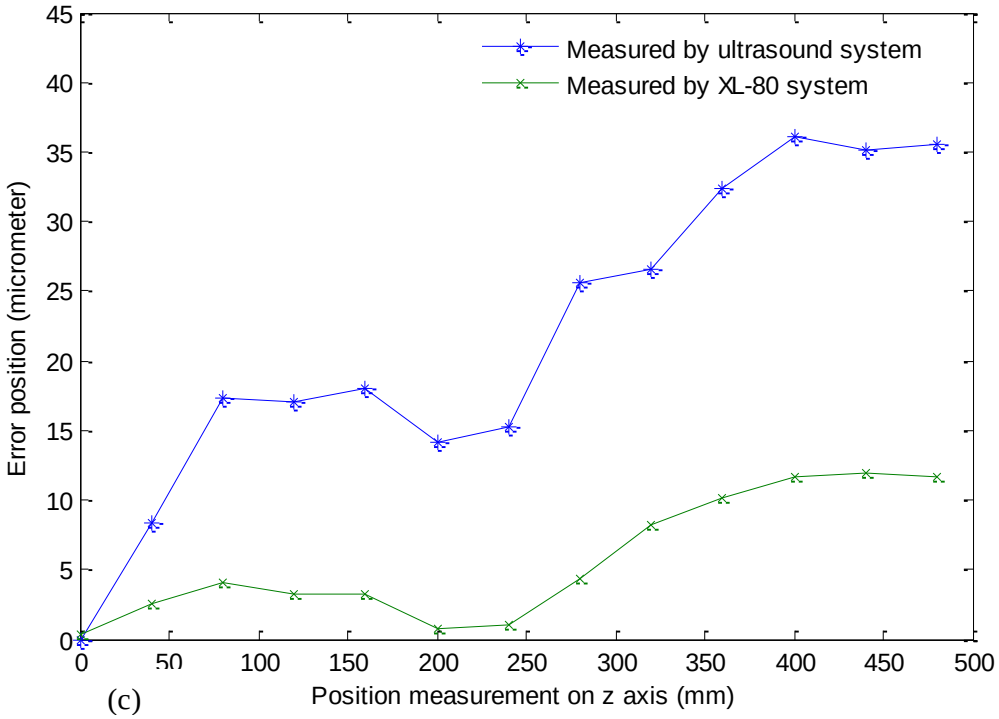

(c)

Figure 8-8 The error measured by the ultrasound system and XL-80 system from GEISS Machine

(a) Measured errors on x-axis
(b) Measured errors on y-axis
(c) Measured errors on z-axis

In Figure 8.9 the difference between ultrasound system and XL-80 system to measure the error position on GEISS machine. The difference between them on x axis was 30μm and on y axis was 38μm, however the error on z axis was 25μm.

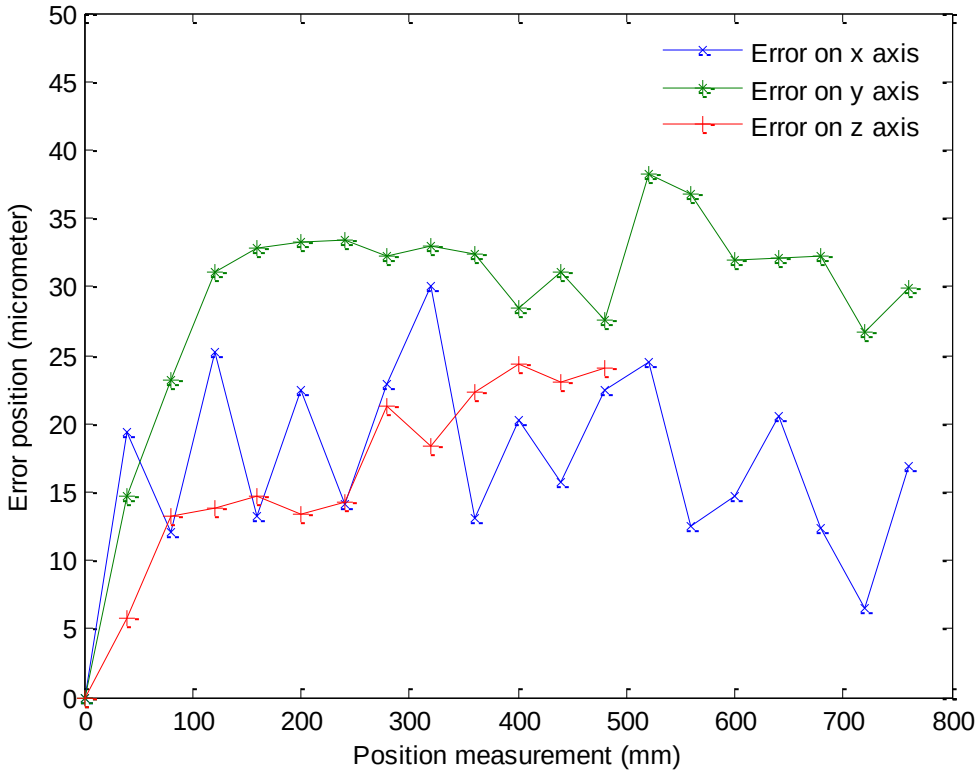

Figure 8-9 The difference between the ultrasound system and XL-80 system to measure the error on GEISS machine.

8.4 Ultrasound system setup on GEISS 5-axis milling machine-volume test

The laser tracer system (eTALON) was also used to validate measurement of the ultrasound system by applying the laser tracer on GEISS machine to measure same positioning measured by ultrasound system as shown in Figure 8.10, but at different time due to practical problems of using the tracker.

A test was carried out to measure the position in three levels of *z* axis and 27 positions on *x* and *y* axis as shown in Figure 8.11.

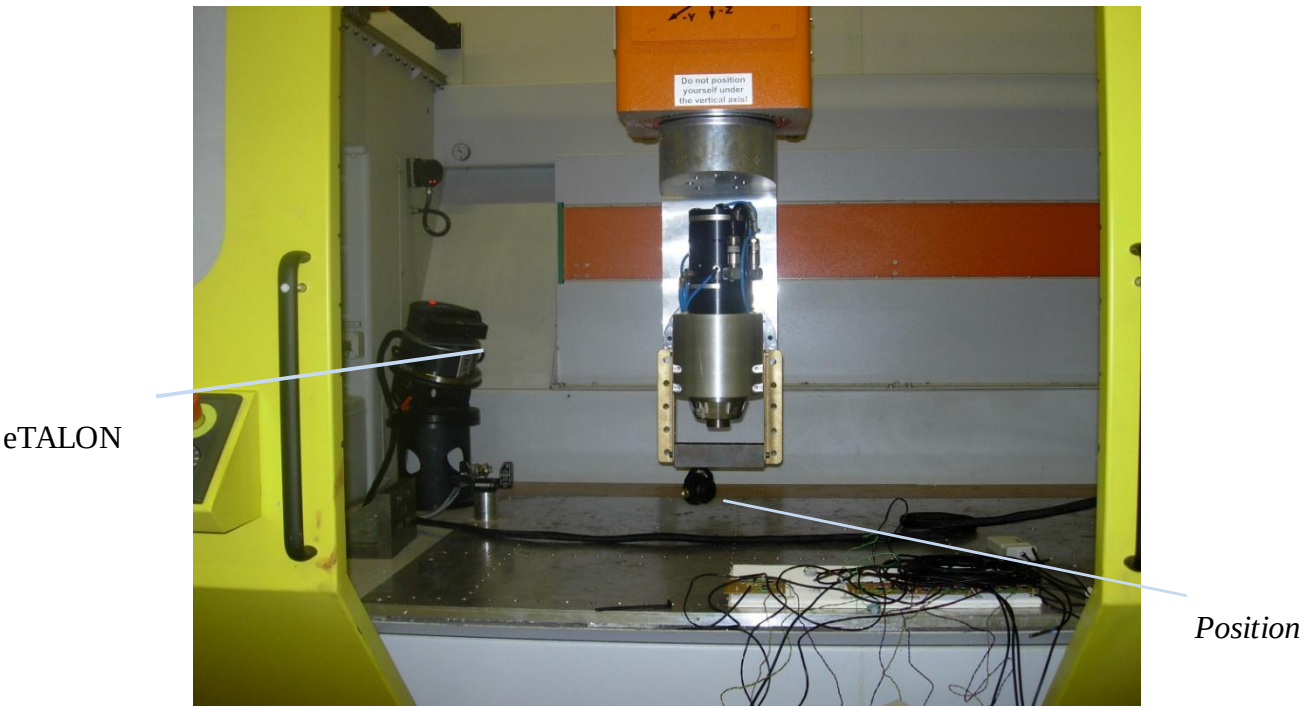

Figure 8-10 eTALON applied on GEISS machine

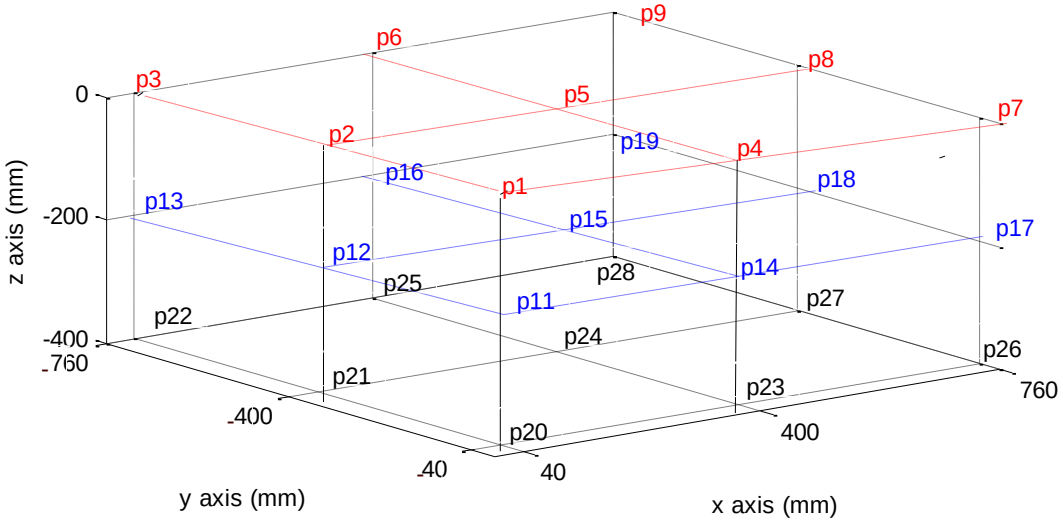

Figure 8-11 Measurement plan on workspace area

The principle of the eTALON measurement depends on a triangulation method, which means to measure accurately *x*, *y*, *z* axis on GEISS machine the eTALON system must be run at least in three positions in GEISS machine. Therefore, for best accuracy the eTALON was moved in four positions about workspace area inside the machine and the coordinates for the position calculated by eTALON software. Figure 8.12 shows the error position for the plan in Figure 8.10 measured by ultrasound system and eTALON system.

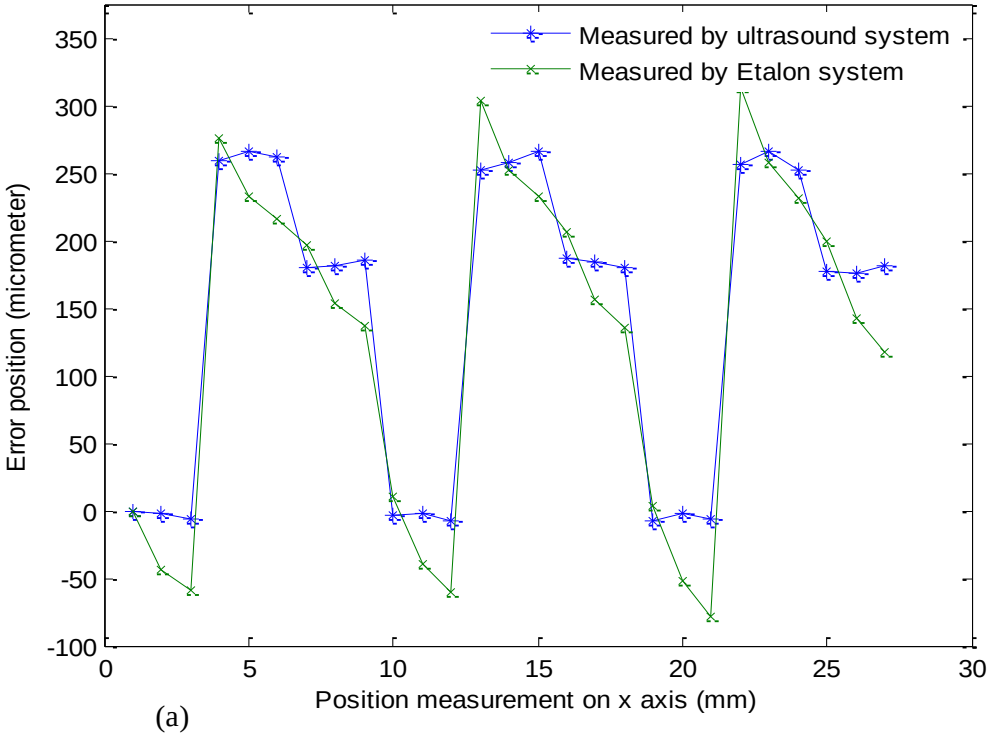
Measured by ultrasound system
Measured by Etalon system
Error position (micrometer)
Position measurement on x axis (mm)
350
300
250
200
150
100
50
0
-50
-100
0
5
10
15
20
25
30

(a)

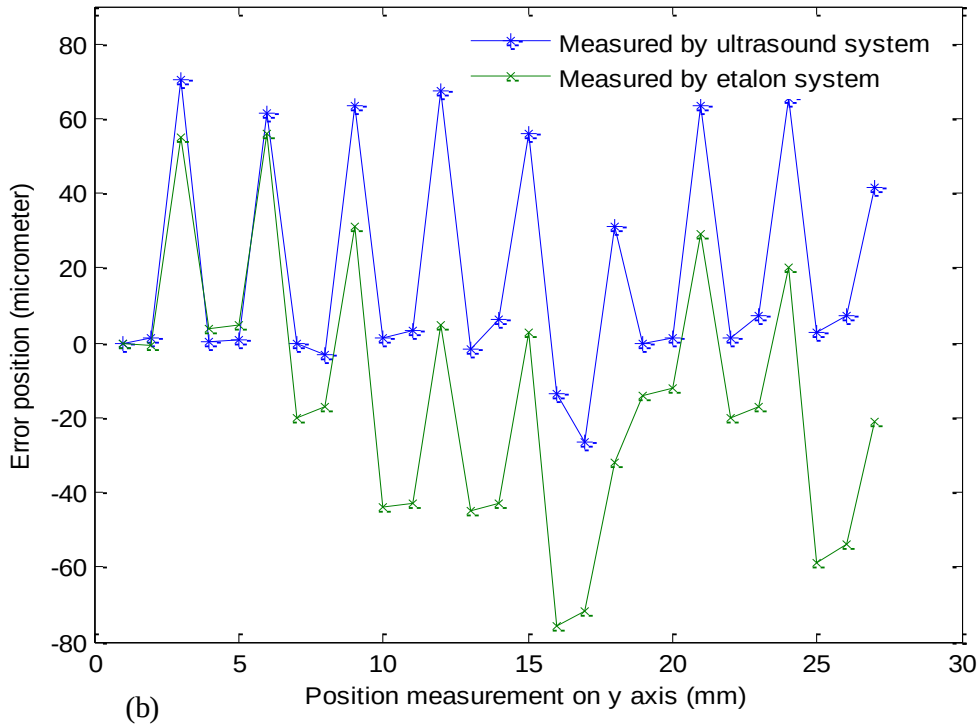
Measured by ultrasound system
Measured by etalon system
Error position (micrometer)
Position measurement on y axis (mm)
80
60
40
20
0
-20
-40
-60
-80
0
5
10
15
20
25
30

(b)

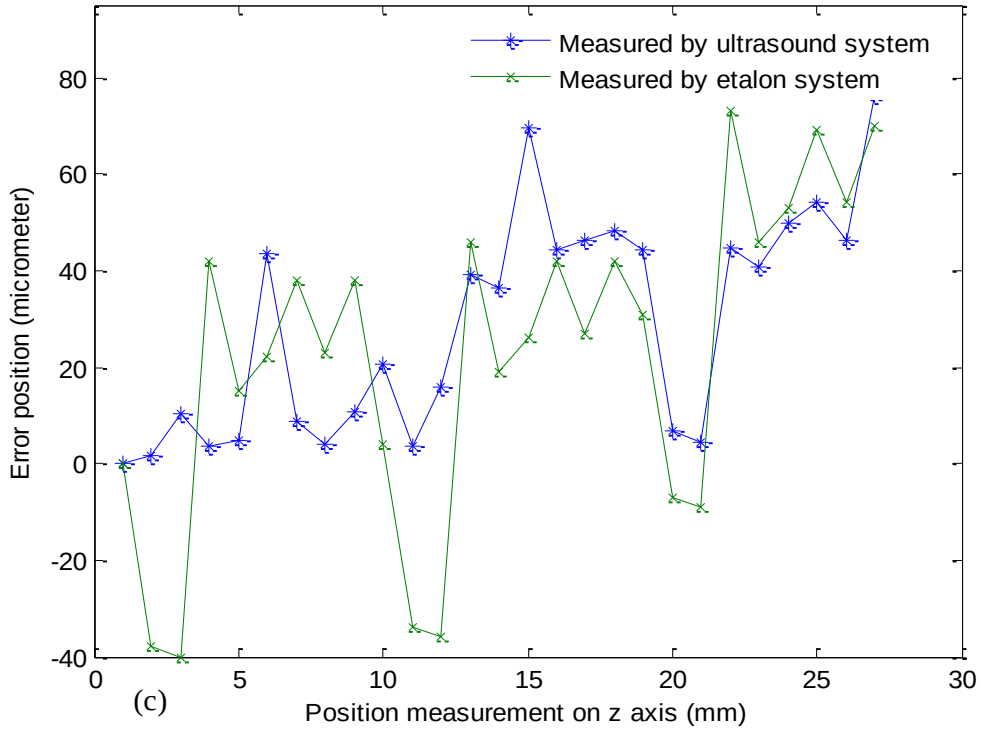

Figure 8-12 The error measured by ultrasound system and eTALON system from GEISS

(a) Measured errors on x-axis
(b) Measured errors on y-axis
(c) Measured errors on z-axis

In Figure 8.13 the difference between ultrasound system and eTALON system to measure the error position on GEISS machine. The difference between them on *x* axis was ±59μm, on *y* axis was ±67μm, and on *z* axis was ±57μm.

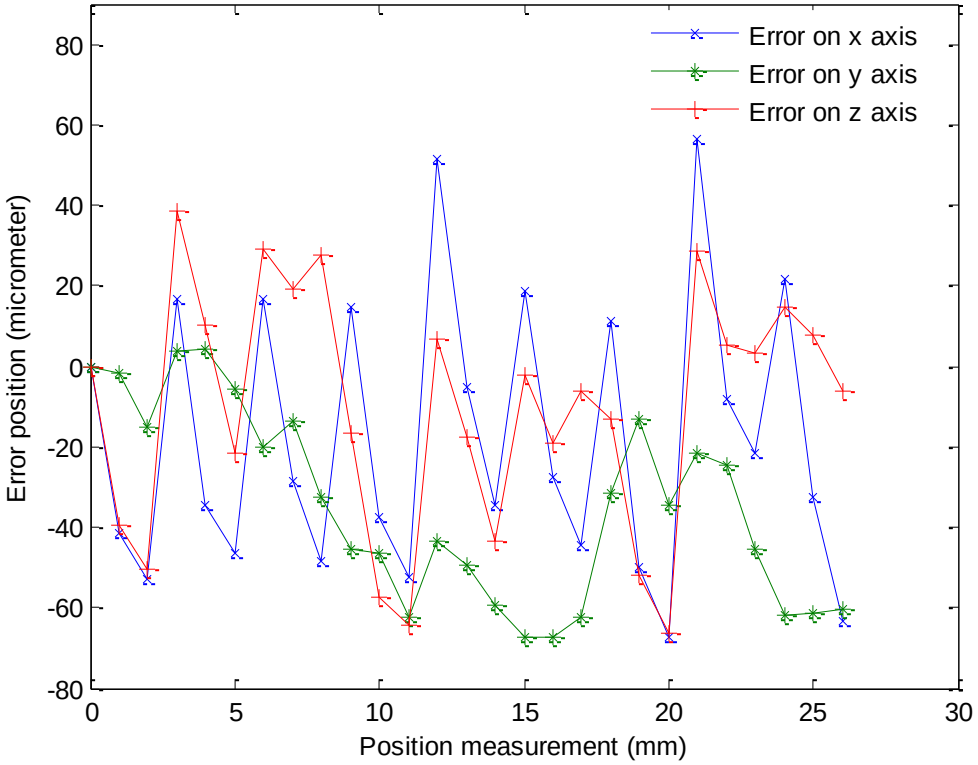

Figure 8-13 The difference between ultrasound system and eTALON system to measure the error on GEISS machine

8.5 Ultrasound system setup on GEISS 5-axis milling machine - Non-cartesian axis test

The last test on ultrasound system was of the rotary C-axis of the GEISS machine (figure 8.14). To maintain transmitter position, the spindle was rotated in anti phase.

Figure 8.16 shows the error position every 45^0 . The machine error on x axis is 0.7mm, y axis 1.23mm and on z axis 0.035mm.

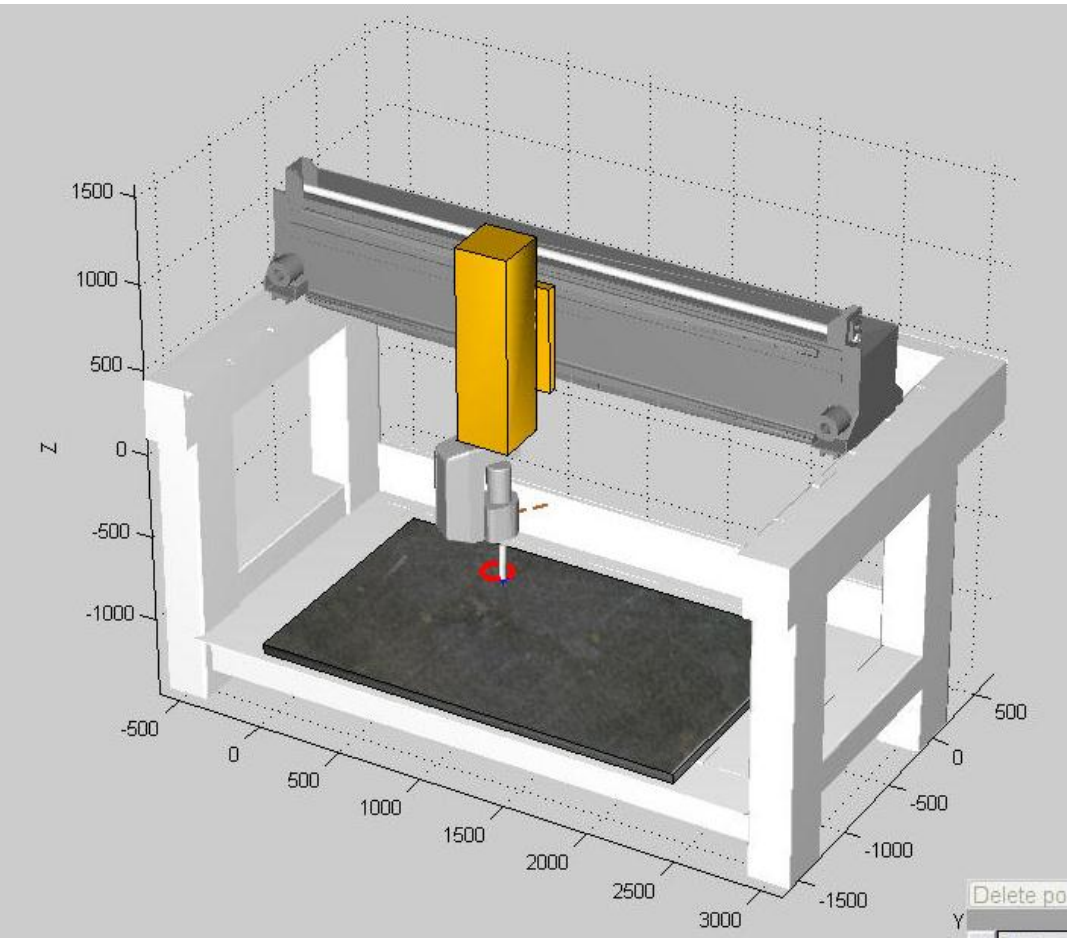

Figure 8-14 Rotate the axis about C-axis

In this test the error measured by ultrasound system need to be compare with another system measured same positions. The dial test indicators (DTIs), precision (GRADE A) test mandrel were used as shown in Figure 8.15, Figure 8.16 also shows the error measured by DTIs.

Figure 8-15 DTIs applied on GEISS machine

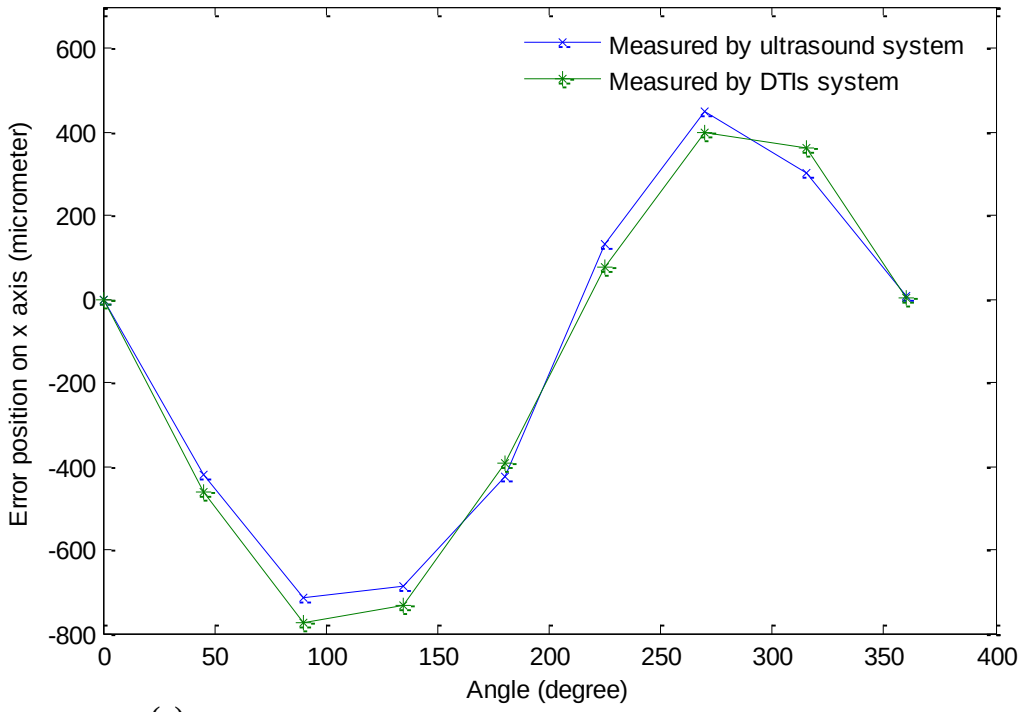
Measured by ultrasound system
Measured by DTIs system
Error position on x axis (micrometer)
Angle (degree)
600
400
200
0
-200
-400
-600
-800
0
50
100
150
200
250
300
350
400

(a)

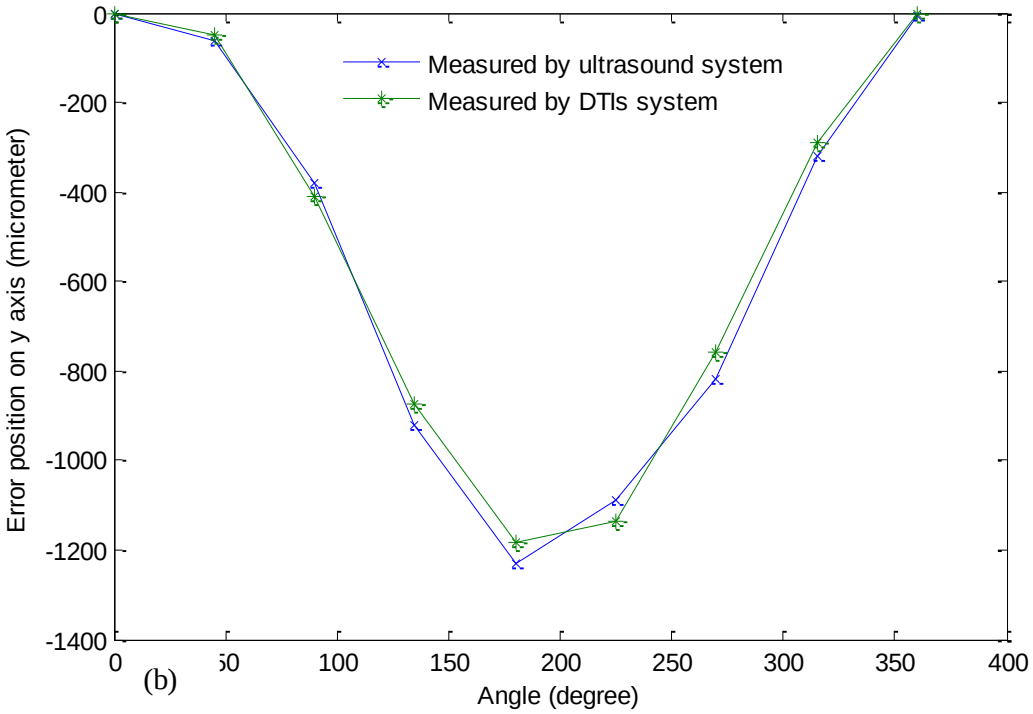
Measured by ultrasound system
Measured by DTIs system
Error position on y axis (micrometer)
Angle (degree)
0
-200
-400
-600
-800
-1000
-1200
-1400
0
100
150
200
250
300
350
400

(b)

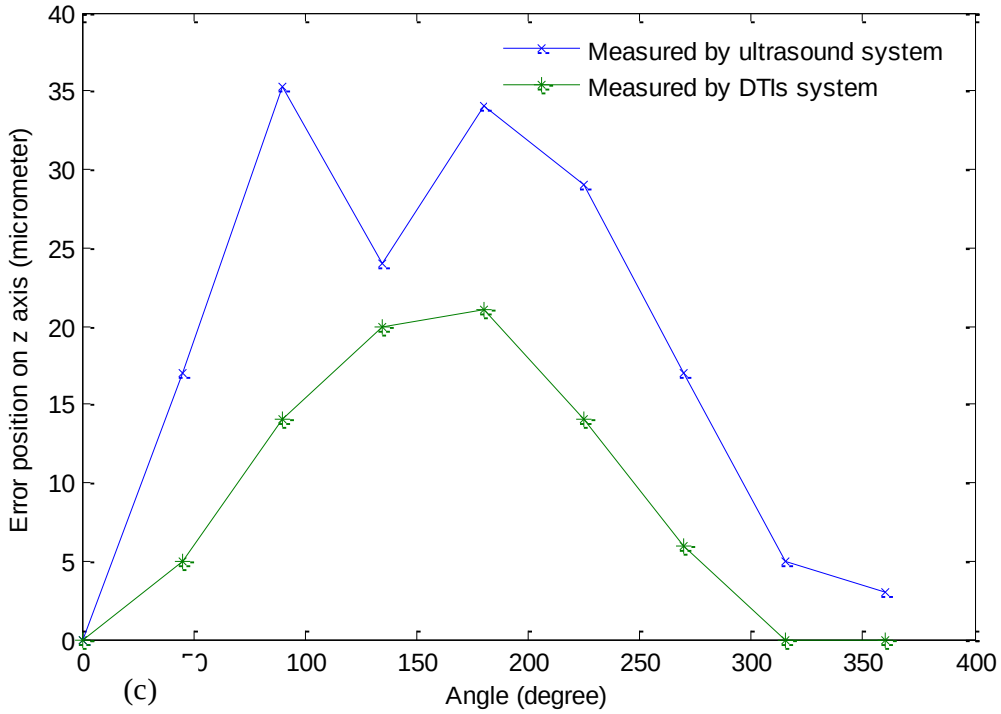

Figure 8-16 Error position after rotate about C

(a) Measured errors on x-axis
(b) Measured errors on y-axis
(c) Measured errors on z-axis

In Figure 8.17 the difference between ultrasound system and DTIs system to measuring the error position on GEISS machine. The difference between them on *x* axis was ±60μm , on *y* axis was ±60μm and on *z* axis was ±22μm.

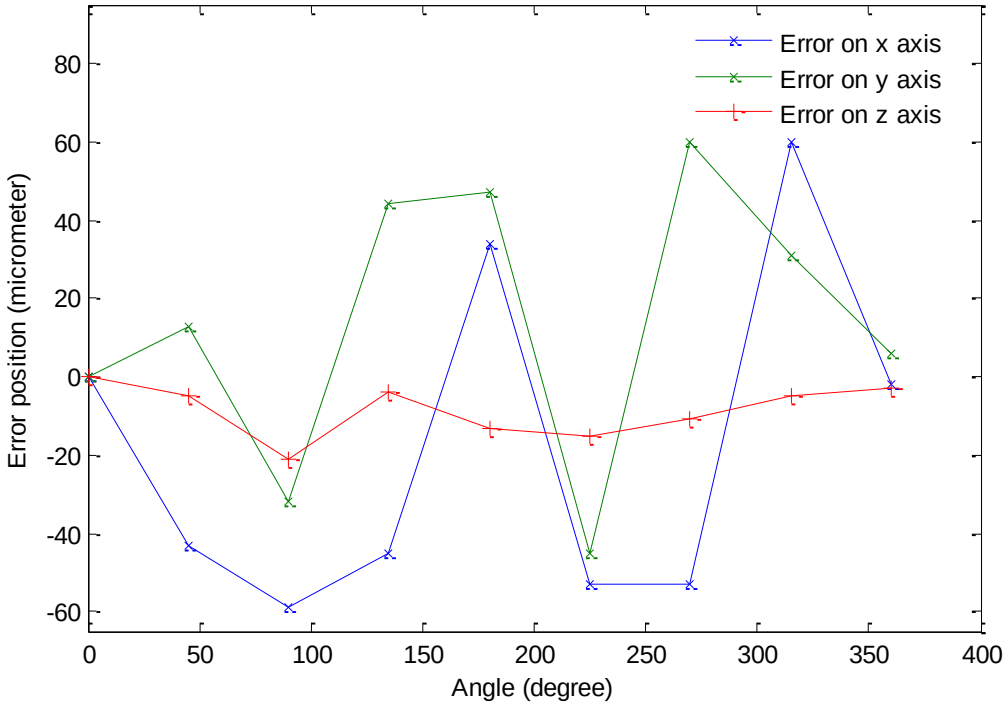

Figure 8-17 The difference between ultrasound system and DTIs system to measure the error on GEISS machine

Figures 8.18 and 8.19, respectively, show the average temperature and humidity in the workspace during measurement of the 3D position of the transmitter on Zeiss CMM.

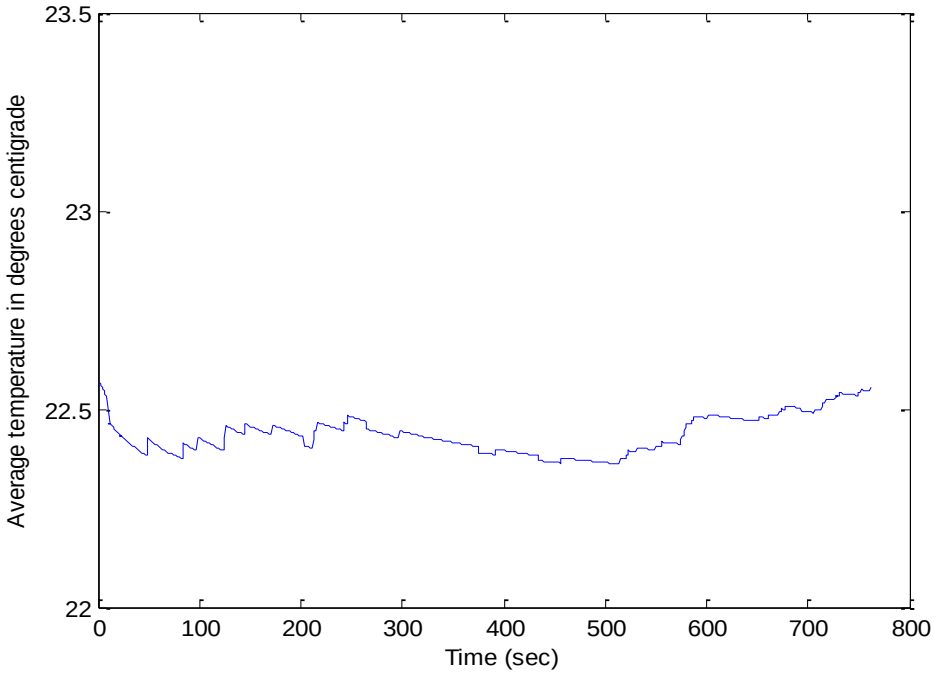

Figure 8-18 Measured temperature in workspace

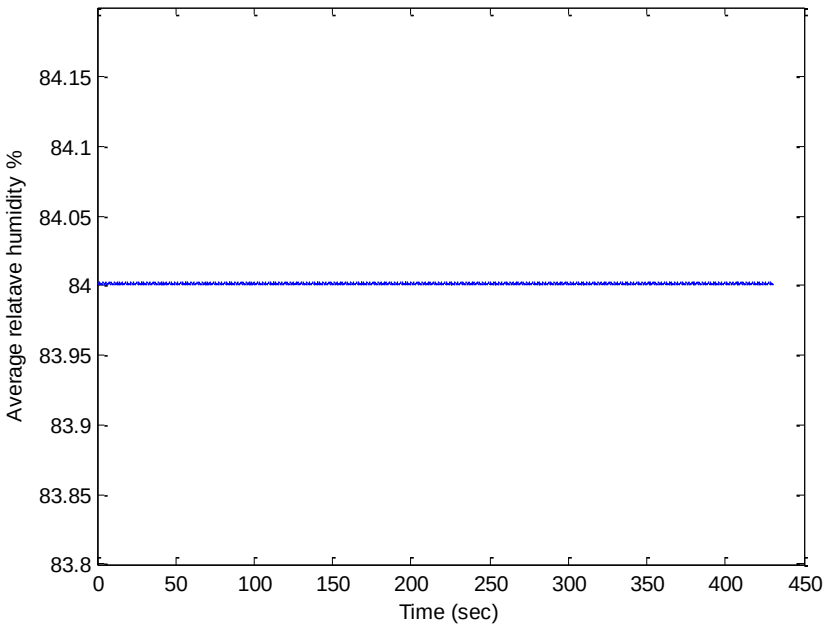

Figure 8-19 Measured humidity in workspace

8.6 Summary

This chapter has described experimental work and results on the prototype measurement system.

Table 8.1 compares the characteristics of Ultrasound system, XL-80, CMM and eTALON. It is hoped that the table will be helpful for the reader when reviewing comparison between ultrasound system and other systems in terms of the accuracy.

Table 8-1 Characteristics comparison of the Ultrasound system, XL-80, CMM and eTALON

	Ultrasound system	**eTALON**	**Renishaw XL-80**	**CMM**
Accuracy	±67μm	5μm	2μm	2μm
Measuring Volume	1.2x1.2m	15m	80m	2x1.2m
Costs	£1200	£130000	£30000	£250000
Portability	Good	Medium	Medium	-
Setup time	15 min	45 min	90 min	-
Measurement time for volume	30 min	2 hrs	2 day	-

Times estimated for a $1m^3$ volume.

Table 8.2 summarizes the validation test on the Zeiss CMM and GEISS milling machine. The system was developed for fixed and dynamic distance measurement. Its accuracy is estimated as 0.025mm compared with CMM in a $\pm 2^oC$ temperature controlled environment, about ±0.065mm in normal environment compared with eTALON, about 0.038mm compared with XL-80 and ±0.06 compared with DTIs.

Table 8-2 Comparison between ultrasound system and other systems for measuring position

Test	Comparator	Comparison accuracy
CMM	CMM	25μm
GEISS CO-liner	XL-80	38 μm
GEISS Volume	eTALON	±67μm
GEISS C-Axis	DTIs	±60μm

Chapter 9 Conclusions and recommendations for further work

9.1 Conclusions

This research has made significant achievements in the improvement of the accuracy, resolution and applicability of an ultrasonic 3D measurement system. The basis of the measurement system which has been developed during the current research is a three receiver, MFCWFM system. The accuracy of the measured 1D distance between transmitter and receiver with this system has reached an accuracy of ±0.019mm in a workspace of dimensions up to 1.2m. A number of novel techniques and algorithms have been developed during the work and presented by the author [45, 47]. The working principles of the system were presented in Section 5.2.1.

Ultrasound speed is very important in ultrasonic distance measurements. Unfortunately, this can drift with time according to the changes in the properties of the air in the workspace. The most important characteristics are air temperature and humidity. These changes have always been a problem in applications of airborne ultrasonics and, in many systems' have significantly limited measurement accuracy.

Conventional methods for ultrasound speed evaluation measure temperature and humidity at a single point in the workspace for real-time estimation of the ultrasound speed. This is simple and can be relatively effective in many cases. However, it has limitations that restrict the application of the ultrasonic measurement system. In this project a novel method for ultrasound speed evaluation was developed to further improve measurement accuracy. This new method uses two ultrasound systems for simultaneous temperature and humidity measurement [35]. The detailed working principles were presented in Section 5.2.2. The solution was obtained by solving a constrained nonlinear optimization problem. The simulation results of this method have demonstrated that the ultrasound speed drifts are evaluated with great accuracy, see Section 7.3. This new

method has the significant advantage compared with conventional methods of requiring no extra instrumentation, thus reducing the add-on cost to the measurement system.

As well as developing the MFCWFM system to measure the initial and subsequent instantaneous positions of a moving transmitter, significant improvements have been made in the practicality of the system. These have been achieved by improving the algorithm for calculating the position coordinates and removing the requirement to place the receivers at predefined, precise positions. In previous ultrasonic 3D measurement systems, the real-time calculation of the position coordinates required orthogonal placement of the receivers, which is difficult to implement in practice and restricts system flexibility. Therefore, in the early stage of this project, a new algorithm was developed to evaluate the position coordinates by iteratively solving a system of equation given in Equation (5-9), which allows arbitrary placement of receivers [50]. Subsequently, in order to simplify the task of real-time processing, a more efficient algorithm was developed to solve the equations directly, without using any iterative procedure. The detailed working principle of this new algorithm was presented in Section 5.3.

Having established an algorithm to calculate the position co-ordinates from arbitrarily-placed receivers, a new procedure was also required to determine the coordinates of the receivers. This procedure, described in Section 5.4, which calculates the receivers' 3D position from inter-receiver distances. The procedure offers a simple means of efficient and accurate receiver positioning, which significantly improves the system's flexibility and adaptability.

The final practical implementation problem addressed ultrasound echoes which cause amplitude and frequency distortions in the received ultrasound signal.

All the techniques and algorithms outlined in this research were developed towards the goal of achieving an economical, accurate real-time ultrasonic 3D measurement system that can provide high-resolution information on position coordinates. Compared with previous ultrasonic 3D measurement systems, significant improvements have been made in many different aspects during the research carried out during the current project. Table

8.2 shows 3D accuracy of 25μm in ideal condition and ±65μm in normal workshop for a $1m^3$ volume. However, a certain amount of further work is required before a fully working system can be achieved, as discussed in the following section.

9.2 Recommendations for further work

Use of the new techniques and algorithms described in this thesis has greatly improved the overall performance of a new ultrasonic 3D measurement system. So far, this has been tested in a prototype measurement system only, as described in Chapters 7 and 8, but further development is required for the measurement system to be satisfactory as a commercial product for industrial applications. This section therefore provides a number of recommendations for this further development work.

9.2.1 Implementation issues

The most immediate area of further work is to build and test a full five channel real-time system. This will need a time to complete and a moderate amount of funding. However, the research and testing carried out to date has shown that such a system will be suitable for real industrial application and have the necessary attributes of high accuracy, high resolution and low cost.

The enhancements made to the measurement system involve a significant amount of extra computation, particularly for the frequency measurement technique introduced in Section 7.2. Hence, there is a need to distribute the computation over the whole system. Therefore, the calculations for the distance measurements will be finished locally at the receivers within the system. Sixteen-bit and eight input channels for DAQ card interface with an operating speed over 6Ms/s are recommended.

All software necessary for the enhanced system is contained within the 3D system package. At present this is LABVEIW 7.1, which has become a very popular software platform. Future work should consider developing the LABVIEW version from 7.1 to 8.6, and using LABVIEW to calculate phase differences, distances and 3D positions.

The ultrasound speed evaluation technique was developed in Chapter 5 and tested in Chapter 7. The accuracy achieved for distance measurement was ±0.019mm over distances of up to 1.2m. To increase the measurement range as will be required by larger workspaces may need additional sensors/systems to preserve the accuracy of the temperature and humidity measurement.

Once the real system has been built, it will be necessary to test the magnitude of the frequency distortions involved in the frequency measurement, and see how much of these distortions can be constrained by the technique developed in Chapter 7. The essential requirement for this test is an enclosed room (or big box) lined with sound absorbing materials. By placing obstacles at different positions in the enclosure, echoes at different frequencies and amplitudes can be produced for the experiment.

9.2.2 Further enhancement to measurement performance

Although the research carried out has achieved significant improvement in measurement using the MFCWFM technique, by using more than three transmission frequencies might improve accuracy. Considering the frequency response of the ultrasound transducer, see Section 6.2, the three transmitting frequencies could be 24.5, 25 and 25.5 kHz. Alternatively burst of ultrasound at any of these frequencies could be picked up by a band-pass filter in the receiver. The frequencies used in the 3D measurement system were 100Hz, 1kHz and 25kHz, but with increase in the distance to be measure there must be a corresponding increase so that the half wavelet for the lowest frequency remains longer than the distance to be measured.

9.3 Contributions to knowledge

1- The technique used for measure distance was introduced in section 5.2.1 and the hardware and software design were introduced in chapter 6. The experimental results were introduced in chapter 8.

2- The second objective is met in sections 5.2.2 and 5.2.3 and experimental results met in section 7.3.

3- Modeling of the ultrasound transmitter-receiver signal is introduced in section 7.2 wit modeling of the ultrasound transmitter-receiver signal method for eliminated distortion frequency measurement.

4- The new 3D measurement system based on three receivers and one transmitter, as shown in sections 5.3 and 5.4. The experimental results are shown in chapter 8.

5- All the 3D measurement results from the new system was compared with CMM, eTALON, XL-80 and DTIs systems (see Tables 8.1 and 8.2), and the accuracy achieved from new system is efficient with many productise for machine calibration.

References

[1] E. Hughes, A. Wilson, and G. Peggs, "Design of a High-Accuracy CMM Based on Multi-Lateration Techniques," *CIRP Annals - Manufacturing Technology*, vol. 49. 2000, pp. 391-394.

[2] M. Vermeulen, P. Rosielle, and P. Schellekens, "Design of a High-Precision 3D-Coordinate Measuring Machine," *CIRP Annals - Manufacturing Technology*, vol. 47. 1998, pp. 447-450.

[3] A. Mahajan and F. Figueroa, "An automatic self-installation and calibration method for a 3D position sensing system using ultrasonics," *Robotics and Autonomous Systems*, vol. 28, Sep. 1999, pp. 281-294.

[4] A. Mahajan and M. Walworth, "3D position sensing using the differences in the time-of-flightsfrom a wave source to various receivers," *Robotics and Automation*, vol. 17, Feb. 2001, pp. 91-94.

[5] P.K. Ray and A. Mahajan, "A genetic algorithm-based approach to calculate the optimal configuration of ultrasonic sensors in a 3D position estimation system," *Robotics and Autonomous Systems*, vol. 41, Dec. 2002, pp. 165-177.

[6] M. MARTIN, R. JIMENEZ, F. SECO, L. CALDERON, L. PONS, and R. CERES, "Estimating the 3D-position from time delay data of US-waves: experimental analysis and a new processing algorithm," *Department of Sensor Systems, Instituto de Automática Industrial*, vol. 101, 2002, pp. 311-321.

[7] A. Jim´enez and F. Seco, "Precise Localisation of Archaeological Findings with a new Ultrasonic 3D Positioning Sensor," *Sensors & Actuators*, vol. 123-4, May. 2005, pp. 214-233.

[8] J. Owens, "Calibration on a Shoestring," *Industrial Robot*, vol. 21, 1994, pp. 10-13.

[9] G. Simon, "Optotrac-cat's eyes and lasers," *Industrial Robot*, vol. 21, 1994, pp. 18-21.

[10] B. PREISING and C. HSIA, "Robot performance measurement and calibration using a 3D computer vision system," *Univ. California, dep. electrical computer eng*, vol. 13, 1991, pp. 327-337.

[11] C. Koh, "A position estimation system for mobile robots using a monocular image of a 3-D landmark," *Robotica*, vol. 12, 1995, pp. 431-441.

[12] S. Kim, H. Rhee, and J. Chu, "Volumetric phase-measuring interferometer for three-dimensional coordinate metrology," *Precision Engineering*, vol. 27, 2003, pp. 205-215.

[13] M. Muquit, T. Shibahara, and T. Aoki, "A High-Accuracy Passive 3D Measurement System using Phase- Based ," *IEICE Trans*, vol. E89-A, 2006.

[14] R. Tsai, "A versatile camera calibration technique for high-accuracy 3D machine vision metrology using off-the-shelf TV cameras and lenses," *Robotics and Automation, IEEE , Journal Of Packaging And Manufacturing Technology Society*, vol. 3, 1987, pp. 323-344.

[15] K. Araki, M. Shimizu, T. Noda, Y. Chiba, Y. Tsuda, K. Ikegaya, K. Sannomiya, and M. Gomi, "A high-speed and continuous 3D measurement system," *Machine Vision and Applications*, vol. 8, Mar. 1995, pp. 79-84.

[16] M. Hartrumpf and R. Munser, "Optical three-dimensional measurements by radially symmetric structured light projection," *Applied Optics*, vol. 36, May. 1997, pp. 2923-2928.

[17] Y. Nishida, H. Aizawa, T. Hori, N. Hoffman, T. Kanade, and M. Kakikura, "3D ultrasonic tagging system for observing human activity," *Intelligent Robots and Systems, 2003. (IROS 2003). Proceedings, 2003 IEEE/RSJ International Conference*, vol. 1. 2003, pp. 785-791.

[18] R.J. Valkenburg and A.M. McIvor, "Accurate 3D measurement using a structured light system," *Image and Vision Computing*, vol. 16, Feb. 1998, pp. 99-110.

[19] J.M.S.T. Motta, G.C. de Carvalho, and R.S. McMaster, "Robot calibration using a 3D vision-based measurement system with a single camera," *Robotics and Computer-Integrated Manufacturing*, vol. 17, Dec. 2001, pp. 487-497.

[20] T. Fohanno, "Assessment of the mechanical performance of industry robot," *General method staff, automobile citroen, France*, 1982.

[21] G. LEGNANI, C. MINA, and J. TREVEL, "Static calibration of industrial manipulators : Design of an optical instrumentation and application to SCARA robots," *Robotic Systems* , vol. 13, 1996, pp. 445-460.

[22] H. Zhuang and Z. Roth, "Modeling Gimbal Axis Misalignments and Mirror Center Offset in a Single-Beam Laser Tracking Measurement System," *Int. J. Robot*, vol. 14, 1995, pp. 3416-3421.

[23] R. Mayer and A. Parker, "A portable instrument for 3-D dynamic robot measurements usingtriangulation and laser tracking," *Robotics and Automation*, vol. 10, Aug. 1994, pp. 504-516.

[24] M. Vince, P. Prenninger, and H. Gander, "A laser tracking system to measure position and orientation of robot end effectors under motion ," *Robot. Res*, vol. 13, 1994, pp. 305-314.

[25] S. Spiess, M. Vincze, and M. Ayromlou, "On the calibration of a 6-D laser tracking system for dynamic robot measurements," *IEEE Trans Of Packaging And Manufacturing Technology Society*, vol. 47, 1998, pp. 270-274.

[26] J. Yuan and L. Yu, Article Information End-effector position-orientation measurement, *Robotics and Automation,*, vol. 15, 1999, pp. 592-595.

[27] "(www.manufacturingtalk.com/news/npt/npt115.html," 2008.

[28] "www.manufacturingtalk.com/news/rea/rea494.htm," 2009.

[29] D. Albada, M. Lagerberg, and A. Visser, "Eye in hand robot calibration," *Industrial Robot*, vol. 21, 1994, pp. 14-17.

[30] P. Webb and C. Wykes, "High-Resolution beam forming for ultrasonic arrays," *IEEE Trans*, vol. 12, 1996, p. 138.

[31] M. Dickinson and S. Morris, "Co-ordinate determination and performance analysis for robot manipulators," *IEEE Proc*, vol. 135, 1988, pp. 95-98.

[32] W. Moritz, P. Shreve, and L. Mace, "Analysis of an ultrasonic spatial locating system," *IEEE, Packaging And Manufacturing Technology Society*, vol. 25, 1976, pp. 43-50.

[33] M. Yang, K. Huang, C. Huang, and M. Young, "A highly accurate ultrasonic measurement system for tremor using binary amplitude shift keying and phase shift method," *Biomedical engineering*, vol. 15, 2003, pp. 61-67.

[34] W. Tsai, C. Huang, and T. Liao, "New implementation of high-precision and instant-response air thermometer by ultrasonic sensors," *Sensors and Actuators A: Physical*, vol. 117, Jan. 2005, pp. 88-94.

[35] F. Aldawi, A. Longstaff, S. Fletcher, C. Pislaru, A. Myers, and J. Briggs, "A high accuracy ultrasonic system for measurement of air temperature," *Proceedings of the euspen international conference- San sebastian*, vol. 2, 2009, pp. 134-137.

[36] S. Glegg, "Ultrasonics (Wykeham Science Series No. 55) 1980, by A. P. Cracknell. London: Wykeham Publications (London) Ltd. (New York: Crane Russak & Company, Inc.) 200 pp.," Oct. 1980.

[37] M.G. Silk, *Ultrasonic transducers for nondestructive testing*, 1984.

[38] O. Oralkan, A. Ergun, J. Johnson, M. Karaman, U. Demirci, K. Kaviani, T. Lee, and B. Khuri-Yakub, "Capacitive micromachined ultrasonic transducers: next-generation arrays for acoustic imaging?," *Ultrasonics, Ferroelectrics and Frequency Control, IEEE Transactions ,Packaging And Manufacturing Technology Society*, vol. 49, 2002, pp. 1596-1610.

[39] J.A. Jensen, *Estimation of Blood Velocities Using Ultrasound*, Cambridge University Press, 1996.

[40] J. Souquet, P. Defranould, and J. Desbois, "Design of Low-Loss Wide-Band Ultrasonic Transducers for Noninvasive Medical Application," *Sonics and Ultrasonics, IEEE Transactions, Packaging And Manufacturing Technology Society*, vol. 26, 1979, pp. 75-80.

[41] G.G. Yaralioglu, I.O. Wygant, T.C. Marentis, and B.T. Khuri-Yakub, "Ultrasonic Mixing in Microfluidic Channels Using Integrated Transducers," *Analytical Chemistry*, vol. 76, Jul. 2004, pp. 3694-3698.

[42] M. Parrilla, J. Anaya, and C. Fritsh, "Digital signal processing techniques for high accuracy ultrasonic range measurements," *IEEE Trans, Packaging And Manufacturing Technology Society*, vol. 40, 1991, pp. 759-763.

[43] J. Petzing, "The analysis of ultrasonic machining systems using wholefield interferometric techniques ," Loughborough, 1996.

[44] A. Mahajan and F. Figueroa, "Intelligent seam tracking using ultrasonic sensors for robotic welding," *Robotica*, vol. 15, 1997, pp. 275-281.

[45] F. Aldawi, A. Longstaff, S. Fletcher, P. Mather, and A. Myers, "A low-cost ultrasonic 3D measurement device for calibration for Cartesian and non-Cartesian machines," *3rd International Symposium on Advanced Fluid/Solid Science and Technology in Experimental Mechanics, Tainan, Taiwan*, 2008.

[46] F. Aldawi, A. Longstaff, S. Fletcher, P. Mather, and A. Myers, "A low-cost ultrasonic 3D measurement device for calibration for Cartesian and non-Cartesian machines, *Special*

issue of Journal of the Japanese Society for Experimental Mechanics, vol. 9, 2009, pp. 77-80.

[47] F. Aldawi, A. Longstaff, S. Fletcher, P. Mather, A. Myers, and J. Briggs, "A multifrequency FM-Based ultrasonic system for accurate 3D measurement," *School of Computing and Engineering Conference, University of Huddersfield* , 2008, pp. 9-13.

[48] C. Huang and M. Young, "Multiple-frequency continuous wave ultrasonic system for accurate distance measurement," *American Institute of Physics*, vol. 70, 1998, pp. 1452-1458.

[49] B. Dennis, "Environmental effects on the speed of sound," *Engineering Society*, vol. 36, 1988.

[50] F. Aldawi, A. Longstaff, S. Fletcher, C. Pislaru, and A. Myers, "Improved 3D position measurement using ultrasonic sensors," *Submitted for Journal of the International Measurement Confederation*, 2009.

[51] B. Gold and N. Morgan, *Speech and audio signal processing*, Berkeley: University of california, 1999.

[52] K. Stroud, *Engineering mathematics*, coventry: Lanchester polytechnic, 1982.

[53] K. Stroud, *Further engineering mathematics*, Coventry: Lanchester polytechnic, 1986.

[54] J.A. Jensen, *Estimation of blood velocities using ultrasound*, Cambridge University Press, 1996.

[55] B.A.J. Angelsen and R.C. Waag, "Ultrasound Imaging: Waves, Signals, and Signal Processing," *The Journal of the Acoustical Society of America*, vol. 121, Apr. 2007, p. 1820.

[56] V. Hans, G. Poppen, E. von Lavante, and S. Perpeet, "Vortex shedding flowmeters and ultrasound detection: signal processing and influence of bluff body geometry," *Flow Measurement and Instrumentation*, vol. 9, Jun. 1998, pp. 79-82.

[57] M. Fink, F. Hottier, and J. Cardoso, "Ultrasonic signal processing for attenuation measurement: Short time Fourier analysis," *Ultrasonic Imaging*, vol. 5, Apr. 1983, pp. 117-135.

[58] R. Rohling, A. Gee, and L. Berman, "Three-dimensional spatial compounding of ultrasound images," *Medical Image Analysis*, vol. 1, Apr. 1997, pp. 177-193.

[59] Y. Wang and P.J. Fish, "Arterial Doppler signal simulation by time domain processing," *European Journal of Ultrasound*, vol. 3, Jan. 1996, pp. 71-81.

[60] M. Riccabona, T.R. Nelson, and D.H. Pretorius, "Three-dimensional ultrasound: accuracy of distance and volume measurements," *Ultrasound in Obstetrics and Gynecology*, vol. 7, 1996, pp. 429-434.

[61] M. Riccabona, T.R. Nelson, D.H. Pretorius, and T.E. Davidson, "Distance and volume measurement using three-dimensional ultrasonography," *J Ultrasound Med*, vol. 14, Dec. 1995, pp. 881-886.

[62] W. Haigis, B. Lege, N. Miller, and B. Schneider, "Comparison of immersion ultrasound biometry and partial coherence interferometry for intraocular lens calculation according to Haigis," *Graefe's Archive for Clinical and Experimental Ophthalmology*, vol. 238, 2000, pp. 765-773.

[63] P.P. Antich, J.A. Anderson, R.B. Ashman, J.E. Dowdey, J. Gonzales, R.C. Murry, J.E. Zerwekh, and C.Y.C. Pak, "Measurement of mechanical properties of bone material in vitro by ultrasound reflection: Methodology and comparison with ultrasound transmission,"

Journal of Bone and Mineral Research, vol. 6, 1991, pp. 417-426.
[64] A. McNab and I. Stumpf, "Monolithic phased array for the transmission of ultrasound in NDT ultrasonics," *Ultrasonics*, vol. 24, May. 1986, pp. 148-155.
[65] I.Y. Solodov, R. Stoessel, and G. Busse, "*Material - Characterization - And - Nde - Using - Focused - Slanted - Transmission - Mode - Of - Air-Coupled - Ultrasound - Pb* - Taylor & Francis," *Research in Nondestructive Evaluation*, vol. 15, 2004, p. 65.

Appendix A

List of publications arising out of this research

[1] F. Aldawi, A. Longstaff, S. Fletcher, C. Pislaru, A. Myers, and J. Briggs, "A high accuracy ultrasonic system for measurement of air temperature," *Proceedings of the euspen international conference- San sebastian*, vol. 2, 2009, pp. 134-137.

[2] F. Aldawi, A. Longstaff, S. Fletcher, P. Mather, and A. Myers, "A low-cost ultrasonic 3D measurement device for calibration for Cartesian and non-Cartesian machines," *3rd International Symposium on Advanced Fluid/Solid Science and Technology in Experimental Mechanics, Tainan, Taiwan*, 2008.

[3] F. Aldawi, A. Longstaff, S. Fletcher, P. Mather, and A. Myers, "A low-cost ultrasonic 3D measurement device for calibration for Cartesian and non-Cartesian machines, *Special issue of Journal of the Japanese Society for Experimental Mechanics*, vol. 9, pp. 77-80, 2009.

[4] F. Aldawi, A. Longstaff, S. Fletcher, P. Mather, A. Myers, and J. Briggs, "A multifrequency FM-Based ultrasonic system for accurate 3D measurement," *School of Computing and Engineering Conference, University of Huddersfield* , 2008, pp. 9-13.

[5] F. Aldawi, A. Longstaff, S. Fletcher, C. Pislaru, and A. Myers, "Improved 3D position measurement using ultrasonic sensors," *Submitted for Journal of the International Measurement Confederation*, 2009.

Appendix B

Hardware

PCI-6110

NI 6120, NI 6115, NI 6110, NI 6111

- 2 or 4 analog inputs; dedicated A/D converter per channel
- 1 to 10 MS/s per channel maximum sample rate
- Analog and digital triggering
- AC or DC coupling
- 8 input ranges from ±200 mV to ±42 V
- 2 analog outputs at 4 MS/s single channel or 2.5 MS/s dual channel
- 8 digital I/O lines (5 V TTL/CMOS)
- Two 24-bit counter/timers
- Measurement services that simplify configuration and measurements

Operating Systems

- Windows 2000/NT/XP
- Mac OS X
- Linux

Recommended Software

- LabVIEW 7.x or higher
- LabWindows/CVI 7.x or higher
- Measurement Studio 7.x or higher
- Digital Waveform Editor
- SignalExpress 1.x or higher

Other Compatible Software

- VI Logger 2.x or higher
- Visual Studio .NET
- Visual Basic, C/C++, and C#

Measurement Services Software (included)[1]

- NI-DAQmx driver software
- Measurement & Automation Explorer configuration utility
- VI Logger Lite data-logging software

[1]Mac OS X and Linux applications must use NI-DAQmx Base driver software.

Calibration Certificate Available

Family	Bus	Analog Inputs	Input Resolution (bits)	Sampling Rate (MS/s)	Input Range (V)	Analog Outputs	Max Output Rate (MS/s)	Output Range (V)	Digital I/O	Counter/ Timers	Triggers
NI 6120	PCI, PXI	4	16	1[3]	±0.2 to ±42	2	4[1]	±10	8[2]	2, 24-bit	Analog, digital
NI 6115	PCI, PXI	4	12	10	±0.2 to ±42	2	4[1]	±10	8[2]	2, 24-bit	Analog, digital
NI 6110	PCI	4	12	5	±0.2 to ±42	2	4[1]	±10	8	2, 24-bit	Analog, digital
NI 6111	PCI	2	12	5	±0.2 to ±42	2	4[1]	±10	8	2, 24-bit	Analog, digital

[1]4 MS/s single channel; 2.5 MS/s on two channels [2]Hardware-timed up to 10 MB/s [3]800 kS/s with NI-DAQmx, 1 MS/s with additional download. Special conditions apply.

S Series Multifunction DAQ 12 or 16-Bit, 1 to 10 MS/s, 4 Analog Inputs

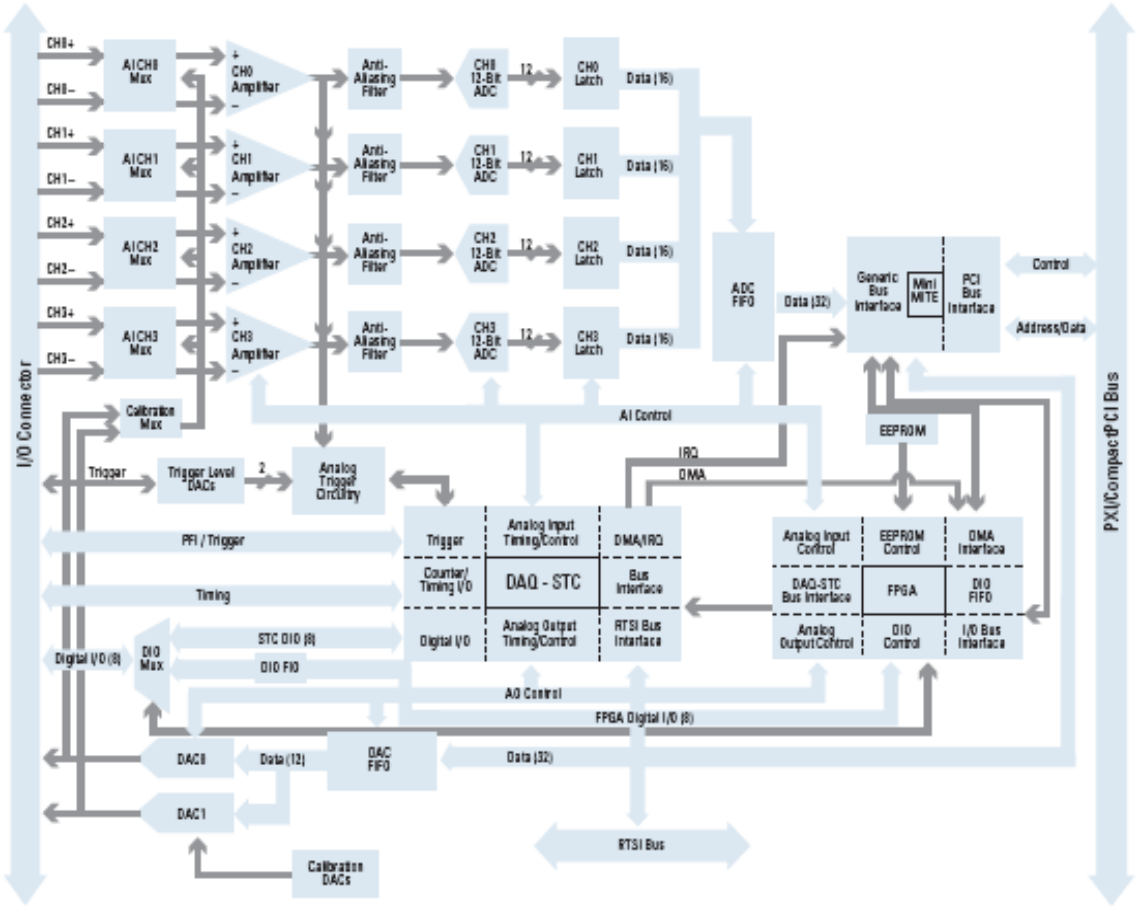

Figure 2. NI 6120 and NI 6115 Hardware Block Diagram

S Series Multifunction DAQ 12 or 16-Bit, 1 to 10 MS/s, 4 Analog Inputs

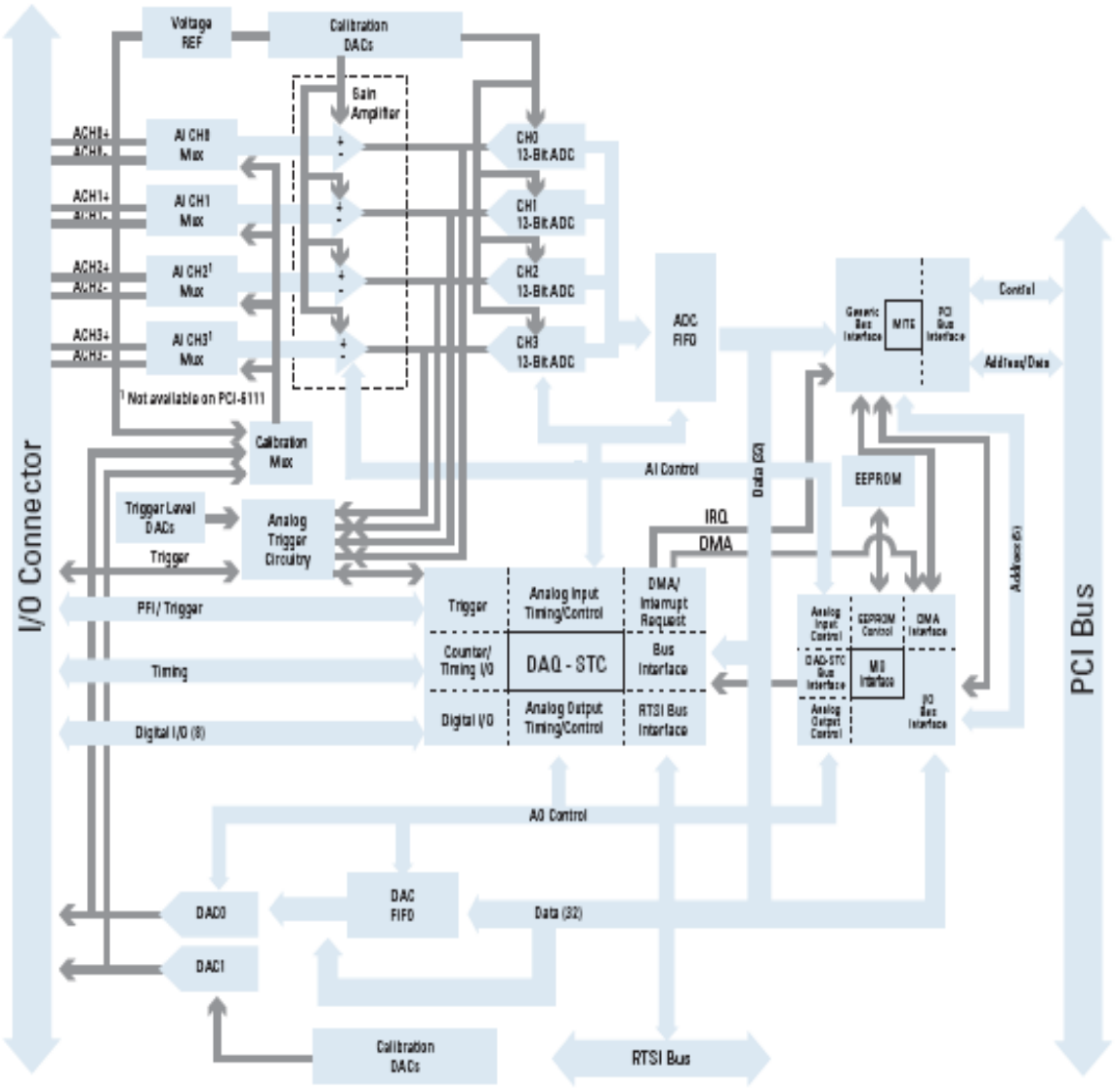

Figure 3. NI 6110 and 6111 Hardware Block Diagram

DAQ Accessories Selection Guide

NI Cable Design Advantages

National Instruments offers many different high-performance shielded cables that have been specially designed for specific NI multifunction DAQ devices. Each type of cable features improved signal integrity using the following technologies:

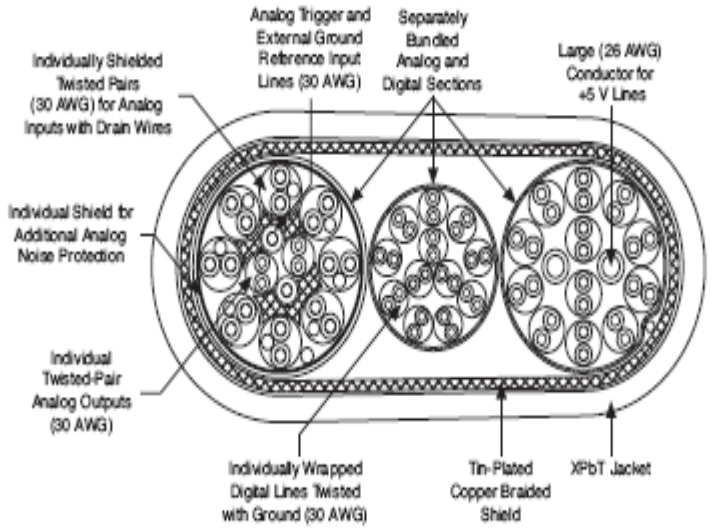

Figure 1. Enhanced-Performance Shielded Cable Used in the SHC68-68-EPM Cable

SCB-68

- Screw terminals for easy I/O connections or use with the CA-1000
- Shielded I/O connector block for use with 68-pin M, E, B, S, and R Series DAQ devices
- Onboard cold-junction compensation sensor for low-cost thermocouple measurements
- 2 general-purpose breadboard areas
- For highly accurate thermocouple measurements, use SCC or SCXI signal conditioning

Overview

The SCB-68 is a shielded I/O connector block for interfacing I/O signals to plug-in DAQ devices with 68-pin connectors. Combined with the shielded cables, the SCB-68 provides rugged, very low-noise signal termination.The SCB-68 is compatible with single and dual connector M Series devices with 68-pin connectors. The connector block is also compatible with most E, B, S, and R Series DAQ devices.

Appendix C

Software

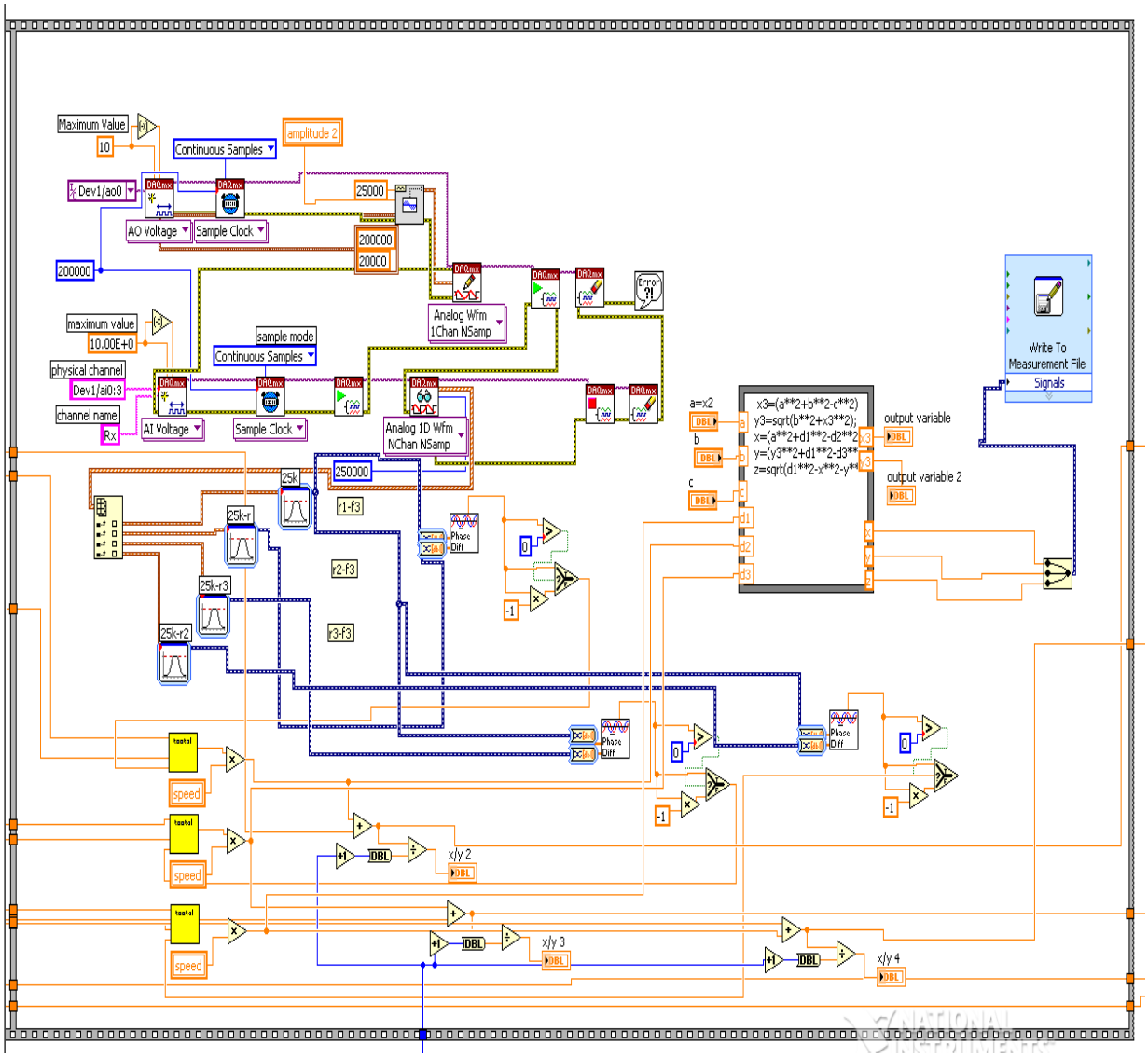

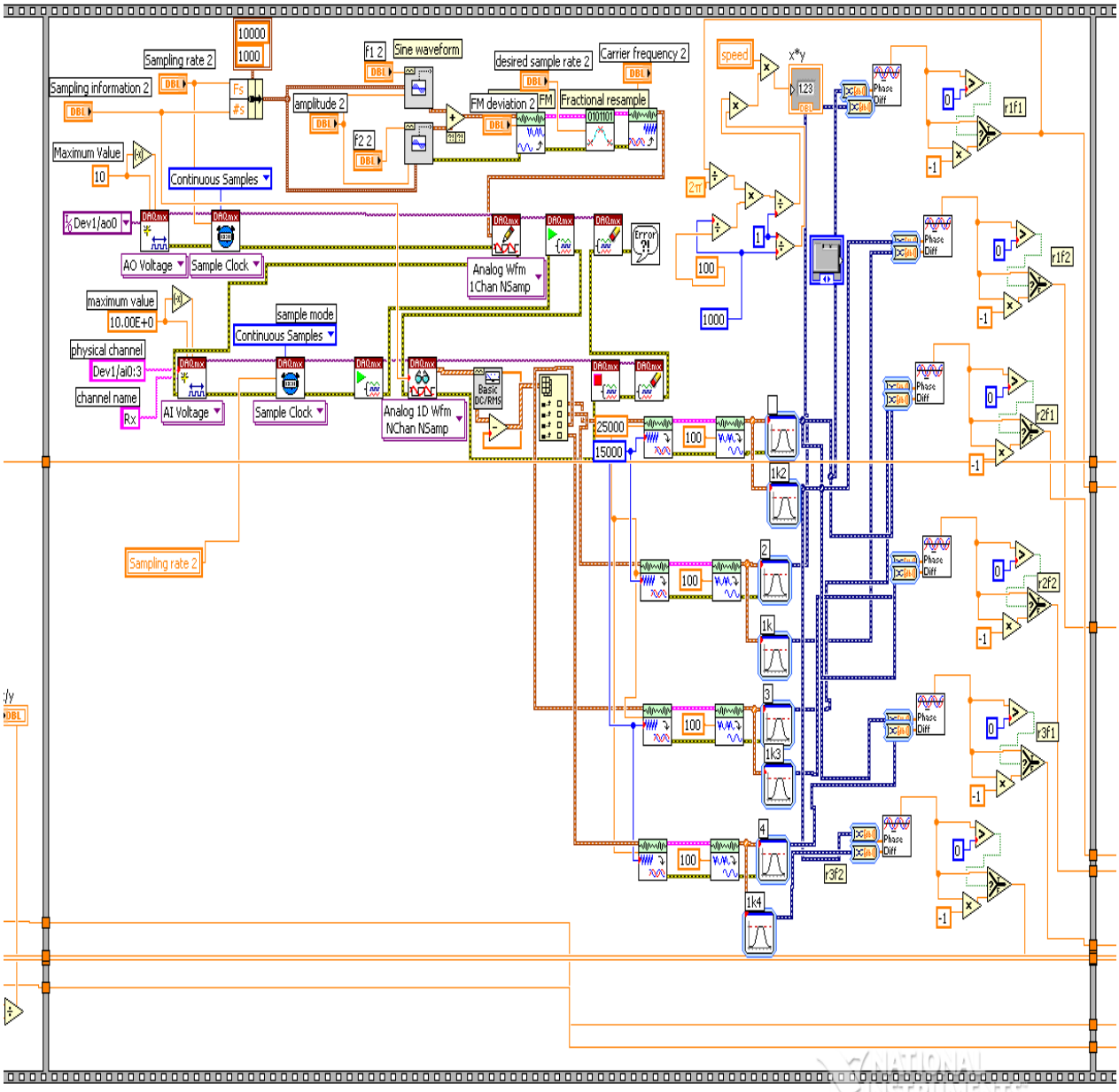
10000
1000
Sampling rate 2
Sampling information 2
Fs
#s
f1 2
Sine waveform
amplitude 2
F2 2
desired sample rate 2
Carrier frequency 2
FM deviation 2
FM
Fractional resample
0101101
speed
x*y
I123
Phase Diff
Maximum Value
10
Continuous Samples
Dev1/ao0
AO Voltage
Sample Clock
Analog Wfm 1Chan NSamp
Error
maximum value
10.00E+0
sample mode
Continuous Samples
physical channel
Dev1/ai0:3
channel name
Rx
AI Voltage
Sample Clock
Analog 1D Wfm NChan NSamp
BasIC DC/RMS
25000
15000
100
1000
2π
1
-1
0
1k2
1k
1k3
1k4
2
3
4
r1f1
r1f2
r2f1
r2f2
r3f1
r3f2
Sampling rate 2
NATIONAL INSTRUMENTS

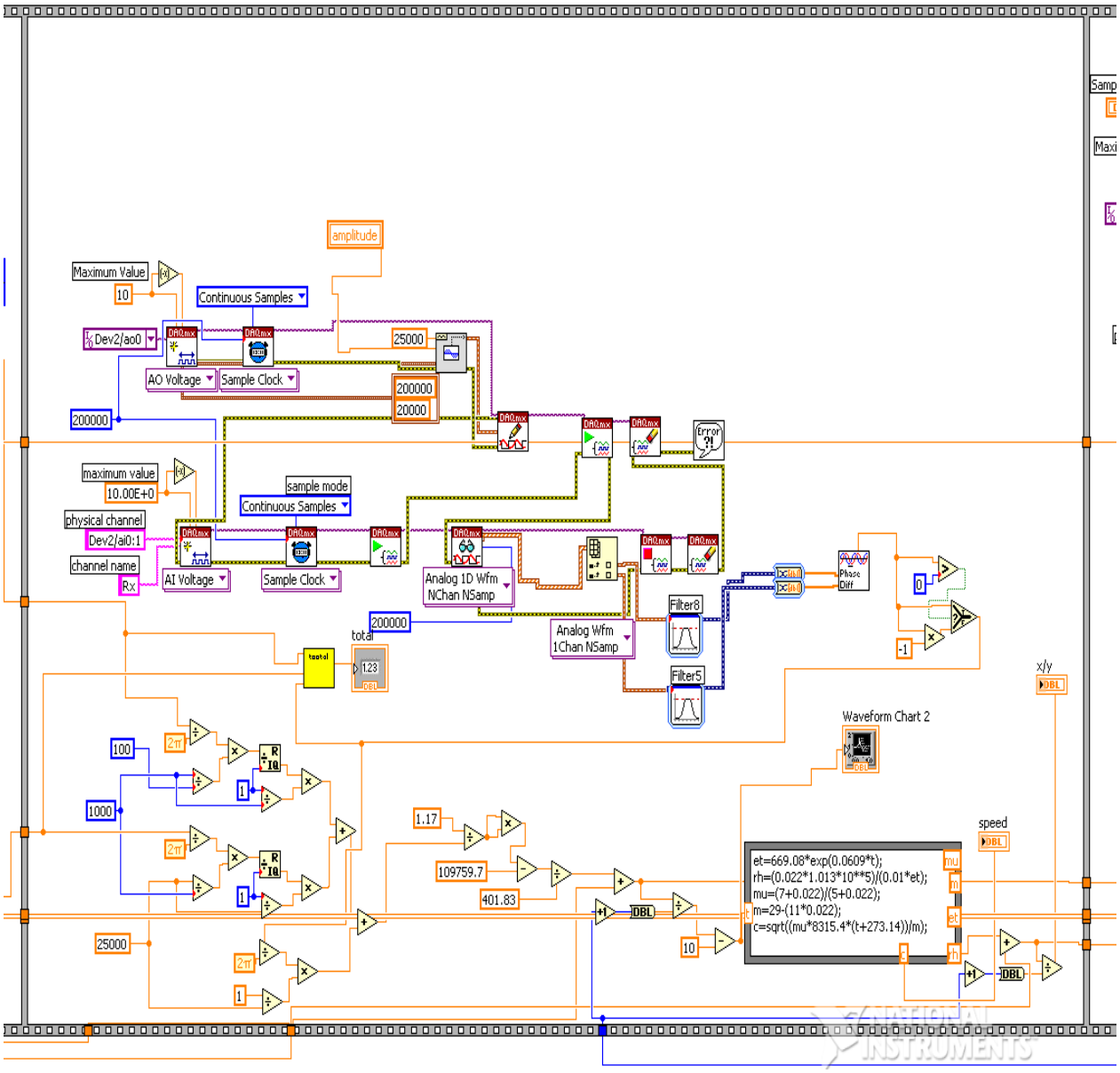
amplitude
Maximum Value
10
Continuous Samples
Dev2/ao0
25000
AO Voltage
Sample Clock
200000
20000
200000
maximum value
10.00E+0
sample mode
Continuous Samples
physical channel
Dev2/ai0:1
channel name
Rx
AI Voltage
Sample Clock
Analog 1D Wfm
NChan NSamp
Filter8
200000
total
Analog Wfm
1Chan NSamp
Filter5
Phase
Diff
0
-1
x/y
Waveform Chart 2
speed
100
1000
25000
1.17
109759.7
401.83
10
et=669.08*exp(0.0609*t);
rh=(0.022*1.013*10**5)/(0.01*et);
mu=(7+0.022)/(5+0.022);
m=29-(11*0.022);
c=sqrt((mu*8315.4*(t+273.14))/m);

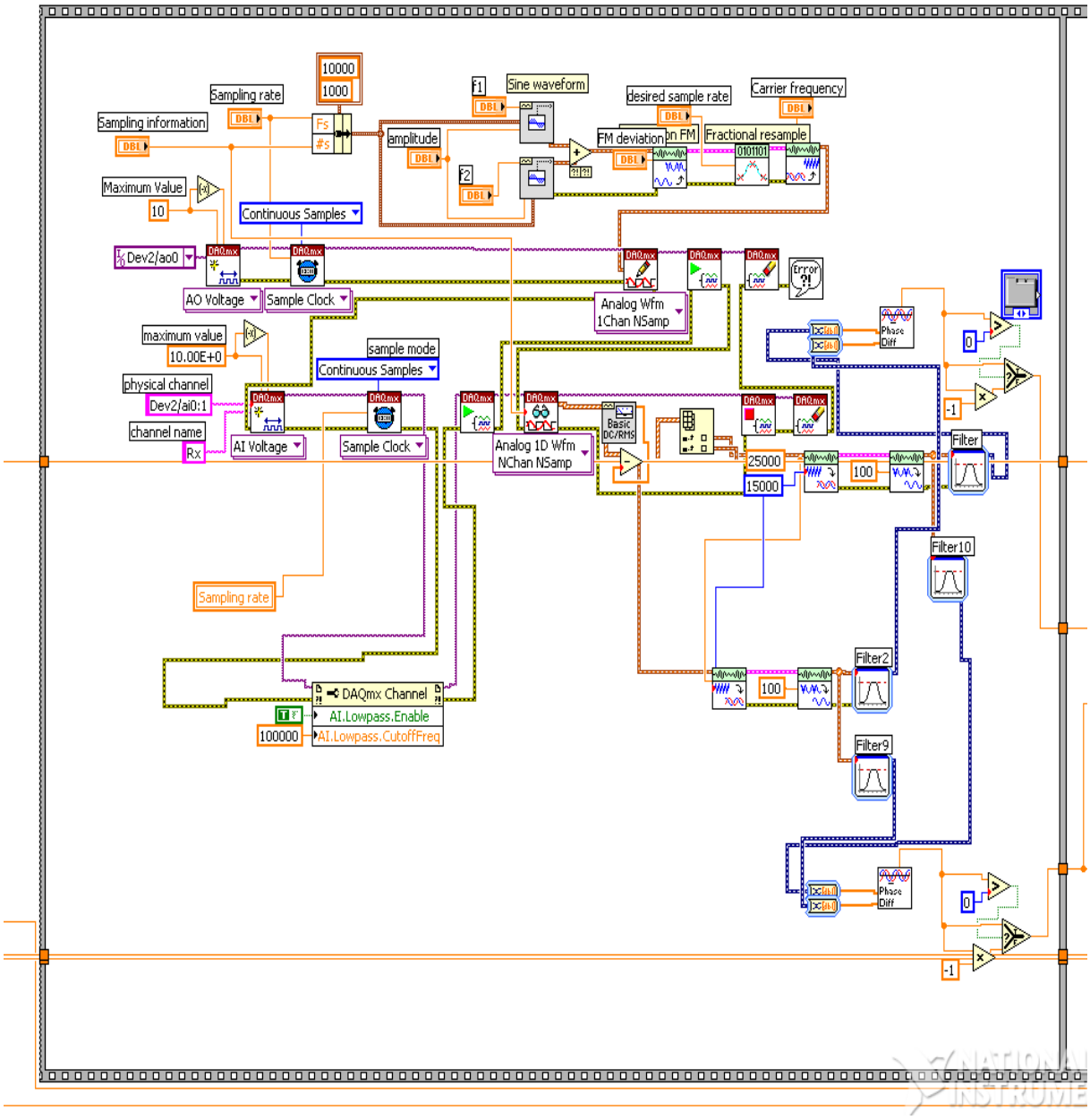
10000
1000
Sampling rate
Sampling information
Fs
#s
f1
Sine waveform
desired sample rate
Carrier frequency
amplitude
FM deviation
on FM
Fractional resample
Maximum Value
10
Continuous Samples
f2
Dev2/ao0
AO Voltage
Sample Clock
Analog Wfm
1Chan NSamp
Error
maximum value
10.00E+0
sample mode
Continuous Samples
physical channel
Dev2/ai0:1
channel name
Rx
AI Voltage
Sample Clock
Analog 1D Wfm
NChan NSamp
Basic
DC/RMS
Phase
Diff
25000
15000
100
Filter
Filter10
Filter2
Filter9
Sampling rate
DAQmx Channel
AI.Lowpass.Enable
100000
AI.Lowpass.CutoffFreq
0
-1

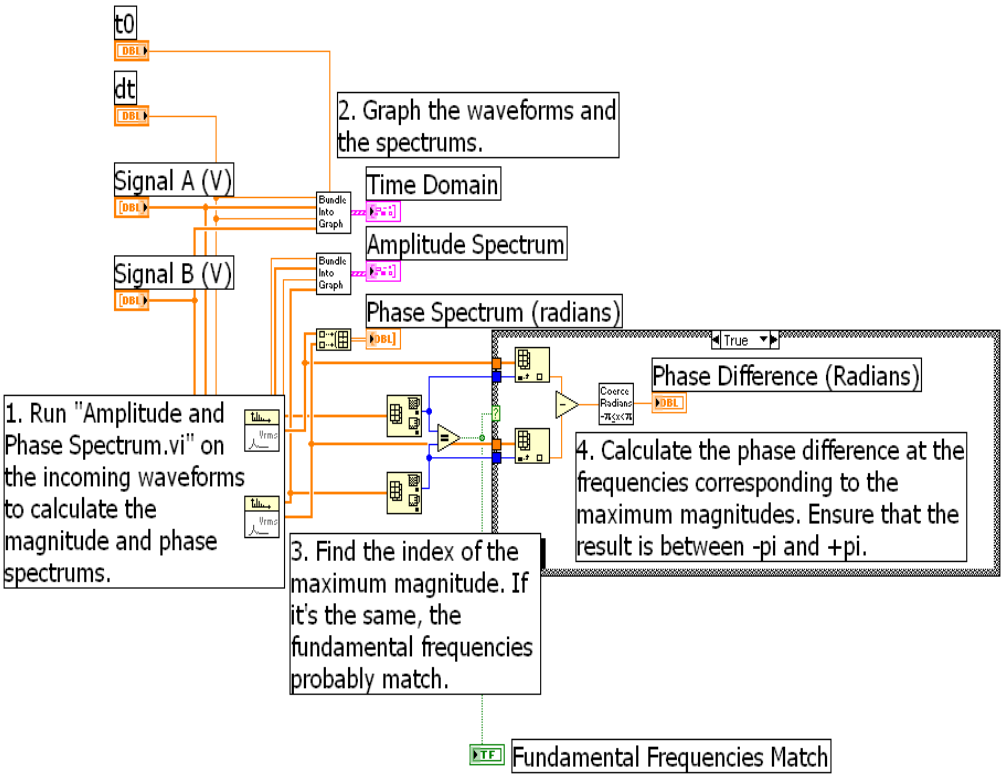
t0
dt
Signal A (V)
Signal B (V)
2. Graph the waveforms and the spectrums.
Time Domain
Amplitude Spectrum
Phase Spectrum (radians)
Bundle Into Graph
Bundle Into Graph
1. Run "Amplitude and Phase Spectrum.vi" on the incoming waveforms to calculate the magnitude and phase spectrums.
True
Phase Difference (Radians)
Coerce Radians
4. Calculate the phase difference at the frequencies corresponding to the maximum magnitudes. Ensure that the result is between -pi and +pi.
3. Find the index of the maximum magnitude. If it's the same, the fundamental frequencies probably match.
Fundamental Frequencies Match

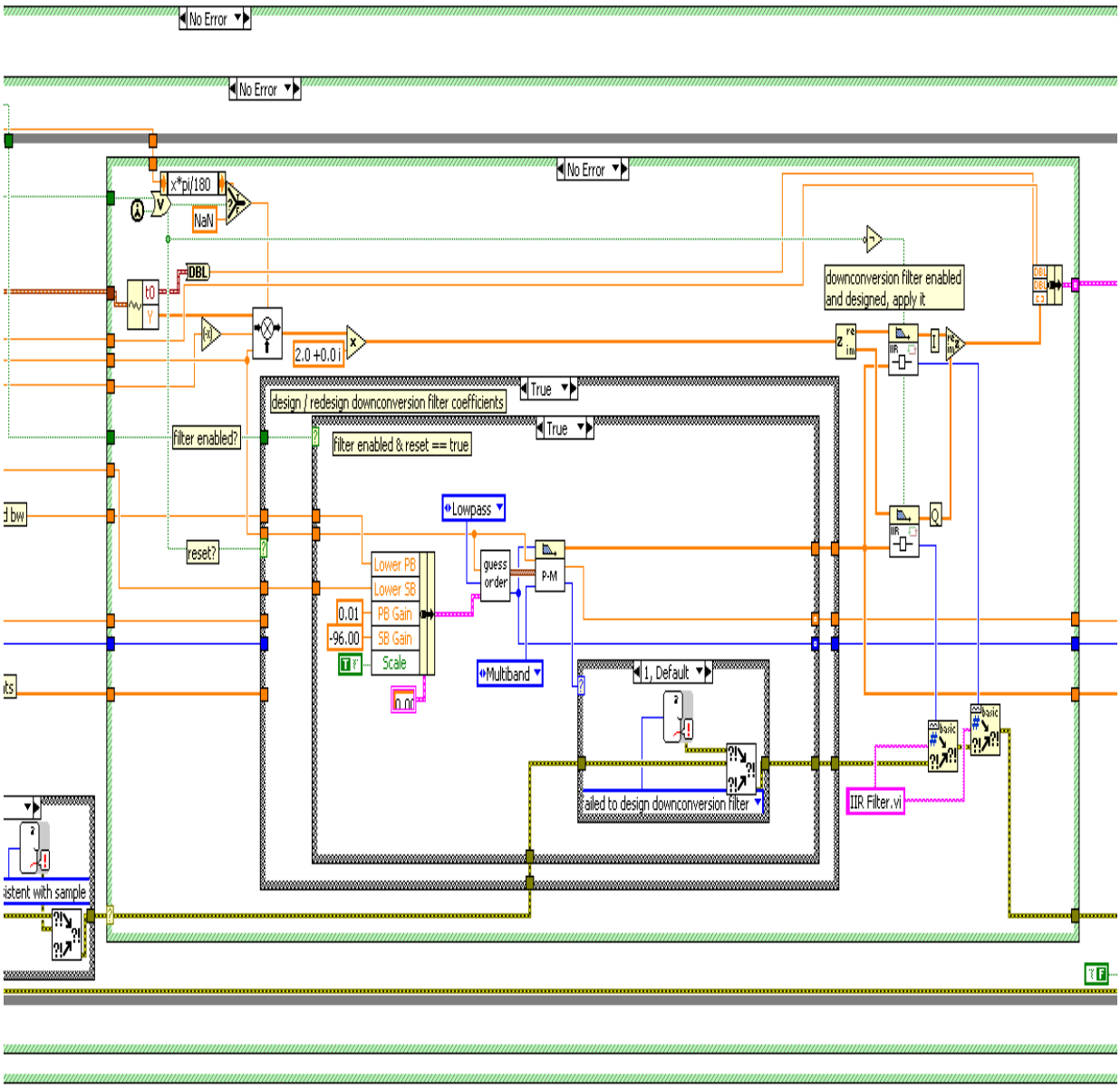
No Error
No Error
No Error
x*pi/180
NaN
DBL
tf0
Y
-tf-
2.0 +0.0 i
downconversion filter enabled and designed, apply it
design / redesign downconversion filter coefficients
True
True
filter enabled & reset == true
filter enabled?
reset?
Lowpass
Lower PB
Lower SB
PB Gain
SB Gain
Scale
0.01
-96.00
guess order
P-M
Multiband
1, Default
ailed to design downconversion filter
IIR Filter.vi
d bw
ts
istent with sample

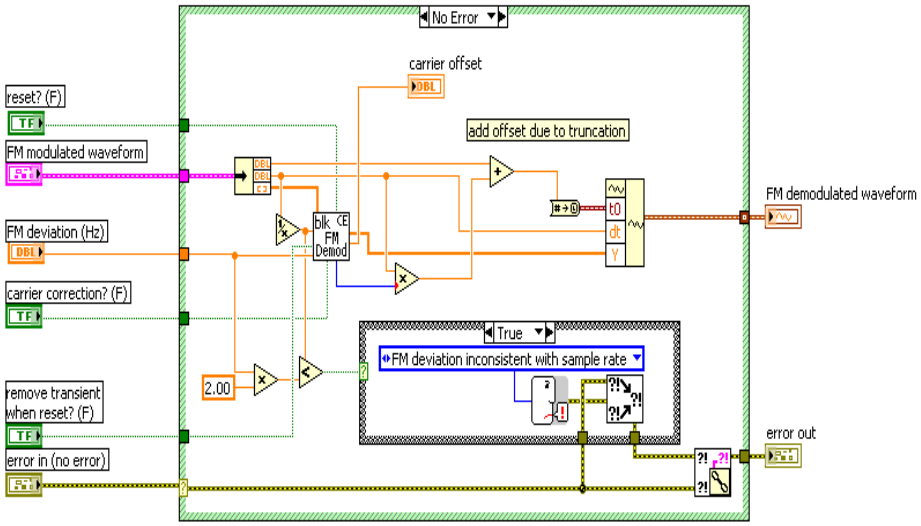
No Error
carrier offset
reset? (F)
FM modulated waveform
add offset due to truncation
FM demodulated waveform
FM deviation (Hz)
blk CE FM Demod
carrier correction? (F)
True
FM deviation inconsistent with sample rate
2.00
remove transient when reset? (F)
error in (no error)
error out

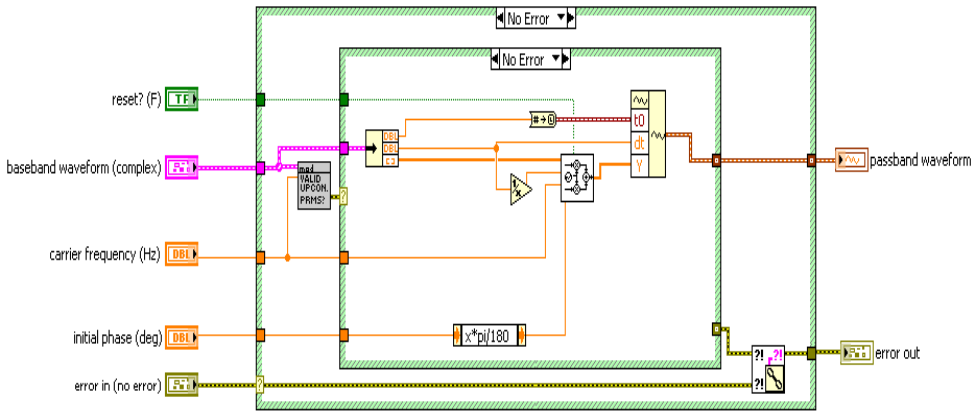
No Error
No Error
reset? (F)
baseband waveform (complex)
carrier frequency (Hz)
initial phase (deg)
error in (no error)
x*pi/180
passband waveform
error out

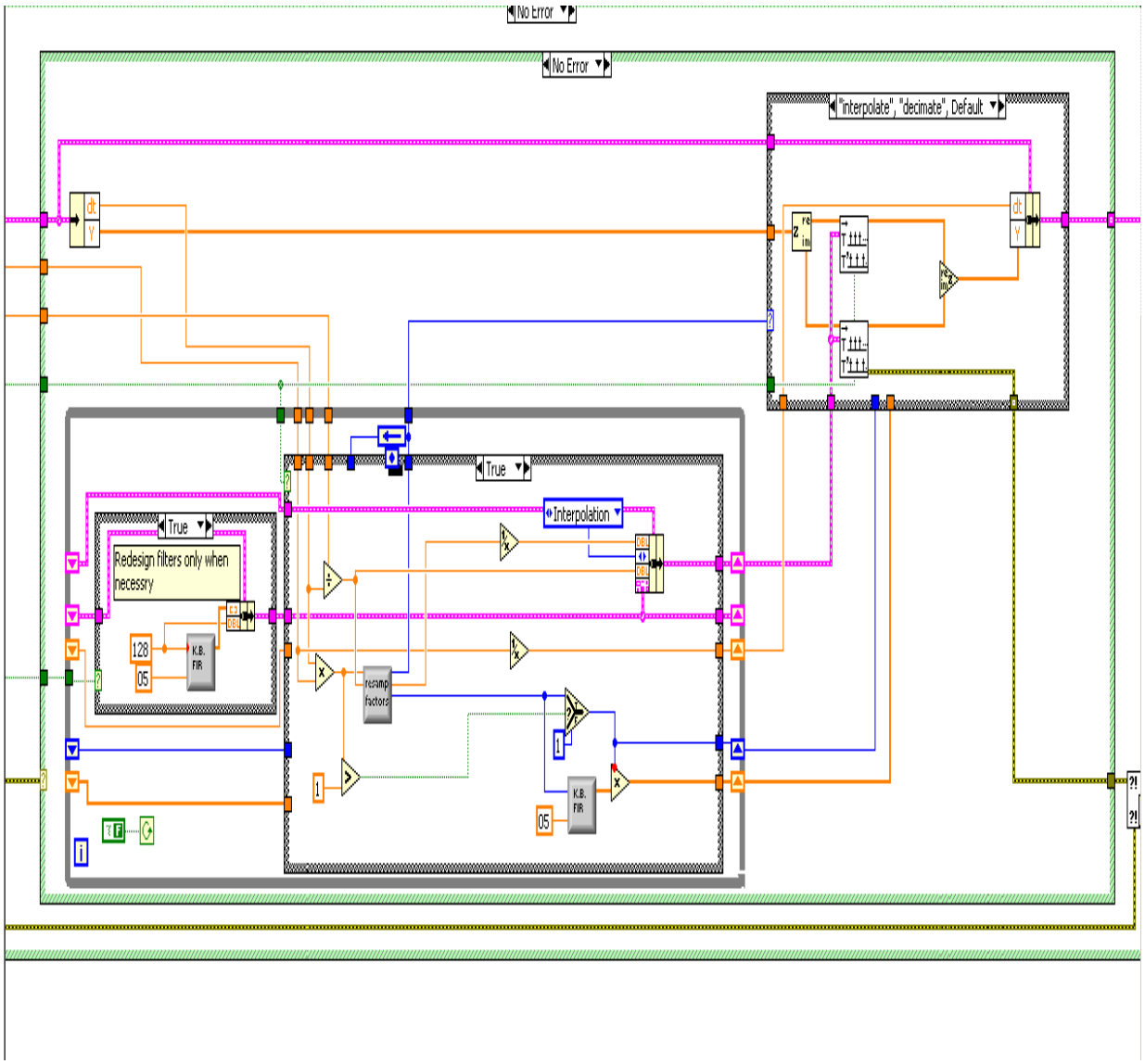
No Error
No Error
"interpolate", "decimate", Default
True
True
Interpolation
Redesign filters only when necessry
128
05
K.B. FIR
Resamp Factors
K.B. FIR
05

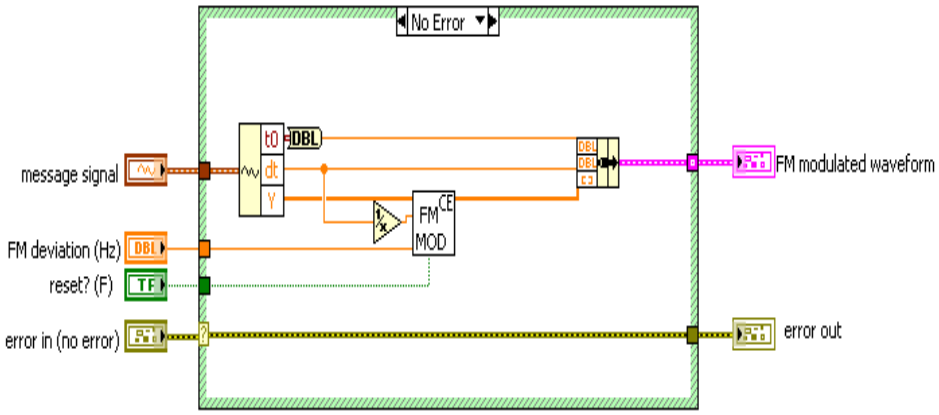
No Error
message signal
FM deviation (Hz)
reset? (F)
error in (no error)
t0
dt
Y
DBL
FM
MOD
FM modulated waveform
error out

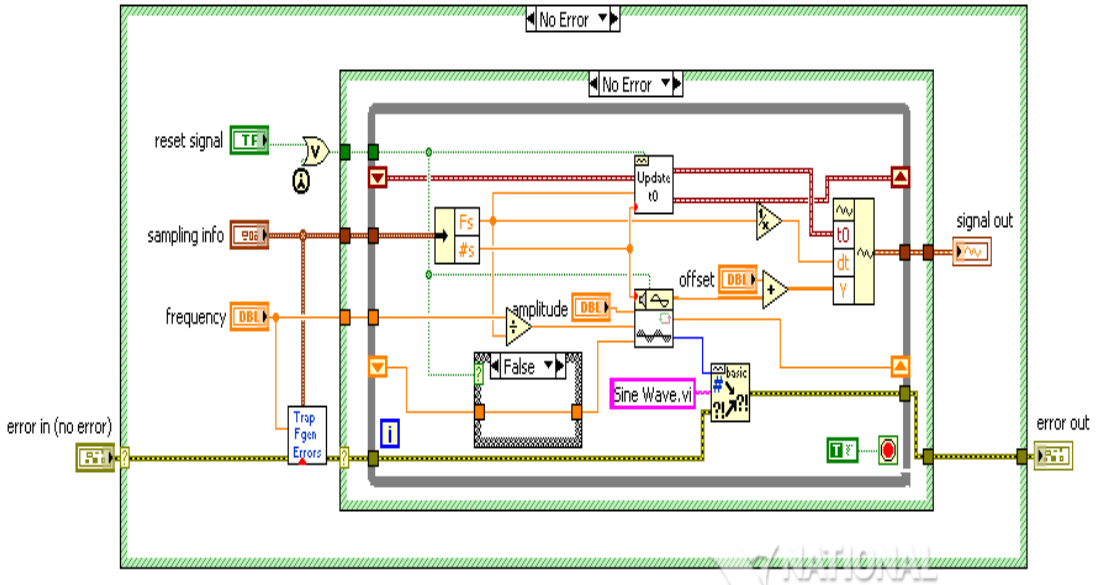
No Error
No Error
reset signal
sampling info
frequency
error in (no error)
Update t0
Fs
#s
amplitude
offset
False
Sine Wave.vi
Trap Fgen Errors
signal out
error out